1993

High Resolution Gas-phase Silicon 2p Core-level Spectroscopy Using Synchrotron Radiation

Douglas George Sutherland

HIGH RESOLUTION GAS-PHASE Si 2*p* CORE-LEVEL SPECTROSCOPY USING SYNCHROTRON RADIATION

by

Douglas G.J. Sutherland

Department of Chemistry

Submitted in partial fulfillment
of the requirements for the degree of
Doctor of Philosophy

Faculty of Graduate Studies
The University of Western Ontario
London, Ontario, Canada
April 1993

ISBN 0-315-83978-3

Canada

ABSTRACT

High resolution (0.05 eV) Si 2*p* pre-edge photoabsorption spectra of SiH_4, SiD_4, Si_2H_6 and Si_3H_8 show a large number of peaks due to Si 2*p* → Rydberg transitions, along with rich vibrational structure. The SiD_4 spectrum has been very useful in distinguishing between Rydberg states and vibrational excitations. The spectra of Si_2H_6 and Si_3H_8 are very similar to each other, exhibiting excitation of asymmetric Si-H vibrations.

The Si L- and K-edge XANES spectra of $Si(OCH_3)_X(CH_3)_{4-X}$ (X=0-4) are reported and the two end members of the series, $Si(OCH_3)_4$ and $Si(CH_3)_4$, are compared to the spectra of SiO_2 and SiC. The L-edge spectra of gaseous $Si(OCH_3)_4$ and solid SiO_2 are qualitatively identical, while the L-edge spectra of $Si(CH_3)_4$ and SiC show strong similarities. MS-Xα calculations for the two species $Si(OCH_3)_4$ and $Si(CH_3)_4$ were used to assign the various spectra for both compounds. Assignments for SiO_2 are based upon a molecular orbital interpretation of the electronic structure of this compound.

High resolution (~0.1 eV) Si 2*p* gas-phase photoelectron spectra of 24 compounds are reported: SiH_XD_{4-X}; $Si(CH_3)_X(OCH_3)_{4-X}$; $Si(CH_3)_X[N(CH_3)_2]_{4-X}$; $SiH_X[Si(CH_3)_3]_{4-X}$; (X=0-4), and SiH_3-CH_3, SiH_3-SiH_3, SiH_3-SiH_2-SiH_3, $Si(CH_3)_3$-$Si(CH_3)_3$, $Ge[Si(CH_3)_3]_4$ and $[Si(CH_3)_2]_6$. Vibrational excitations have been resolved in the spectra of SiH_XD_{4-X}, SiH_3-CH_3, SiH_3-SiH_3 and SiH_3-SiH_2-SiH_3. For the compounds SiH_XD_{4-X} and SiH_3-CH_3 the vibrational structure is dominated by the Si-H, Si-D or Si-C symmetric vibrational mode. Conversely, the spectra of SiH_3-SiH_3 and SiH_3-SiH_2-SiH_3 are dominated by the asymmetric Si-H bending vibrations - the first example

of this in core-level photoelectron spectroscopy. In the remaining compounds the vibrational effects are not resolved; however, the peak widths increase in the order $Si(CH_3)_4$ < $Si[Si(CH_3)_3]_4$ < $Si[N(CH_3)_2]_4$ < $Si(OCH_3)_4$ < SiF_4 indicating that the vibrational manifold increases analogously.

The valence photoelectron spectra of $Si(CH_3)_4$, $Si(CH_3)_3$-$Si(CH_3)_3$, $Si[Si(CH_3)_3]_4$, $Ge[Si(CH_3)_3]_4$ and $[Si(CH_3)_2]_6$ are reported at four different photon energies, 21.2, 100, 120 and 135 eV.

ACKNOWLEDGEMENTS

I would like to express my sincere thanks to my research supervisor Prof. G.M. (Mike) Bancroft for his support, his guidance and for his tireless enthusiasm for even the smallest details of this work. Also, many of the results presented here are the direct result of technical assistance provided by Dr. K.H. Tan, Dr. B.X. Yang and the staff at the Aladdin Synchrotron Radiation Center at the University of Wisconsin at Madison.

I also wish to acknowledge the support and contributions made by other members of the Department of Chemistry at the University of Western Ontario and especially those members of our research group: Dr. M. Kasrai, Dr. L. Coatsworth, Jay Microft, Mike Scaini, Leone Maddox, Jammie Price, Zhi Feng Lui, Yong Feng Hu, Xiaorong Li, Ziqi Gui, Dien Li and Zhanfeng Yin. In particular I would like to thank Dr. J.D. (John) Bozek and Dr J.N. (Jeff) Cutler whose contributions to this work and friendship were indispensable. I would also like to thank Dr. J. (Joe) Shapter and Dr. S.J. (Steve) Bushby for keeping me humble on the squash courts.

Finally, I would like to thank my parents Mrs. Kathleen M. Sutherland and the late Mr. Robert M. Sutherland from whom I learned the following quote:

A little learning is a dangerous thing;
Drink deep or taste not the Pierian spring:
There shallow draughts intoxicate the brain,
And drinking largely sobers us again.

Alexander Pope.
An Essay On Criticism,
Part II, Line 15

TABLE OF CONTENTS:

TABLE OF CONTENTS (*Continued*)

TABLE OF CONTENTS (*Continued*)

LIST OF TABLES

LIST OF TABLES (*Continued*)

LIST OF FIGURES

LIST OF FIGURES (*Continued*)

LIST OF FIGURES (*Continued*)

CHAPTER I:

INTRODUCTION

Section I-1; Synchrotron Radiation.

X-rays were first discovered in 1895 by Wilhelm Conrad Roentgen and for this work he received, in 1901, the very first Nobel Prize in Physics. The Roentgen tube, and derivations thereof, continued to be the most intense source of X-rays up to, approximately, the mid point of the twentieth century when, in 1947, the first observation of synchrotron radiation was made at The General Electric Company in Schenectady New York.[1-3]

The use of synchrotron radiation for scientific research proceeded, at first, as a parasitic endeavor with scientists in this field using the synchrotron radiation that was produced as a by-product of cyclotrons and other particle accelerators in which charged particles were accelerated through a quasi-circular orbit. The first accelerator that was dedicated to the production of synchrotron radiation for use in spectroscopy was the 240 MeV storage ring, *Tantalus*, at the University of Wisconsin at Madison which was constructed in the late 1960's, becoming fully operational in 1973.[4] In the twenty years since then, around the world, more than 35 synchrotrons have been constructed or will be completed in the near future.[5] These instruments range in size from a circumference of ~15 m up to ~1 km for a facility such as *The Advanced Photon Source* at Argonne, with a cost of between 20 million and 456 million dollars,[6] respectively.

The characteristics of the photons produced by synchrotron radiation are determined from a number of parameters; chiefly, the energy of the electrons circulating in the storage ring, the radius of curvature of the electron orbit, the strength of the magnetic filed in the bending magnets

and the current or number of electrons in the ring. The details and theoretical aspects of the production of synchrotron radiation is beyond the scope of this thesis but have been discussed at length in many other publications.[6-8] Qualitatively, synchrotron radiation is a continuum light source with an energy distribution curve that rises slowly at low energy (usually in the infrared) to a maximum value at some critical energy, E_c, which is dependant upon the bending-radius of the electron beam. The intensity then drops off sharply at higher energy, usually in the hard X-ray region of the spectrum.

For nearly all spectroscopic studies some type of monochromator must be employed to separate out from the continuum those wavelengths of interest. From this point of view the energy domain can be divided into three main regions: 0 to 30 eV, 30 to 1000 eV and those energies greater that 1000 eV. In the first region, monochromators utilizing normal incidence or near-normal incidence optics can be employed. Between 30 and 1000 eV standard grating-type monochromators can still be used but only in conjunction with glancing angle optics to avoid absorption of the photons by the optical media. Above 1000 eV the wavelength of the photons is too small even for holographically ruled gratings to be practical and monochromatization is usually achieved with crystal optics employing the principles of Bragg diffraction. Within each of the three energy domains there exist a number of specific monochromator designs whose throughput throughout the range of interest is characterized by its range of practical operation, its intensity as well as spatial and spectral resolution.

Section I-2; Photoabsorption.

The study of the interaction of light with matter dates back to antiquity with the earliest recorded theories pre-dating even Aristotle. This interaction was not quantified, however, until the time of J.H. Lambert (1728-77) who devised the first laws of photoabsorption spectroscopy which were later refined by Beer to form the familiar Beer-Lambert equation,

$$\mathrm{Log}(I_o/I) = \mu x \qquad \text{[Eq. I-1]}$$

where I_o and I are, respectively, the initial and final intensities of the radiation, μ is the absorption coefficient and x is the path-length of the light.

The absorption coefficient, μ, can be related to the absorption cross section, σ, of an individual atom or molecule via Equation I-2,

$$\mu = N_A \sigma \qquad \text{[Eq. I-2]}$$

where N_A is the number density of absorbing species in the path of the light. The cross section, σ, varies as a function of the frequency of the radiation and is related directly to the electronic structure of the absorbing species. Thus, the absorption coefficient $\mu(\omega)$, at frequency ω, can be written[9] in terms of the dipole matrix element M_{ij} according to Equation I-3,

$$\mu(\omega) = \frac{4\pi^2 e^2}{\eta \hbar c} \hbar\omega \sum_{i,j} |M_{ij}|^2 \delta(E_i - E_j - \hbar\omega) \qquad \text{[Eq. I-3]}$$

where η is the index of refraction, and the delta function, $\delta(E_i - E_j - \hbar\omega)$, is introduced to ensure that only transitions between quantized states with energy difference $\hbar\omega$ are allowed. The dipole matrix element M_{ij} represents the probability of an electron in state $|i\rangle$ interacting with the electric field of the impinging radiation and being promoted to some state $|j\rangle$. In a system with n electrons this can be expressed mathematically as Equation I-4,

$$M_{ij} = \langle \Psi_j^* | \sum_n \hat{r}_n | \Psi_i \rangle \qquad \text{[Eq. I-4]}$$

where $\hat{r}_n$ is the dipole moment operator for the system and Ψ_i and Ψ_j are, respectively, the initial and final state wavefunctions of the molecule. Equation I-4 is often written in terms of the one particle approximation where the many-electron wavefunctions, Ψ, are replaced by n one-electron wavefunctions, ψ, each of which act independently of all others. Here, M'_{ij}, the one-particle approximation of M_{ij}, can be written as Equation I-5.

$$M'_{ij} = \langle \psi_j^* | \hat{r} | \psi_i \rangle \qquad \text{[Eq. I-5]}$$

Although other phenomena, (such as magnetic dipole transitions, as well as electronic and and magnetic quadrapole transitions) do contribute to the absorption process, it is the matrix element $\langle\psi_j^*|\vec{r}|\psi_i\rangle$ in Equation I-5 that is the primary intensity giving process in electronic absorption spectroscopy. For the quantity M'_{ij} to have some finite value, three criteria must be met:

(i) Some component of the electric dipole of the molecule must be aligned with some component of the electric vector of the light.

(ii) The initial and final states must be separated in energy by an amount equivalent to that of the incoming photon ($\hbar\omega$).

(iii) The initial and final state wavefunctions must overlap; that is, they must not be orthogonal.

In the case where $|\psi_i\rangle$ represents the wavefunction of an electron in a core orbital which is localized on nucleus k, then, for the matrix element in Equation I-5 to have some finite value, the final state wavefunction, $|\psi_j\rangle$, must also have significant amplitude in the vicinity of nucleus k. For such discrete core-level transitions the absorption coefficient, $\mu(\omega)$, is usually replaced by the oscillator strength, f_{ij}, which is defined in Equation I-6.

$$f_{ij} = \frac{2m\hbar\omega}{\hbar^2}|M_{ij}|^2 \qquad \text{[Eq. I-6]}$$

In this definition of the oscillator strength, for an N electron atom in initial state i, f_{ij} will follow the sum rule first derived by Thomas, Kuhn and Reiche,[10] (Equation I-7).

$$\sum_J f_{IJ} = N \qquad \text{[Eq. I-7]}$$

However, in core-level photoabsorption, most of the oscillator strength occurs in that energy domain which lies above the ionization threshold in the continuum. In the continuum the oscillator strength, f_{IJ}, is replaced by the spectral density, df/dE, and thus, applying the sum rule to both the discrete and continuum regions, equation I-7 becomes,

$$\sum_J f_{IJ} + \int_{E_I}^{\infty} \frac{df}{dE}\, dE = N \qquad \text{[Eq. I-8]}$$

where the lower limit of integration, E_I, is the energy of ionization.

Core-level absorption spectra are usually divided into two separate regions.[11] The near-edge region includes the discrete below-edge transitions as well as those that occur up to approximately 50 eV above the edge. This region of a molecule's spectrum is referred to as "Near-Edge X-ray Absorption Fine Structure" (NEXAFS) or, equivalently, just "X-ray Absorption Fine Structure" (XANES). Features at higher energies are referred to as "Extended X-ray Absorption Fine Structure" (EXAFS). Peaks in this region of the spectrum result largely from backscattering of the outgoing photoelectron from the surrounding atoms in the molecule. The backscattered electron wave interferes with that of the outgoing electron wave resulting in regions of differing amplitude in the total electron wavefunction. These differences in amplitude result in the presence of weak peaks in the

extended x-ray region of the spectrum. Although EXAFS is not dealt with specifically in this thesis there are a number of excellent treatises that document the details of this phenomenon.[11-13] Peaks in the XANES region of the spectrum result from either transitions to bound states (of Rydberg, anti-bonding molecular orbital, or mixed character) in the discrete pre-edge region, or, in the continuum, the electron may be ejected directly into the vacuum or it may be temporarily trapped in the vicinity of the molecule by some potential well.[14]

Section I-3; Photoelectron Spectroscopy.

The development of photoelectron spectroscopy (PES) is usually attributed to Kai Siegbahn of the University of Uppsala during the late 1950's and early 1960's. However, the roots of the technique can actually be traced back to the turn of the century when Innes[15] recorded the first photoelectrons using a Roentgen tube with a platinum anticathode, two Helmholtz coils to deflect the electrons and a photographic plate to permanently record their trajectory. It is interesting to note that this work was done only ten years after the discovery of the electron by J.J. Thompson and several years before Rutherford's discovery of the nuclear atom. Although Einstein had published his theory of the photoelectric effect only two years earlier, Innes, in explaining his results, erroneously concludes that, "the most probable cause is atomic disintegration".

Quantum theory and the theory of the nuclear atom, developed in the first quarter of this century, led to a better understanding of photoelectrons and eventually set the stage in the 1950's for the first *high resolution* photoelectron spectrometers built by Siegbahn at Uppsala. The early work in this field was all done on solids; the first gas-phase spectrum being recorded by Krause[16] in 1965. The basic PES technique involves the ionization of a sample molecule by a monochromatic beam of high energy photons with subsequent measurement of the kinetic energy of the ejected photoelectron. The binding energy of the electron is determined via Equation I-9,

$$BE = h\nu - KE \qquad \text{[Eq. I-9]}$$

where BE is the binding energy of the orbital from which the photoelectron was ejected, $h\nu$ is the energy of the absorbed photon and KE is the measured kinetic energy of the photoelectron. Photoionization is an electric dipole interaction between the electric field of the impinging radiation and the electric dipole of the atom or molecule. The equations describing this process have been outlined in Section I-2 of this chapter and need not be repeated here.

In addition to the photon and binding energies, the kinetic energy of the photoelectron is also a manifestation of the total energy (electronic, vibrational, rotational, etc.) of the resulting ion[16]. In atoms and molecules with filled degenerate sub-shells the removal of an electron can result in two final electronic states caused by the spin-orbit interaction. For instance, removal of an electron from an atomic *p*-orbital can result in an ion whose total angular momentum quantum number, J, is either 1/2 or 3/2 depending on whether the spin angular momentum of the electron hole is opposed or aligned with the orbital angular momentum of the ion. The 1:2 ratio of the intensities of the resulting two peaks is a manifestation of the (2J+1)-fold degeneracy of the two electronic states of the ion.

Another cause of multiple lines in the photoelectron spectrum is the different vibrational states of the ion. Each possible vibrational state of the ion that becomes populated dictates that there will be that much less energy imparted to the ejected electron. Thus, photoelectron spectra of simple molecules often exhibit peaks whose energy spacing is a direct reflection of the spacing between vibrational quanta in the ion. Rotational

transitions are too small to be resolved and it is reasonable to assume that because their energy spacing is so much smaller than the lifetime linewidth that they contribute only a small amount to the overall linewidth of the spectrum.

Other notable effects include ligand-field splitting, shake up and shake off. Ligand field splitting occurs when the electric field of a ligand acts as a perturbation which destroys the degeneracy of the atomic *p* and or atomic *d*-orbitals on the atom to which the ligand is bound. Although this effect can be quite large it is much less common than vibrational effects and usually only occurs when the central atom and its ligand(s) have very disparate electronegativities. Shake up is the result of electronic excitation in the ion that accompanies photoionization and shake off is another two-electron process resulting in double ionization.[10] Shake up and shake off together usually only account for approximately 10% of the total ionization cross section.

In determining the binding energy of an electron one usually assumes Koopmans' theorem[17] to be true. In Koopmans' theorem the photoionization process is treated as a single electron event in which the kinetic energy of the outgoing photoelectron is neither enhanced nor impeded by any relaxation or configuration interaction between the photoelectron and those electrons remaining in the ion. A second, and less important, approximation is that the photoelectron, from the conservation of momentum, contains essentially all of the kinetic energy imparted to the system by the absorbed photon.

With these two approximations in mind, photoelectron spectroscopy has been used to measure directly the relative energies of the different molecular orbitals of thousands of compounds in both the solid and gaseous state. Although the study of valence level photoelectron spectroscopy has

proceeded rapidly right from the very beginning, interest in core level spectra has taken longer to catch on. This is due, primarily, to the poor resolution that results from the use of laboratory line sources such as Al Kα and Mg Kα. Typically, the bandwidth of such a photon source is on the order of 1 eV and the high photon energies (1486 eV for Al and 1253 eV for Mg) result in very high electron kinetic energies for all but the deepest of cores. As a result, the full-width-half-height of the resulting photoelectron peak can often be greater than 2 eV, thereby destroying any of the fine structure and chemical information it may contain.

Although many refinements of the technique have taken place since its inception, arguably the most important of these is the availability of synchrotron radiation which can be tuned to essentially any energy and thus provide a convenient, highly monochromatic excitation source. These highly monochromatic sources have lead to better energy resolution of the ejected photoelectron and through this, a better understanding of the ionization process has evolved. The advent of tunable, highly monochromatic synchrotron radiation has allowed the resolution of features as small as 0.1 eV on low lying (~100 eV) cores[18] and has improved the resolution of deeper cores to a similar degree. Core level spectra are easier to interpret[19] than the corresponding valence level of the same compound and have thus become an important tool in the study of complex systems such as polymers and surfaces.

When a core level electron is ejected it leaves the remaining electrons in the ion in an excited state configuration. The ion can then relax through one of two processes, namely, x-ray fluorescence or Auger emission shown schematically in Figures I-1a and I-1b. In the fluorescence process, a valence electron fills the core hole with subsequent emission of

Figure I-1: (a) The schematic representation of relaxation via fluorescence decay in a core-ionized atom. (b) The schematic representation of relaxation via Auger emission in a core-ionized atom.

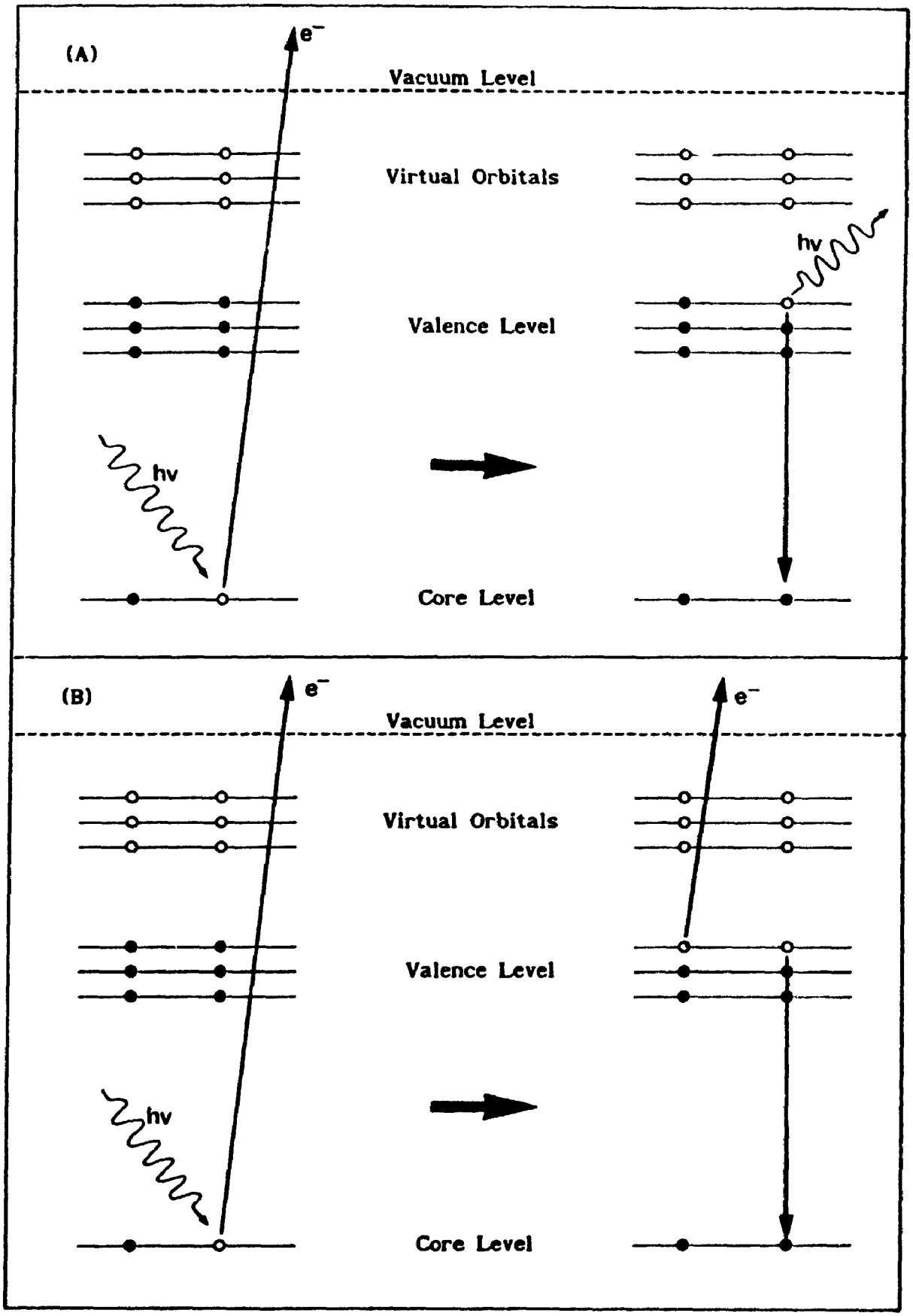
(A)
e⁻
Vacuum Level
Virtual Orbitals
hv
Valence Level
hv
Core Level
(B)
e⁻
Vacuum Level
e⁻
Virtual Orbitals
Valence Level
hv
Core Level

a photon with energy, $h\nu$, equivalent to the energy difference between the valence and core level. In the case of Auger decay, the energy released when a valence electron drops into the core hole is sufficient to cause ionization of a second electron from the molecule. The rate at which these processes occur defines the lifetime of the core hole which is directly related to the linewidth through the Heisenberg uncertainty principle[20] shown in Equation I-10,

$$\Gamma_l \geq \hbar/\tau \qquad \text{[Eq. I-10]}$$

where Γ_l is the lifetime linewidth (full width at half-height) of a given state and $\tau(=t_{1/2}/0.693)$ is the mean lifetime of that state. The total linewidth, Γ_T, of a photoelectron peak is given by Equation I-11,

$$\Gamma_T = (\Gamma_s^2 + \Gamma_a^2 + \Gamma_l^2)^{1/2} \qquad \text{[Eq. I-11]}$$

where Γ_s is the linewidth of the ionizing source, Γ_a is the linewidth of the analyzer and Γ_l is the lifetime, or inherent linewidth of the system being studied. The total linewidth of most spectra in this thesis is determined primarily by the source linewidth, Γ_s. Table I-1 shows how Γ_T varies as a function of Γ_s when Γ_l is held constant at 0.035 eV (the lifetime of the Si $2p$ hole state[21]) and Γ_a is held at 0.060 eV, the resolution of the analyzer.

Table I-1. The relationship between Γ_T and Γ_s when Γ_I and Γ_a are held constant at 0.035 eV and 0.060 eV respectively.

Γ_s (eV)	Γ_T (eV)
0.010	0.070
0.020	0.072
0.030	0.076
0.040	0.080
0.050	0.086
0.060	0.092
0.070	0.099
0.080	0.106
0.090	0.114
0.100	0.122
0.110	0.130
0.120	0.139
0.130	0.147
0.140	0.156
0.150	0.165

If the Auger process is fast, (ie. the lifetime of the core hole is short), and, if the Auger electron has higher energy than the photoelectron, then the Auger electron can catch up to the photoelectron before both have fully escaped from the atom or molecule. This process is referred to post-collisional interaction (PCI) and can result in long tails being produced on the high kinetic energy side of the photoelectron peak.[22] The effects of PCI on photoelectrons is complicated by the fact that in most cases there is usually more than one Auger electron emitted.

All of the core level photoelectron spectra presented in this thesis are of the Si 2*p* level which has a lifetime of approximately 1.18 X 10^{-13} s (35 meV).[21] Typical kinetic energies for the photoelectrons are ~25 eV; thus the photoelectrons are more than 350 nm away from the molecule before the Auger electron is emitted, and this coupled with the comparatively low

energy of the Si Auger electrons leads to spectra that are largely unaffected by PCI. By comparison, the C 1*s* lifetime is only 0.10 eV and thus the photoelectron (at 25 eV) will only be 100 nm away when the Auger electron is emitted. Hence, even in photoelectron spectra of the C 1*s* edge, PCI will only be important at kinetic energies that are substantially less than 25 eV. However, it should be noted that the Auger electrons emitted as a result of ionization of the C 1*s* shell have much higher energy than do those that result from ionization of the Si 2*p* level. This coupled with the shorter lifetime of the C 1*s* state makes PCI much more important in C 1*s* spectroscopy than it is in the spectra of the Si 2*p* level.

Section I-4; SCF MS-Xα Calculations.

The calculation of the electronic properties of molecules through the use of the MS-Xα method has been described in detail in a number of reports[23-32] and thus, for the sake of brevity, only a brief outline of the technique will be presented here. The problem of the motion of electrons in the field of atomic nuclei is best approximated by the Hartree-Fock type one-electron wavefunctions. However, the amount of computer time required is usually prohibitive for polyatomic molecules and thus, a simplified version is required. The Xα method is a self-consistent-field (SCF) technique which uses a "muffin tin" model to approximate the one-electron potentials of the molecule. These potentials are calculated via the one-electron Shrodinger equation,[25]

$$[-\nabla_1^2 + V_c(1) + V_{x\alpha}(1)]\psi_i(1) = \varepsilon_i\psi_i(1) \qquad \text{[Eq. I-12]}$$

where $-\nabla_1^2$ is the kinetic energy, $V_c(1)$ is the electrostatic potential energy at position 1 of the complete electronic and nuclear charge (computed classically) and $V_{x\alpha}(1)$ is the exchange potential which is dependant upon the electron density, ρ, and the scaling parameter, α, as shown in Equation I-13.

$$V_{x\alpha}(1) = -6\alpha\left[\frac{3}{4}\,\pi\rho(1)\right]^{1/3} \qquad \text{[Eq. I-13]}$$

In the muffin tin model the molecule in question is broken down into three regions as shown schematically in Figure I-2. Region 1 represents the volume within the atomic sphere where the potential is approximated by a spherical average of the exact atomic potential. In the second region, the inter-sphere region, the molecular potential is approximated by a constant equal to the average of the inter-atomic potentials. In region 3 a spherically averaged potential is used to model the extra-molecular potential.

The starting potential is merely the superposition of the atomic potentials averaged in such a way so as to fit the muffin tin model. The muffin tin potentials are then used in the solution of the one-electron Schrodinger equation for each of the three different regions. Solution of these equations yields the single-electron energy eigenvalues, ε_i, which can, in turn, be used to calculate the single-electron wavefunctions, ψ_i, in their proper form with the boundary condition that both the wavefunction and its first derivative be continuous at the boundary of the sphere.

The orbitals thus calculated are populated with the correct number of electrons, determined by the criteria specified in the calculation and are then used to determine the new potential, thereby completing the first iteration. This iterative process is repeated to within a previously

Figure I-2: Schematic representation of the "muffin tin" approximation of intramolecular potentials. Area 1 represents the inner atomic sphere region, area 2 is the inter-atomic sphere region and area 3 is the extra-molecular region of the molecular potential.

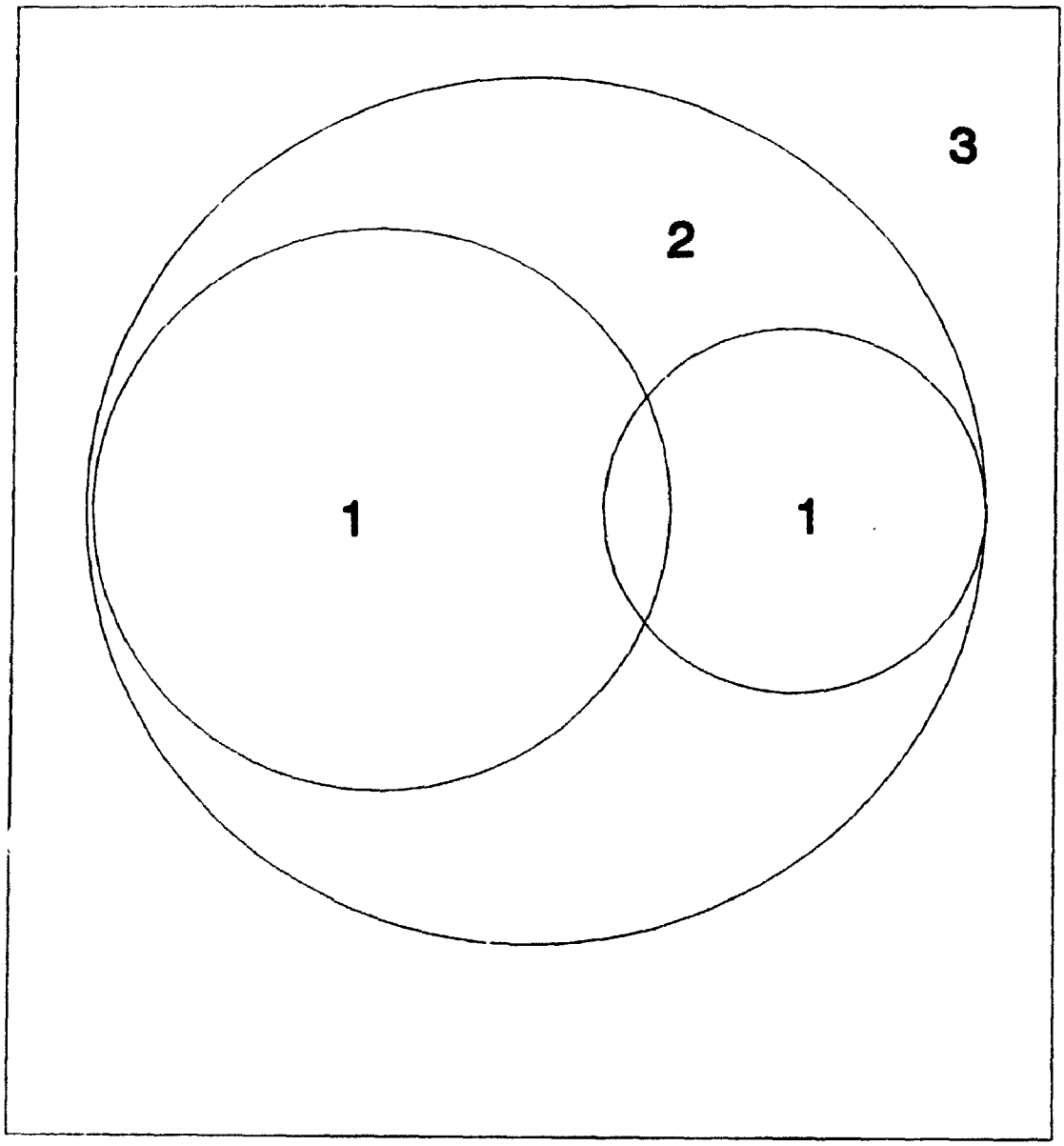
3
2
1
1

specified tolerance, eventually yielding the SCF molecular potential.

The cross section in both the discrete and continuum regions is calculated using equations of the form of [1-3] with incorporation of the proper scattering boundary conditions.[24,29] Because overlapping spheres have been found to result in improved descriptions of the ionization potentials, total energies of molecules and better behaved cross sections, the atomic sphere radii were calculated using the Norman procedure[30] and then enlarged by 15%. The atomic exchange parameters, α, were taken from Schwarz's tabulations[31] and the exchange parameters for both the inter and outer sphere regions are the average of the atomic values weighted by the number of valence electrons. In the continuum cross section calculation the asymptotic behavior of the potential at large values of r was treated by adding a Latter tail[32] to the outer sphere potential after the last iteration.

Section I-5; References.

1) F.R. Elder, A.M. Gurewitsch, R.V. Langmuir and H.D. Pollack, Phys. Rev., 71, 829, (1947)

2) F.R. Elder, A.M. Gurewitsch, R.V. Langmuir and H.D. Pollack; J. Appl. Phys., 18, 810, (1947)

3) F.R. Elder, R.V. Langmuir and H.D. Pollack; Phys. Rev., 74, 52, (1948)

4) E.M Rowe and F.E. Mills; Part. Accel., 4, 211, (1973)

5) H. Kobayakawa and K. Huke; Rev. Sci. Instr., 60, 2548, (1989)

6) (a) D.E. Moncton; Rev. Sci. Inst., 63(1), 1557, (1992).

(b) G. Margaritondo, *Introduction to Synchrotron Radiation*, Oxford University Press, New York, (1988): and references therein

7) H. Winik, "Properties of Synchrotron Radiation" in: *Synchrotron Radiation Research*, eds. H. Winik and S. Doniach, Plenum Press, New York, (1980)

8) S. Krinsky, M.L. Perlman and R.E. Watson, "Characteristics of Synchrotron Radiation and its Sources" in: *Handbook on Synchrotron Radiation*, eds. E.E. Koch, vol 1a, North Holland Publishing, New York, (1983)

9) F.C. Brown, "Inner-Shell Threshold Spectra", in: *Synchrotron Radiation Research*, ed. H. Winik and S. Doniach, Plenum Press, New York, (1980).

10) J. Berkowitz; *Photoabsorption, Photoionization and Photoelectron Spectroscopy*, Academic Press, New York, (1979)

11) E.A. Stern, "Theory of EXAFS" in *X-ray Absorption*, Eds. D.C. Koningsberger and R. Prins, John Wiley & Sons, New York, (1988).

12) B.K. Agarwal; *X-ray Spectroscop*, Springer-Verlag, Berlin, (1991)

13) (a) D.A. Sayers, E.A. Stern and F.W. Lytle; Phys. Rev. Lett., **27(18)**, 1204, (1971).

13) (b) P.H. Citrin, P. Eisenberger and B.M. Kincaid; Phys. Rev. Lett., **36(22)**, 1346, (1976).

(c) P.A. Lee, P.H. Citrin, P. Eisenberger and B.M. Kincaid; Rev. Mod. Phys., **53(4)**, 769, (1981).

14) J.L. Dehmer; J. Chem. Phys., **56**, 4496, (1972)

15) Jenkins et al; J. Elec. Spec. and Rel. Phen., **12**, 1, (1977)

16) T.A. Carlson; *X-Ray Photoelectron Spectroscopy*, Downden, Hutchinson and Ross Publishing; Stroudsberg, Penn.; (1978).

17) T. Koopmans; Physica, **1**, 104, (1933)

18) D.G.J. Sutherland, G.M Bancroft and K.H. Tan; J. Chem. Phys., **97(11)**, 7918, (1992).

19) F.J. Himpsel, B.S. Meyerson, F.R. McFeely, J.F. Morar, A. Taleb-Ibrahimi and J.A. Yarmoff, Proceedings from the Enrico Fermi School on "Photoemission and Absorption Spectroscopy of Solids and Interfaces with Synchrotron Radiation"; Ed. M. Campagna and R. Rosei, North Holland, Amsterdam, (1990).

20) A. Messiah, *Quantum Mechanics*, North Holland, Amsterdam, (1982)

21) (a) E.Z. Chelkowska and F.P. Larkins; J. Phys. B, **24**, 5083, (1991).

(b) J. McColl and F.P. Larkins; Chem. Phys. Lett., **196**, 343, (1992).

22) (a) V. Schmidt; J. de Phys., **48**, C9-401, (1987)

(b) K. Helenelund, U. Gelius, P. Froelich and O. Goscinski; J. Phys. B, **19**, 379, (1987)

(c) W. Eberhardt, S. Bernstorff, H.W. Jochims, S.B. Whitfield and B. Crasemann; Phys. Rev. A, **38**, 3808, (1988)

23) K.H. Johnson; Advan. Quantum Chem., 7, 143, (1973)

24) J.W. Davenport; Ph.D. Thesis, University of Pennsylvania, USA, (1976)

25) J.C. Slater and K.H. Johnson; Phys. Rev. B, 5, 844, (1971)

26) D.A. Case and M. Karplus; Chem. Phys. Lett., 39, 33, (1976)

27) D.A. Case; Ann. Rev. Phys., 33, 151, (1982)

28) J.C. Slater; Phys. Rev., 81, 385, (1951)

29) D. Dill and J.L. Dehmer, J. Chem. Phys., 61, 692, (1974)

30) J.G. Norman; J. Chem. Phys., 61, 4630, (1974)

31) K. Schwarz; Phys. Rev. B, 5, 2466, (1972)

CHAPTER II:

EXPERIMENTAL

Section II-1; The Grasshopper Beamline.

The details of the Grasshopper design,[1,2] and specifically that of the Canadian Grasshopper,[3] have been documented elsewhere and thus will not be treated in detail here. All of the Si 2*p* and Si 2*s* spectra in this thesis were recorded using the Mark IV Grasshopper monochromator at the Canadian Synchrotron Radiation Facility (CSRF) on the Aladdin Synchrotron at the University of Wisconsin at Madison.

The Mark IV is a high resolution, glancing angle design with a 2 meter, holographically ruled 1800 groove/mm grating mounted on a 1 meter Rowland circle[3] for use in the energy range 70 to 800 eV. The first optical component in the beamline is the M_0 mirror which collects 14 mrad of radiation from the storage ring in the horizontal direction and focuses it into the monochromator. Once inside the monochromator the radiation is vertically focused by the M_1 mirror which meets the radiation at a glancing angle of 1°. The 1° glancing angle (as opposed to 2° in earlier models) gives improved throughput at higher energies. From the M_1 mirror the radiation is is focused through a Codling-type entrance slit and reflected onto the grating from the slit mirror. The grating disperses the white light into its constituent wavelengths and reflects the resulting monochromatic beam through the exit slit.

The energy of the radiation leaving the exit slit can be adjusted by changing the relative positions of the M_1 mirror, the entrance slit mirror and the grating which can be moved mechanically by changing the position of the monochromator carriage. The now monochromatic radiation is then

simultaneously refocused in both the vertical and horizontal directions by a toroidal mirror to a minimum spot size at the interaction region and the Rowland-circle design ensures that the exit angle remains constant as a function of energy. The throughput of the beamline from 70 eV to 1000 eV was measured by monitoring the current produced when the radiation strikes a gold diode in the sample chamber. A plot of Current vs Photon Energy is shown in Figure II-1.

The theoretical linewidth of the resulting radiation can be calculated from Equation II-1,

$$\Delta\lambda(\text{Å}) = 0.003 \text{ X } S(\mu m) \qquad \text{[Eq. II-1]}$$

where $\Delta\lambda$ is the full width at half of the maximum intensity, 0.003 is a constant peculiar to the 1800 groove grating and S is the slit width of the entrance and exit slits. Thus, at 100 eV photon energy, and a slit width of 15 μm the band width of the photon source is 0.04 eV.

The monochromator is interfaced to a computer which can then be used to set a specific energy or scan an energy range of interest. The wavelength of the emitted radiation is related to the displacement of the monochromator through Equation II-2,

$$\lambda = d\left[\text{Sin } \alpha + \text{Sin}\left[\text{Sin}^{-1}\left(\frac{D - L_o}{R}\right) - (180 - \alpha)\right]\right] \qquad \text{[Eq. II-2]}$$

Figure II-1: The throughput of the CSRF Grasshopper monochromator from 70 eV to 1000 eV. This spectrum was recorded with a 1200 groove/mm grating as opposed to the 1800 groove/mm grating used in this thesis but the salient features of the spectral profile are the same. (Digitized from J.D. Bozek, Ph.D. thesis, Ref. # 7).

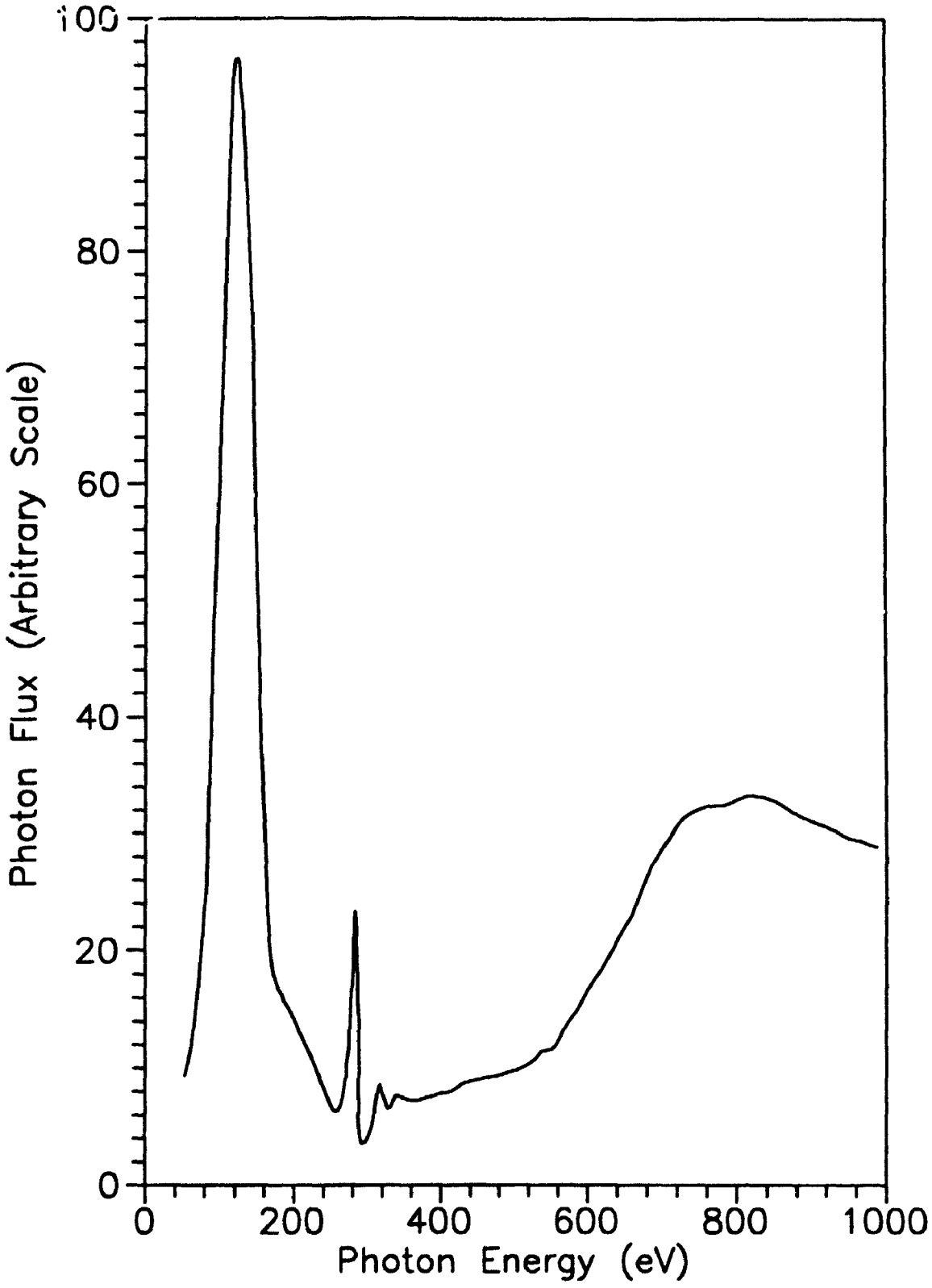
100
80
60
40
20
0
Photon Flux (Arbitrary Scale)
0
200
400
600
800
1000
Photon Energy (eV)

where d is the spacing between rulings on the grating in Å, α is the angle of incidence, R is the radius of the grating in mm and D and L_o are, respectively, the displacement and the zero position of the monochromator. From the positions of the absorption lines of known compounds, D and L_o can be calibrated thereby allowing direct calculation of the photon energy.

The monochromator is pumped by a Perkin Elmer Ultek TNB-X combination ion pump/titanium sublimator with a combined pumping speed of 4200 L/s. In addition there is a 25 L/s ion pump mounted at the grating to improve the vacuum in this region. The grating is separated from the sample chamber by a cryo pump to ensure that no material from the sample chamber contaminates the grating. The various sample chambers used in conjunction with this beamline all have their own pumping stations.

Section II-2; The Double Crystal Beamline.

In addition to the Grasshopper beamline the Canadian Synchrotron Radiation Facility (CSRF) also maintains a double crystal monochromator (DCM) on a separate beamline for higher energy (1750 to 3700 eV) spectroscopic studies. The DCM employs a Golovchenko-type boomerang mechanism[4] which mechanically links two InSb monochromator crystals for proper rotation and translation. In order to keep the position of the exit beam constant when the Bragg angle is scanned, the second crystal translates while simultaneously rotating to maintain a parallel configuration with the first crystal. The high-precision mechanics keep the second crystal parallel to the first within 13 μm throughout the full range of travel.

The throughput of the DCM is shown in Figure II-2 as a function of photon energy from 1750 eV to 3700 eV. The upper curve was recorded when the storage ring was operating at 1 GeV while the lower dashed curve corresponds to 0.8 GeV. The marked difference in throughput emphasizes the need for higher energy storage rings for this type of monochromator. With a ring current in the synchrotron of 100 mA at 1 GeV energy, the CSRF DCM beamline will deliver approximately $4X10^{10}$ photons/second at the silicon 1s edge (1840 eV) with a photon resolution of less than 0.8 eV.

Space limitations of the beamline (< 15 m including experimental station) dictated that the optical arrangement be one in which the monochromator came before the refocusing mirrors. As a result, the primary crystal bears a large heat load from the synchrotron which raises its temperature by several degrees celsius. The temperature of the primary

Figure II-2. The throughput of the CSRF Double Crystal beamline from 1750 eV to 3700 eV with InSb monochromator crystals. (Digitized from B.X. Yang *et al.*, Ref # 4)

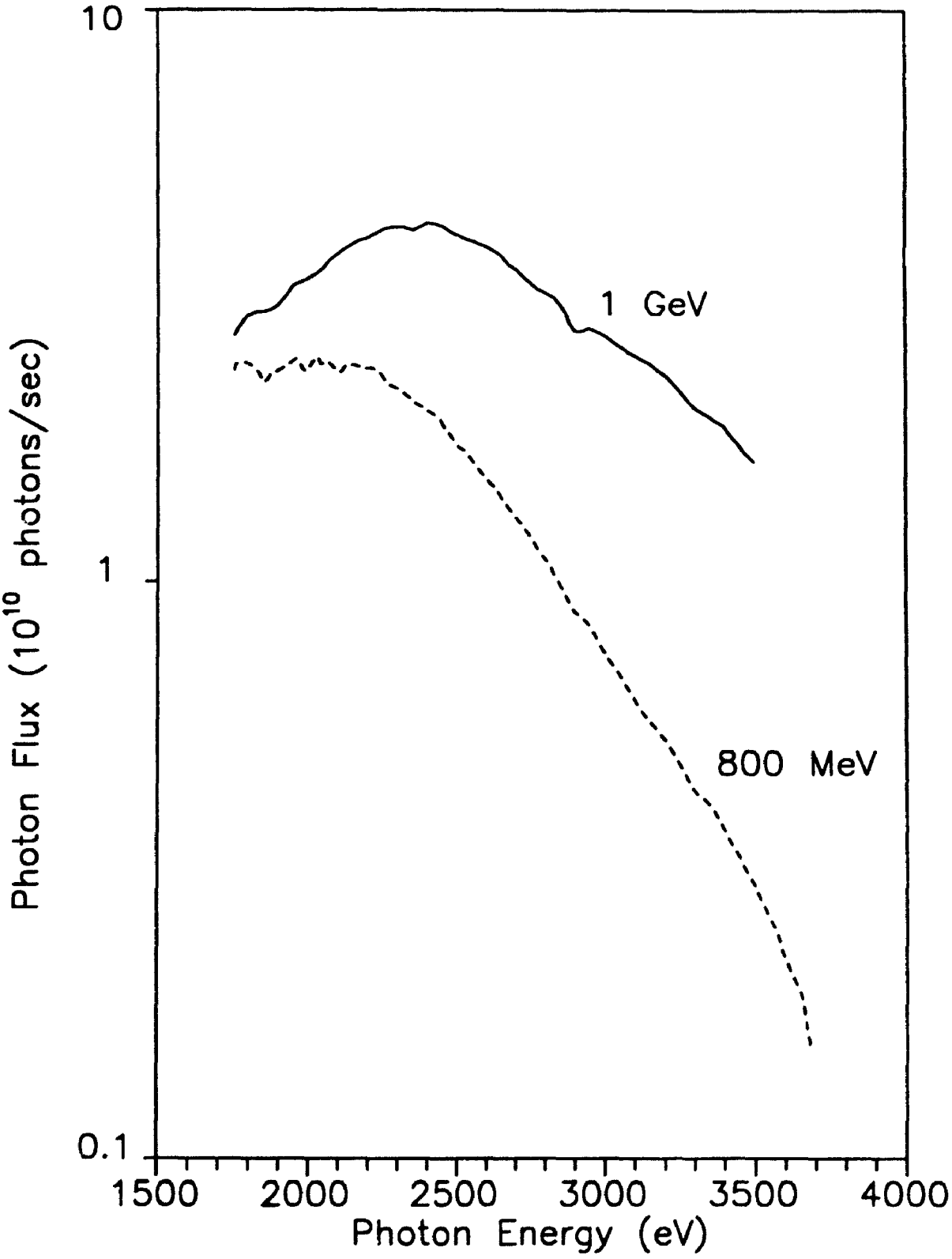
10
1
0.1
Photon Flux (10^{10} photons/sec)
1 GeV
800 MeV
1500
2000
2500
3000
3500
4000
Photon Energy (eV)

crystal is monitored and the secondary crystal is resistively heated to the same temperature to eliminate thermal variance in the two crystal lattices.

After emerging from the monochromator the divergent x-rays are focused by reflection from a refocusing mirror. At the focal point of this final mirror the spot size of the x-ray beam is less than 1mm in width and less than 3mm in height. During a full spectral scan (1.75 keV to 3.7 keV) the focal point of the entire optical system moves by less than 0.3 mm horizontally and less than 1 mm vertically.

User control of the beamline is achieved through the use of two IBM PC computers which operate as a slave/master team communicating with each other via an RS232 interface. Users bringing their own computer controlled equipment can access the system through one of two different ways. The user's computer can replace the master and control the slave computer directly or the master computer can control both the slave and user devices.

Section II-3; Photoabsorption.

Two different types of photoabsorption equipment were used in conjunction with the Grasshopper and the DCM respectively. Spectra of the Si 2*p* and 2*s* edges were recorded on the Grasshopper beamline in experiments which directly measured the attenuation of the radiation by the sample. Spectra of the Si 1*s* edge were recorded on the DCM beamline with a single ionization chamber.

On the Grasshopper, the high pressure (~40 milli torr) area of the sample chamber was separated from the optical components of the beamline by a carbon-polymer window which transmitted 85% of the radiation in the 100 to 200 eV region of the spectrum. The 30 cm pathlength of the sample chamber was pumped by a 330 L/s Balzer turbo molecular pump and the pressure was measured with an Edwards cold-cathode type device.

At the end of the sample chamber, opposite the carbon window, a gold diode was placed in the path of the radiation and was connected to the negative terminal of a 9 volt battery. A second terminal from the gold diode was fed into a Kiethly 4400 current amplifier, the output from which was then fed to a 32 bit analog to digital converter in the computer that controlled the monochromator. When the sample chamber was filled with the gas of interest the computer could record the current from the gold diode (and hence the attenuation of the radiation by the sample) as a function of the photon energy as set by the monochromator.

Background corrections due to changes in the beam intensity as a function of photon energy (see Figure II-1, Section II-1) were accounted for

by recording the background spectrum (when the sample chamber was empty) both before and after each spectrum was run. The two background spectra were digitally averaged and the final absorption, A, was calculated according to Equation II-3,

$$A = \text{Log}\ (I_o/I) \qquad \text{[Eq. II-3]}$$

where I_o is the averaged background from the empty chamber and I (which is proportional to the transmittance of the sample) is the current produced when the chamber is filled with the sample gas. From Equation II-3 the absorption, A, is a measure of the relative cross section of the sample; no effort was made to measure quantitatively the absolute cross sections of any of the compounds studied in this thesis.

The absorption spectra of the Si 1*s* edge were recorded on the DCM beamline using a 30 cm long single ionization chamber separated from the optical components of the beamline by a carbon-polymer window. In an ionization chamber[5] the sample gas is contained between two plates of opposite electrical charge. When the sample is ionized by the radiation the negatively charged particles are attracted to the positive plate and the positive ions are attracted to the negative plate thus producing a net flow of current between the two plates. A current thus produced is directly proportional to the absorption of the sample. The background was measured simultaneously by recording the current from a gold mesh placed in the path of the radiation prior to its interaction with the sample.

Section II-4; The Photoelectron Spectrometers.

All core-level photoelectron spectra in this thesis are of the Si 2*p* edge and as such were recorded on the Grasshopper beamline with a modified McPherson electron energy analyzer. The McPherson spectrometer has been described in detail by a number of thorough reports[6-8] and thus will only be treated briefly here. Essentially the McPherson consists of two concentric partial spheres with a mean radius of 36 cm. A gas cell and electron entrance slit (1 mm) is fitted at one end of the spheres in such a way that the synchrotron beam is directed across the face of the analyzer and entrance slit as shown in Figure II-3.

The entire analyzer is oriented in such a way that the x, y and z components of the electron acceptance angle are maximized at the pseudo magic angle position for a synchrotron beam of 90% polarized light. Because the degree of polarization changes only slightly as a function of photon energy the electron throughput is essentially maximized throughout the entire energy range of the system.

The gas cell is equipped with a rectangular light pipe (inner dimensions: 4 X 1 X 0.1 cm^3) used to reduce the flow of sample gas from the gas cell into the chamber. This allows pressures of approximately $1X10^{-3}$ torr inside the cell (in the interaction region) and a pressure of only $4X10^{-5}$ torr in the sample chamber. The sample chamber and the analyzer are both pumped by Balzer turbo molecular pumps with 330 and 550 L/s capacities respectively which keep pressures in the sample chamber and analyzer at $4X10^{-5}$ and $1X10^{-7}$ torr respectively during operation.

Figure II-3. Schematic representation of the McPherson photoelectron spectrometer at CSRF. (After Bozek *et al.*, Bozek, and Cutler; refs # 6-8).

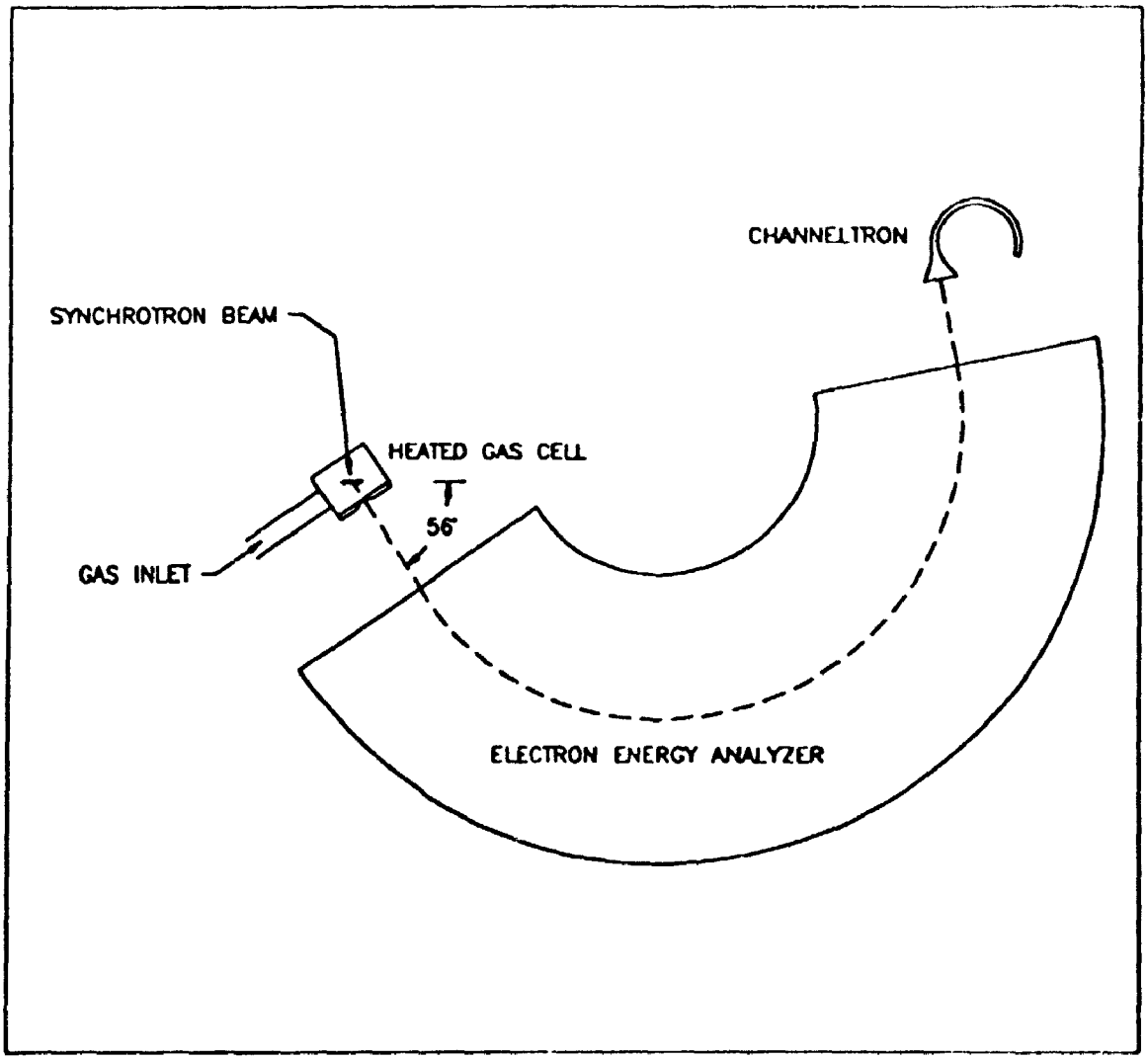
CHANNELTRON
SYNCHROTRON BEAM
HEATED GAS CELL
T
56°
GAS INLET
ELECTRON ENERGY ANALYZER

The gas inlet system in Figure II-3 can be replaced with a solid sample probe which can be used to record the spectra of volatile solids. The hollow tip of the probe can be packed with approximately 1g of solid sample which is then inserted into the gas cell. For this type of work the gas cell can be resistively heated to temperatures up to 110° C to increase the vapor pressure of the sample.

Detection of the electrons was achieved in one of two ways. Initially a channel electron multiplier (channeltron) was used in conjunction with a 1 mm electron exit slit and the voltage applied to the spheres was scanned to allow passage of electrons with different kinetic energies. To scan the spheres, the voltage would be held constant for a period of 1 second while the number of counts from the channeltron was recorded. The sphere voltage (and hence the electron kinetic energy) would then be changed by some increment and the number of counts at that energy would be recorded. The entire spectrum would thus be recorded by scanning through the energy region of interest several times. With 1 mm entrance and exit slits the theoretical electron resolution, $\Delta E/E$, was equal to 1/760 which is equivalent to an electron linewidth of 0.04 eV at 30 eV kinetic energy. In practice however, typical electron linewidths are assumed to be closer to 0.06 eV in accord with the data presented in Table I-1 of Chapter I.

In 1991 the electron exit slit and channeltron were replaced by a Quantar model 3395A position sensitive detector (PSD). This device records the number of electrons striking the detector as a function of their position on the detector surface. The detector surface is divided into 1024 channels thereby recording an entire range of electron kinetic energies simultaneously. The practical range of energies detected is a function of

the mean kinetic energy of the electrons. For instance, at low mean kinetic energies, the spatial dispersion of the electrons is greater than it would be at high mean kinetic energies. That is, it requires more channels to record a 1 eV range of photoelectrons whose average kinetic energy is 25 eV than it does to record a 1 eV range of photoelectrons with a mean kinetic energy of 100 eV.

For calibration purposes, the number of channels required to record a 1 eV range of energies was measured as a function of mean kinetic energy of the electrons. This was done by recording the photoelectron spectrum of the Xe 4*d* level at a range of different electron kinetic energies and then measuring the spin-orbit splitting of this level in terms of the number of channels separating the two peaks. For instance, at a mean kinetic energy of 25 eV the highest count rate for the $d_{3/2}$ peak was registered in channel number 227 while that of the $d_{5/2}$ peak was registered in channel number 810. Given that the spin-orbit splitting[7,8] of the Xe 4*d* level is 1.984 eV, this corresponds to (810-227)/1.984 = 294 channels/eV. It was found that the reciprocal of this (eV/channel) changes linearly with respect to the mean kinetic energy of the electrons. Table II-1 shows the values of channels/eV and eV/channel for a range of different mean kinetic energies and Figure II-4 shows a plot of eV/Channel VS Mean Kinetic Energy.

It was found that for a mean kinetic energy of 25 eV the "window" recorded by the PSD was approximately 3.5 eV wide (from 23.25 to 26.75 eV). Thus, spectra recorded over a sufficiently narrow range of kinetic energies, such as those of the Si 2*p* edge, could now be recorded in the so-called "snap-shot mode" without scanning the voltages on the spheres. The decreased data acquisition time with the PSD meant that the slit widths on the monochromator could be reduced, giving lesser intensity but increased

Figure II-4. A plot of (eV/Channel) VS (Mean Kinetic Energy) for the Quantar 3395A position sensitive detector.

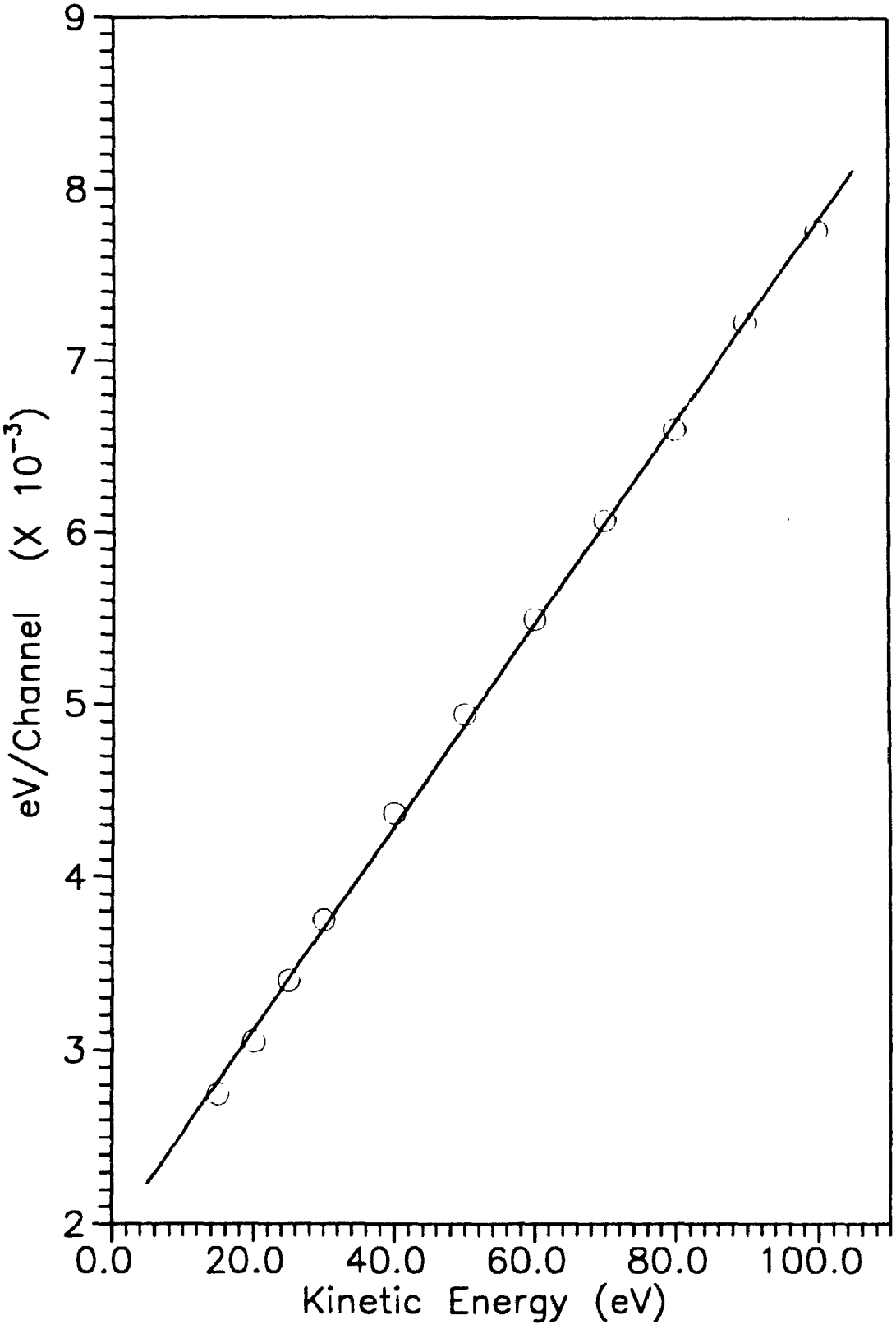
9
8
7
6
5
4
3
2
eV/Channel (X 10^{-3})
0.0
20.0
40.0
60.0
80.0
100.0
Kinetic Energy (eV)

resolution. An example of this improvement is shown in Figure II-5 which depicts the raw data for the Si 2*p* photoelectron spectra of Si_2H_6 recorded with the channeltron and with the PSD. The improved count-rate, greater number of data points and improved resolution with the PSD make obvious the peaks and shoulders due to vibrational splitting in this molecule. The details of this spectrum are discussed in Chapter V.

Table II-1. The number of PSD channels/eV and the number of eV/channel as a function of the mean kinetic energy of the photoelectrons.

Mean K.E. (eV)	Channels/eV (/eV)	eV/Channel (eV X 10^{-3})
15.0	364	2.75
20.0	328	3.05
25.0	294	3.40
30.0	267	3.75
40.0	229	4.37
50.0	202	4.94
60.0	182	5.49
70.0	165	6.07
80.0	152	6.61
90.0	139	7.22
100.0	129	7.76

Some of the valence band photoelectron spectra in Chapter VI (those with photon energies of 21.8 eV) were recorded on a commercial laboratory photoelectron spectrometer essentially identical to the one described above but equipped with a He discharge lamp as the ionizing source. This instrument[9] is a McPherson ESCA 36 photoelectron spectrometer which has been modified to accommodate gaseous samples and volatile solids. The original DEC computer and data acquisition system has been replaced with an IBM PC identical to that used at the CSRF.[6-8]

Figure II-5. The Si 2*p* photoelectron spectrum of Si_2H_6 recorded with the PSD (top curve) and with the channeltron (bottom curve).

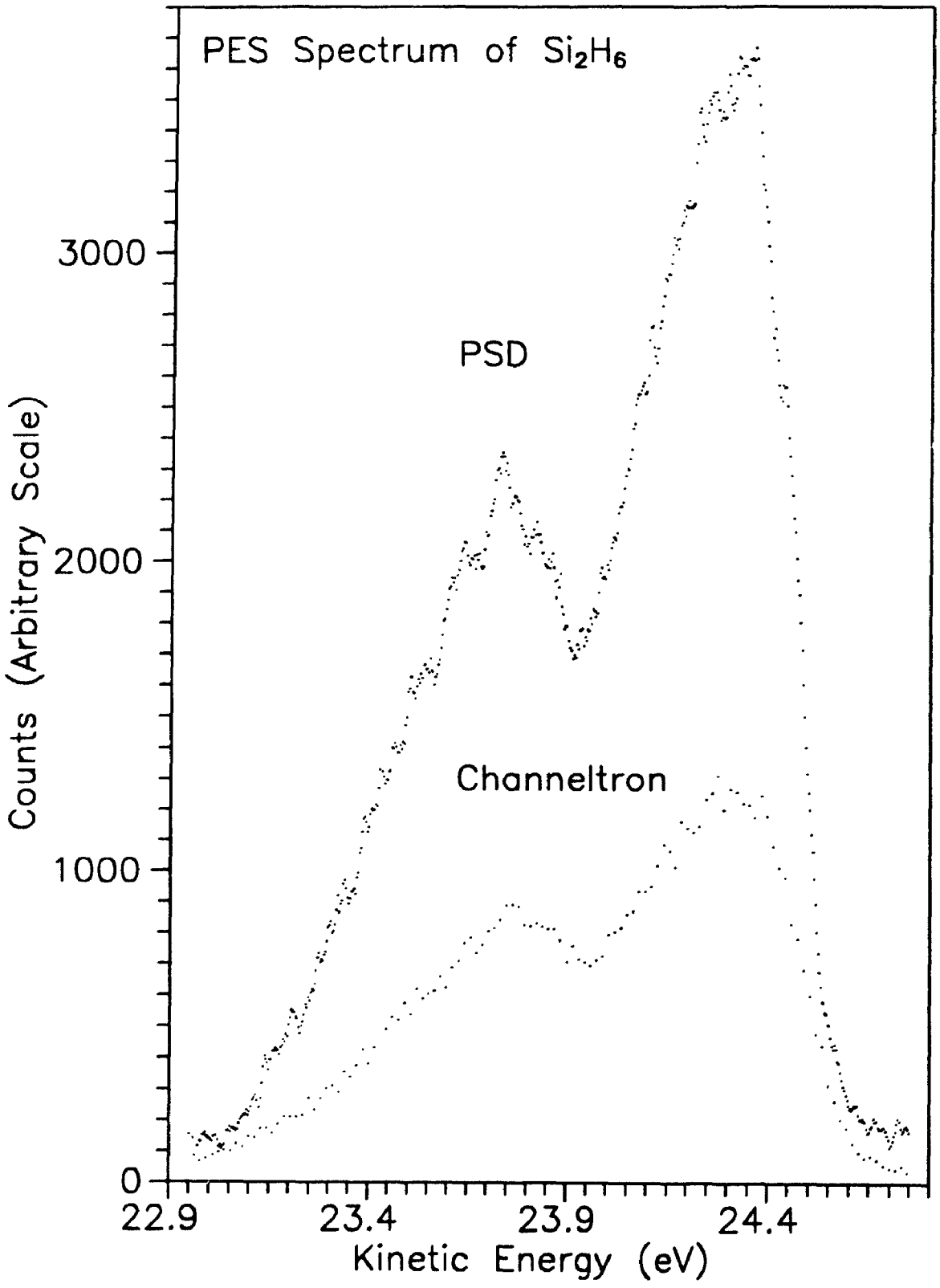
PES Spectrum of Si_2H_6
PSD
Channeltron
Counts (Arbitrary Scale)
3000
2000
1000
0
22.9
23.4
23.9
24.4
Kinetic Energy (eV)

Section II-5; References.

1) F.C. Brown, R.Z. Bachrach, S.B.M. Hagstrom, N. Lien and C.H. Pruett; *Vacuum Ultraviolet Radiation Physics*, Ed. E. Koch, Pergamon Press, New York, (1974)

2) F.C. Brown, R.Z. Bachrach, and N. Lien; Nuc. Inst. Meth., **152**, 73, (1978)

3) K.H. Tan, G.M. Bancroft, L.L. Coatsworth and B.W. Yates; Can. J. Phys., **60**, 131, (1981)

4) B.X. Yang, F.H. Middleton, B.G. Olsson, G.M. Bancroft, J.M. Chen, T.K. Sham, K.H. Tan and D.J. Wallace;, Nuc. Instr. & Meth., ???, ???, (1992)

5) J. Berkowitz, *Photoabsorption, Photoionization and Photoelectron Spectroscopy*, Academic Press, New York, (1979), p408.

6) J.D. Bozek, J.N. Cutler, G.M. Bancroft, L.L. Coatsworth, K.H. Tan and D.S. Yang; Chem. Phys. Lett., **165**, 1, (1990)

7) J.D. Bozek, Ph.D. Thesis, University of Western Ontario, London, Ontario, Canada, (1991)

8) J.N. Cutler, Ph.D. Thesis, University of Western Ontario, London, Ontario, Canada, (1992)

9) G.M. Bancroft, I. Adams, D.K. Creber D.E Eastman and W. Gudat; Chem. Phys. Lett., **38**, 83, (1976).

CHAPTER III:

VIBRATIONAL EFFECTS IN THE Si 2p PRE-EDGE PHOTOABSORPTION SPECTRA OF SiH_4, SiD_4, Si_2H_6 AND Si_3H_8.

Section III-1; Introduction.

The Si 2*p* pre-edge photoabsorption spectrum of SiH_4 was first reported by Hayes and Brown[1,2] and their original interpretation was then modified using theoretical calculations by Schwarz[3], Friedrich[4] *et al* and Robin[5]. Although the spectrum of SiD_4 has never been re. .ded to confirm the various interpretations, all reports agree that both symmetric and asymmetric vibrational modes are excited upon transitions to the lower Rydberg states (approximately 105 eV) in the pre-edge spectrum of SiH_4. Furthermore, there is a general consensus that transitions to higher Rydberg states (those that approach the ionization threshold) do not lead to the excitation of vibrational modes. The excitation of the symmetric vibrational mode in the Si 2*p* *photoelectron* spectra of SiH_4[6-9] and SiD_4[7] has been reported which has led to the suspicion of the existence of vibrational excitations throughout the phot. bsorption spectra of the higher Rydberg states of these molecules. Furthermore, the possible existence of asymmetric vibrational modes in the photoabsorption spectra brings into question the fits that have been assigned to the *photoelectron* spectra of SiH_4 and SiD_4 which do not include asymmetric vibrations.

The molecules disilane (Si_2H_6) and trisilane (Si_3H_8), because of their high symmetry, fall into a special category. Both these molecules contain two symmetrically equivalent cores and this leads to a unique spectral profile in their core-level spectra due to localization of the core hole on only one Si center. This "core-hole localization"[10] results in a lowering of the excited state symmetry of the molecule which allows coupling

between electronic and non-totally symmetric vibrational modes of the molecule. Although the theory of this phenomena was developed in the mid 1970's, because of technical difficulties in achieving sufficient resolution only three experimental reports of this have been cited in the literature.[11-14]

In this chapter the high resolution (~0.05 eV) Si *2p* pre-edge photoabsorption spectra of both SiH_4 and SiD_4 are presented thereby allowing the assignment of both the Rydberg levels and the vibrational excitations in these spectra. The photoabsorption spectra of disilane (Si_2H_6) and trisilane (Si_3H_8) are also reported. The asymmetric Si-H vibrations, found in the spectrum of the two-centered molecule disilane, provide perhaps the best example of core hole localization and vibronic coupling in core-level spectroscopy reported thus far.

Section III-2; Experimental.

All samples were purchased commercially and used without further purification. The photoabsorption spectra were recorded in the gas-phase with a path length of 30 cm and a gas pressure of 30 milli torr. The attenuation of the radiation by the sample was measured by monitoring the electrical current from a gold diode placed at the end of the gas cell. Spectra were recorded with and without the sample present to allow for background correction. All spectra were recorded using the CSRF Mark IV Grasshopper monochromator[15] at the Aladdin synchrotron of the University of Wisconsin at Madison. The monochromator employs an 1800 groove/mm grating which yields a minimum practical photon resolution of 0.05 eV at 105 eV photon energy.

Section III-3; Silane and Silane-d4.

Figure III-1 shows the Si 2*p* photoabsorption spectra of SiH_4 (top) and SiD_4 (bottom) plotted on the same axes from 102 to 109 eV and Figure III-2 gives an expanded version of the 3.5 eV region between 104.5 and 108.0 eV with major peaks labeled A to T. The exact positions of most major peaks were determined from the first derivative of the spectra and the positions and assignments are summarized in Table III-1. The spectrum of SiH_4 is in good qualitative agreement with all previously published work in this field, but our higher intensity and higher resolution results in the observation of new features. Combined with the isotope shifts from SiD_4 we have been able to give a more precise assignment for the Rydberg and vibrational peaks in the Si 2*p* pre-edge photoabsorption spectrum of these molecules. The excellent resolution is demonstrated by the separation of peaks B and C in SiD_4 (Table III-1, Figure III-2) which have an energy difference of only 66 meV.

Comparing our results more closely with those of Brown's[2] (Table III-1) we see that the major peak positions are in very good agreement. For example, positions of peak maxima for the initial peaks B to H (Figure III-2) are all within 20 meV of Browns and subsequent peaks J to P are all within 40 meV. Because our photon flux is at least 4 orders of magnitude greater than that used by Brown we have observed new features such as peaks A and I, and the higher energy peaks Q to T that are previously unreported. Furthermore, more accurate measurement, via photoelectron spectroscopy[6-9], of physical parameters such as the spin-orbit splitting (0.613 eV),

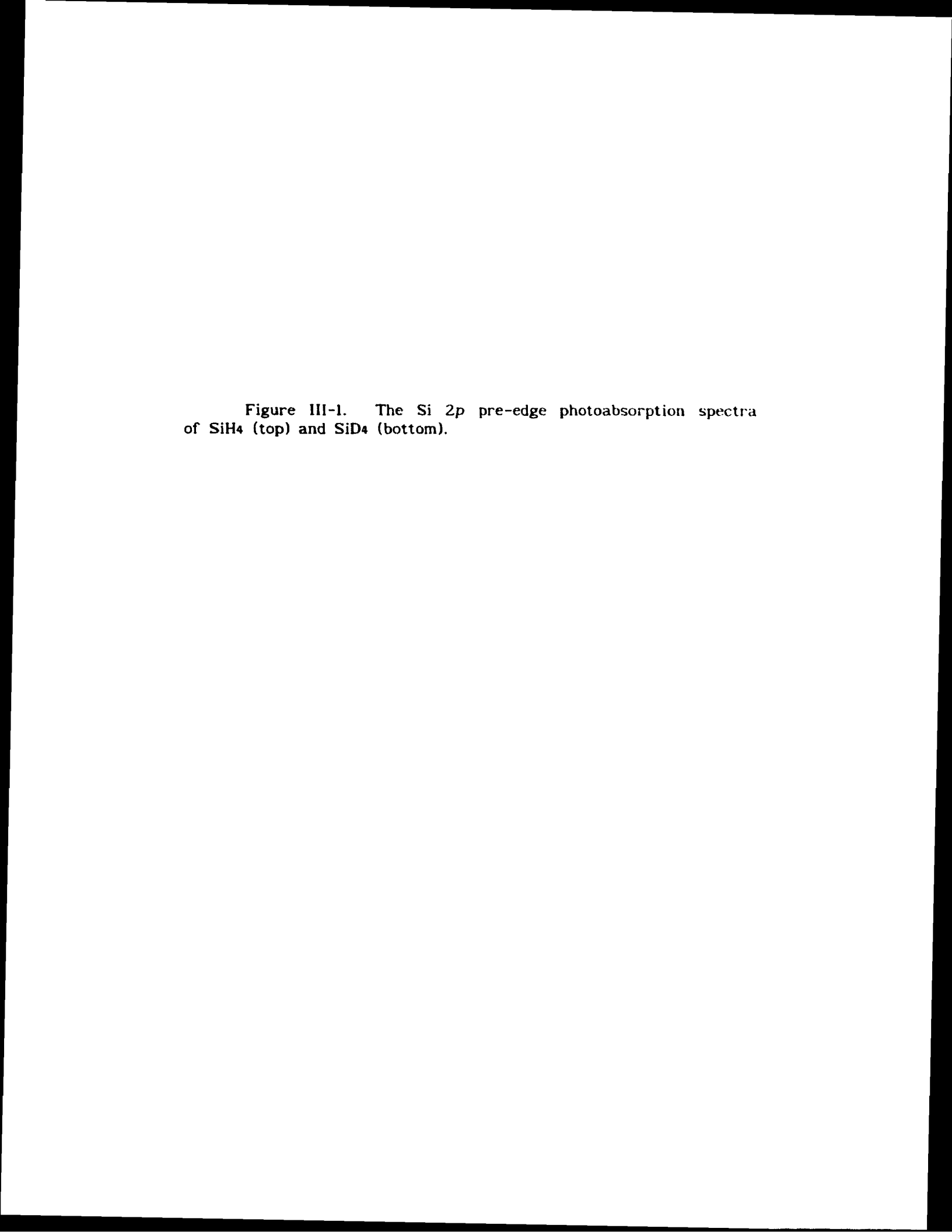

Figure III-1. The Si 2*p* pre-edge photoabsorption spectra of SiH_4 (top) and SiD_4 (bottom).

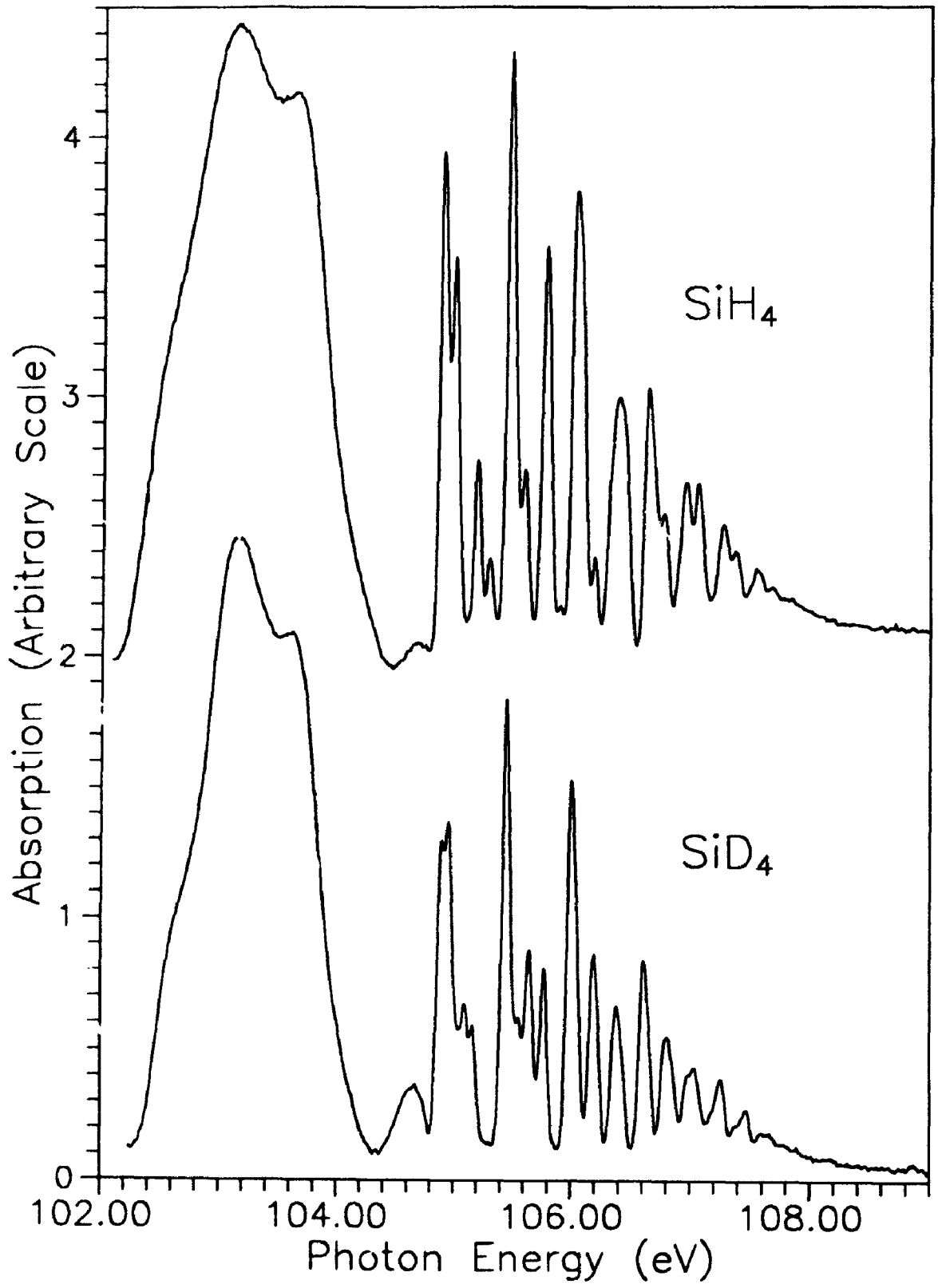
Absorption (Arbitrary Scale)
0
1
2
3
4
SiH4
SiD4
102.00
104.00
106.00
108.00
Photon Energy (eV)

Figure III-2. Si 2*p* photoabsorption spectra of silane (top) and silane-d_4 (bottom). The positions of the Rydberg levels and their spin-orbit counterparts (solid horizontal lines numbered I-II) and the positions of vibrational excitations (solid vertical lines) and their spin-orbit counterparts (dashed vertical lines) numbered, where space permits, according to the Rydberg (I to II) or is spin-orbit counterpart (I' to II') from which they originated. The subscripts "a", "s" and "o" designate, respectively, asymmetric, symmetric and overtone vibrations.

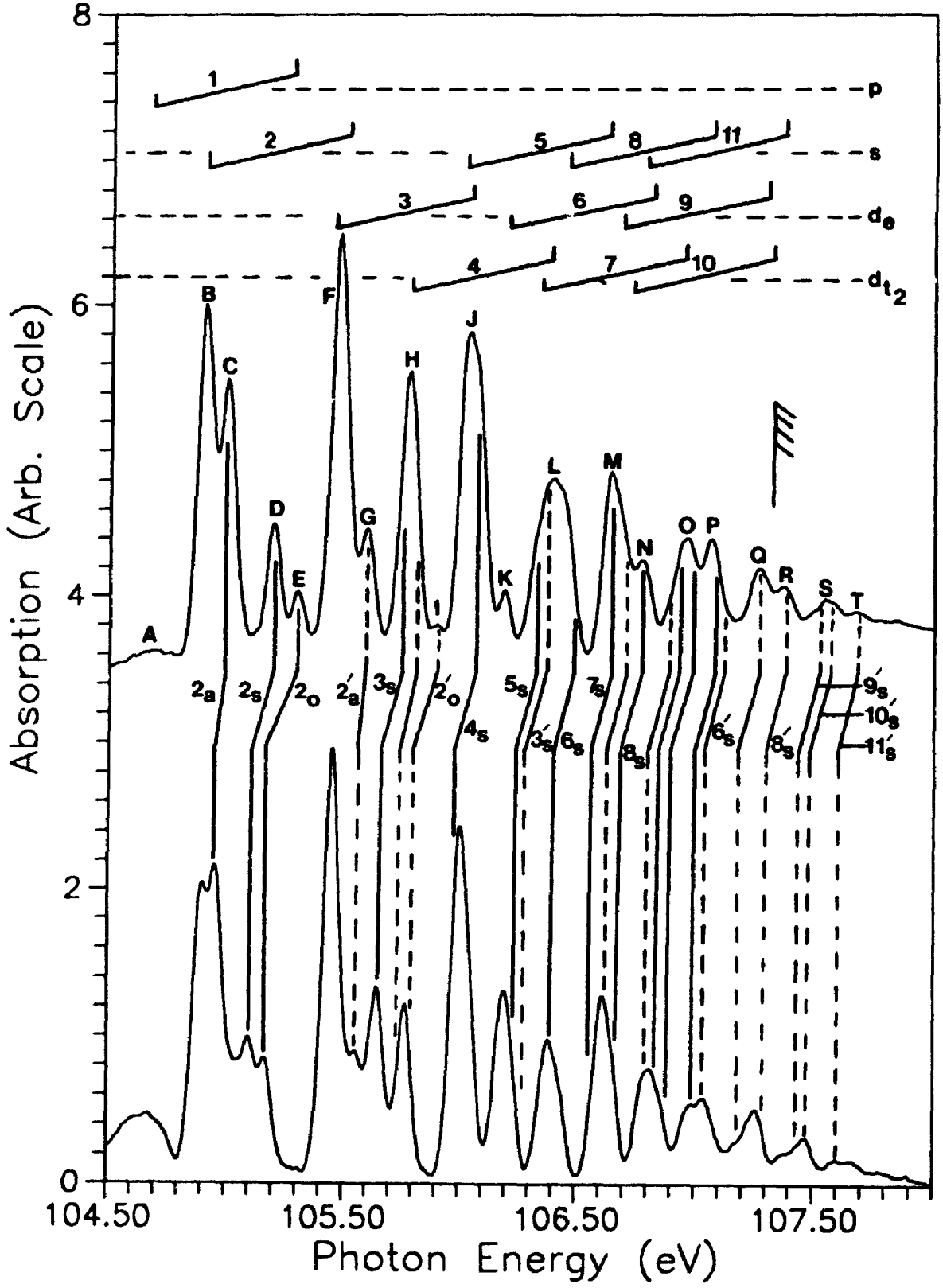
Absorption (Arb. Scale)
Photon Energy (eV)
104.50
105.50
106.50
107.50
0
2
4
6
8
p
s
d_e
d_t2
A
B
C
D
E
F
G
H
I
J
K
L
M
N
O
P
Q
R
S
T
2a
2s
2o
2'a
3s
2'o
4s
5s
3's
6s
7s
8s
6's
8's
9's
10's
11's

Table III-1. The peaks from Figure III-2, their respective positions, positions from previous work and assignments. (a=asymmetric; s=symmetric; o=overtone).

			Position (eV)			Assignment	
Peak	Ryd.#	Vib.#	SiH_4	SiD_4	Hayes[2]	$2p_{3/2}\rightarrow$	$2p_{1/2}\rightarrow$
A	1	-	104.661	104.662	-	4*p*	
B	2	-	104.902	104.901	104.92	5*s*	
C	-	2_a	105.001	104.967	-	a vib on 2	
D	-	2_s	105.197	105.110	-	s vib on 2	
E	-	2_o	105.300	105.176	-	o vib on 2	
F	3	-	105.45	105.45	105.52	3*d*(e)	
	2'	-	105.51	105.51	105.52		5*s*
G	-	2_a'	105.61	105.56	-		a vib on 2'
H	-	3_s	105.75	105.66	-	s vib on 3	
	4	-	105.78	105.78	105.84	3*d*(t2)	
	-	2_s'	105.81	105.73	-		s vib on 2'
I	-	2_o'	105.91	105.80	-		o vib on 2'
J	5	-	106.01	106.01	106.06	6*s*	
	3'	-	106.07	106.07	106.10		3*d*(e)
	-	4_s	106.07	105.99	-	s vib on 4	
K	6	-	106.19	106.19	-	4*d*(e)	
L	-	5_s	106.30	106.22	-	s vib on 5	
	7	-	106.36	106.36	106.45	4*d*(t2)	
	-	3_s'	106.36	106.24	-		s vib on 3'
	4'	-	106.39	106.39	106.45		3*d*(t2)
	8	-	106.47	106.47	106.50	7*s*	
	-	6_s	106.48	106.40	-	s vib on 6	
M	5'	-	106.62	106.62	106.68		6*s*
	9	-	106.65	106.65	106.69	5*d*(e)	
	-	7_s	106.66	106.58	-	s vib on 7	
	-	4_s'	106.68	106.60	-		s vib on 4'
	10	-	106.69	106.69	-	5*d*(t2)	
N	-	8_s	106.76	106.68	-	s vib on 8	
	11	-	106.78	106.78	106.78	8*s*	
	6'	-	106.80	106.80	-		4*d*(e)
O	-	5_s'	106.92	106.84	-		s vib on 5'
	-	9_s	106.95	106.87	-	s vib on 9	
	7'	-	106.97	106.97	107.02		4*d*(t2)
	-	10_s	106.98	106.90	-	s vib on 10	
P	8'	-	107.08	107.08	107.09		7*s*
	-	11_s	107.08	107.00	-	s vib on 11	
	-	6_s'	107.09	107.01	-		s vib on 6'
Q	9'	-	107.26	107.26	-		5*d*(e)
	-	7_s'	107.27	107.19	-		s vib on 7'
	10'	-	107.30	107.30	-		5*d*(t2)
R	-	8_s'	107.38	107.30	-		s vib on 8'
	11'	-	107.40	107.40	-		8*s*
S	-	9_s'	107.56	107.48	-		s vib on 9'
	-	10_s'	107.59	107.51	-		s vib on 10'
T	-	11_s'	107.69	107.61	-		s vib on 11'

vibrational splitting (0.295 eV) and the Si $2p$ ionization threshold (107.316 eV) has lead to a better interpretation of the peak assignments in the photoabsorption spectrum of SiH_4.

The broad peak centered at 103.2 eV in Figure III-1 has been assigned[4] to a total of four transitions from the Si $2p_{3/2}$ and the $2p_{1/2}$ core levels to the $4s\sigma^*$ and $3p\sigma^*$ valence anti-bonding orbitals. Figure III-2 shows the spectrum of SiH_4 (top) and SiD_4 (bottom) from 104.5 to 108.0 eV with Rydberg levels (numbered 1 to 11) marked above the two spectra. Their corresponding spin-orbit counterparts, although not numbered separately on Figure III-2, have been assigned the numbers 1' to 11' in Table III-1. The peaks that result from Si-H and Si-D vibrations have been connected by solid lines (numbers 1 to 11) or dashed lines (1' to 11') according to the Rydberg transition or spin-orbit splittings from which they originated. Each vibration in Figure III-2 is assigned one of three subscripts "a", "s" or "o" which denote, respectively, asymmetric, symmetric or overtone vibrations. The positions of all Rydberg and vibrational excitations are tabulated in Table III-1. Because the first five peaks in Figure III-2 each result from only a single transition they are reported with greater accuracy than subsequent transitions, the exact positions of which are more difficult to measure.

The assignment of Rydberg states in this work agrees most closely with that of the original work by Hayes and Brown[1,2] with four notable exceptions:

(1) They assigned the broad peak at ~103 eV to Rydberg transitions. This has been shown[3,4] to result from transitions to anti-bonding orbitals.

(2) Three new Rydberg states have been added; numbers 1, 6 and 10 in Figure III-2.

(3) The added information provided by the spectrum of SiD_4 has allowed for much more precise determination of the exact positions of Rydberg levels within a given peak.

(4) Most importantly, unlike all previous interpretations of the spectrum of SiH_4 (in which it was concluded that there were no vibrational excitations associated with the higher Rydberg levels), comparison with the spectrum of SiD_4 clearly shows that there are pronounced vibrational effects right up to threshold and beyond. This is in accord with the fact that the Si-H(D) symmetric vibrational mode has been observed[6-9] in the Si 2*p* photoelectron spectra of these molecules.

With the exception of the first Rydberg transition (peak A in Figure III-2 is discussed below), the remaining Rydberg levels have been divided into three categories: those that are of *s*-character and those that are of *d*-character, the latter being split into E and T_2 symmetry as suggested by Schwarz[3]. The positions of each of the Rydberg states, shown in Figure III-2, has been calculated using the simple formula[2],

$$(n-\delta)=[R/(A-E_n)]^{1/2} \qquad \text{[Eq. III-1]}$$

where n is the principle quantum number, δ is the quantum defect, R is a Rydberg (13.6 eV) and $(A-E_n)$ is the term value where A is the ionization limit and E_n is the position of the Rydberg state. Because δ is constant for a given series, $(n-\delta)$ should change by a value of unity for successive Rydberg states in the same series. Table III-2 shows the different series to which each Rydberg state belongs as well as the values for all the terms in equation III-2. From Table III-2, the average change in the value of

$(n-\delta)$ is 0.895. Deviations from the ideal value of unity may result from partial mixing between Rydbergs and anti-bonding orbitals.

Table III-2. The positions of the different Rydberg lines from Figure III-2 in order of increasing energy for the four different Rydberg series, term values and average quantum defects.

Series	Rydberg	E_n	$(A-E_n)$	n	δ	$(n-\delta)$	Avg. δ
p	1	104.661	2.65	4	1.73	2.27	1.73
s	2	104.902	2.41	5	2.62	2.38	-
	5	106.01	1.31	6	2.77	3.23	-
	8	106.47	0.87	7	3.03	3.97	-
	11	106.78	0.53	8	2.92	5.08	2.84 ± 0.18
d(e)	3	105.45	1.87	4	1.30	2.70	-
	6	106.19	1.13	5	1.52	3.48	-
	9	106.65	0.67	6	1.46	4.54	1.43 ± 0.11
d(t2)	4	105.78	1.55	4	1.03	2.97	-
	7	106.36	0.96	5	1.22	3.78	-
	10	106.69	0.63	6	1.33	4.67	1.19 ± 0.15

Peak A in Figure III-2 at 104.661 eV is previously unobserved in SiH_4 and is approximately 8-fold more intense in SiD_4. Robin[5] has suggested that the first peak in this region should be due to the $2p \rightarrow 4p$ transition but erroneously[4] assigned this transition to peak B in Figure III-2. From CI calculations Friedrich[4] *et al* predict the first Rydberg line at ~104.5 eV (very close to the value of 104.661 eV for peak A), but go on to say that as a result of its $2p \rightarrow 4p$ character the intensity is too low to be observed. We therefore assign peak A to the first Rydberg line resulting from a transition from a Si $2p$ core to a $4p$-type Rydberg; however, other Rydberg states of p-character are too weak to be observed. The increased intensity

in SiD_4 is unexplained. The fact that a *p* to *p* transition is allowed at all is unusual and may be due to a distortion of the molecular symmetry that occurs upon core-ionization.

Peak B results from a transition to Rydberg # 2 which is of 5*s* character. The vibrational excitations arising from this transition are beautifully demonstrated by the isotopic shifts in the positions of peaks C, D and E in Figure III-2. Peak C results from the excitation of the asymmetric Si-H bending mode associated with Rydberg # 2. Peak D results from the excitation of the symmetric Si-H stretching mode and peak E is a vibrational overtone that results from the excitation of both stretching and bending modes associated with Rydberg # 2. Other Rydberg levels of *s*-character are numbers 5, 8 and 10; see Table III-2.

The frequency of the Si-H symmetric stretching vibration, 0.295 eV, (the difference between peaks B and D) is identical to the value of the Si-H stretching frequency measured from photoelectron spectroscopy (see Chapter V) which is perhaps surprising considering that the transition from which this vibration arises is 2.4 eV below threshold. Similarly the values of 0.209 eV and 0.212 eV for the Si-D vibrational frequency as measured, respectively, by photoabsorption and photoelectron spectroscopy are in excellent agreement. Furthermore, the measurement of the Si-D vibrational frequency as measured by both techniques is predicted exactly by Equation III-2,

$$\nu(\text{Si-D})/\nu(\text{Si-H}) = [\mu(\text{Si-H})/\mu(\text{Si-D})]^{1/2} \qquad \text{[Eq. III-2]}$$

where ν is the vibrational frequency and μ is the reduced mass.

The frequency of the Si-H asymmetric bending mode (the difference

between peaks B and C or between peaks D and E) has an average value of 0.102 eV in SiH_4 and 0.066 eV in SiD_4; again, in excellent agreement with equation III-2. Although this vibrational mode has not been observed in the photoelectron spectra of either SiH_4 or SiD_4 the photoelectron spectrum of disilane[9], SiH_3-SiH_3, does exhibit a vibrational progression with an energy spacing of 0.102 eV and this value is further confirmed by the long vibrational progression in the photoabsorption spectrum of this molecule (see Figure III-3).

Peak G in Figure III-2 is the spin-orbit counterpart of peak C and the previously unobserved peak I is the spin-orbit of peak E. Beyond peak I (~105.9 eV) there is no definite evidence of the Si-H asymmetric bending vibration; this vibrational mode seems to be associated only with the $2p \rightarrow 5s$ transition but due to the complexity of the spectrum, better resolution is required to confirm this.

The spectrum of SiD_4 has also been extremely useful in assigning the position of more subtle vibrational effects such as peak H in Figure III-2. The fact that there is vibrational structure in this peak only becomes obvious when it is compared to the corresponding position in the spectrum of SiD_4. Here we see that peak H is comprised of more than just a single Rydberg transition, as was suggested previously[1-6], and actually contains a significant amount of vibrational structure. For proper interpretation and assignment of these spectra, a comparison of different regions of the two spectra shown in Figure III-2 makes clear the need to include vibrational excitations throughout the pre-edge region.

Section III-4; Disilane and Trisilane.

Figure III-3 shows the photoabsorption spectra of disilane (Si_2H_6) and trisilane (Si_3H_8) plotted on the same axes; the data is summarized in Table III-3. Both spectra have the same general profile but the rich vibrational structure seen in disilane is much less evident in trisilane. It is immediately obvious that the vibrational progression in disilane is radically different from that of the single-centered molecule SiH_4. None the less, there are some similarities.

Peak 1 in disilane has been assigned to the same core to anti-bonding transitions as in SiH_4: namely $2p \rightarrow 4s\sigma^*$ and $2p \rightarrow 3p\sigma^*$. The 0.4 eV shift of this peak to lower energy (relative to the corresponding peak in SiH_4) is commensurate with the chemical shift (0.3 eV)[7] expected when a Si-H bond is replaced by a Si-Si bond. If peak 1 in disilane is aligned with the corresponding peak in SiH_4 (Figure III-1) then peaks 2 through 5 correspond very closely to the position of Rydberg states as determined from the photoabsorption spectra of SiH_4 and SiD_4. The shoulder inbetween peaks 1 and 2, at ~104.0 eV in Figure III-3, may correspond to the Si $2p \rightarrow 4p$ Rydberg transition (peak A, Figure III-2) barely observable in SiH_4. Peak 2 in Figure III-3 corresponds exactly with the Si $2p \rightarrow 5s$ transition in the spectrum of SiH_4 (peak B, Figure III-2) and peaks 3, 4 and 5 in disilane (Figure III-3) result from transitions to higher Rydberg levels. Peaks 3, 4 and 5 (Figure III-3) each show rich vibrational structure which, as in SiH_4 and SiD_4, continues right up to the ionization threshold and beyond. In particular, the vibrational manifold on peak 3 has a shape very

Figure III-3. The Si 2*p* photoabsorption spectra of disilane (top) and trisilane (bottom) from 101.5 to 108.5 eV. Peak 1 results from transitions to anti-bonding orbitals while peaks 2-5 result from Rydberg transitions.

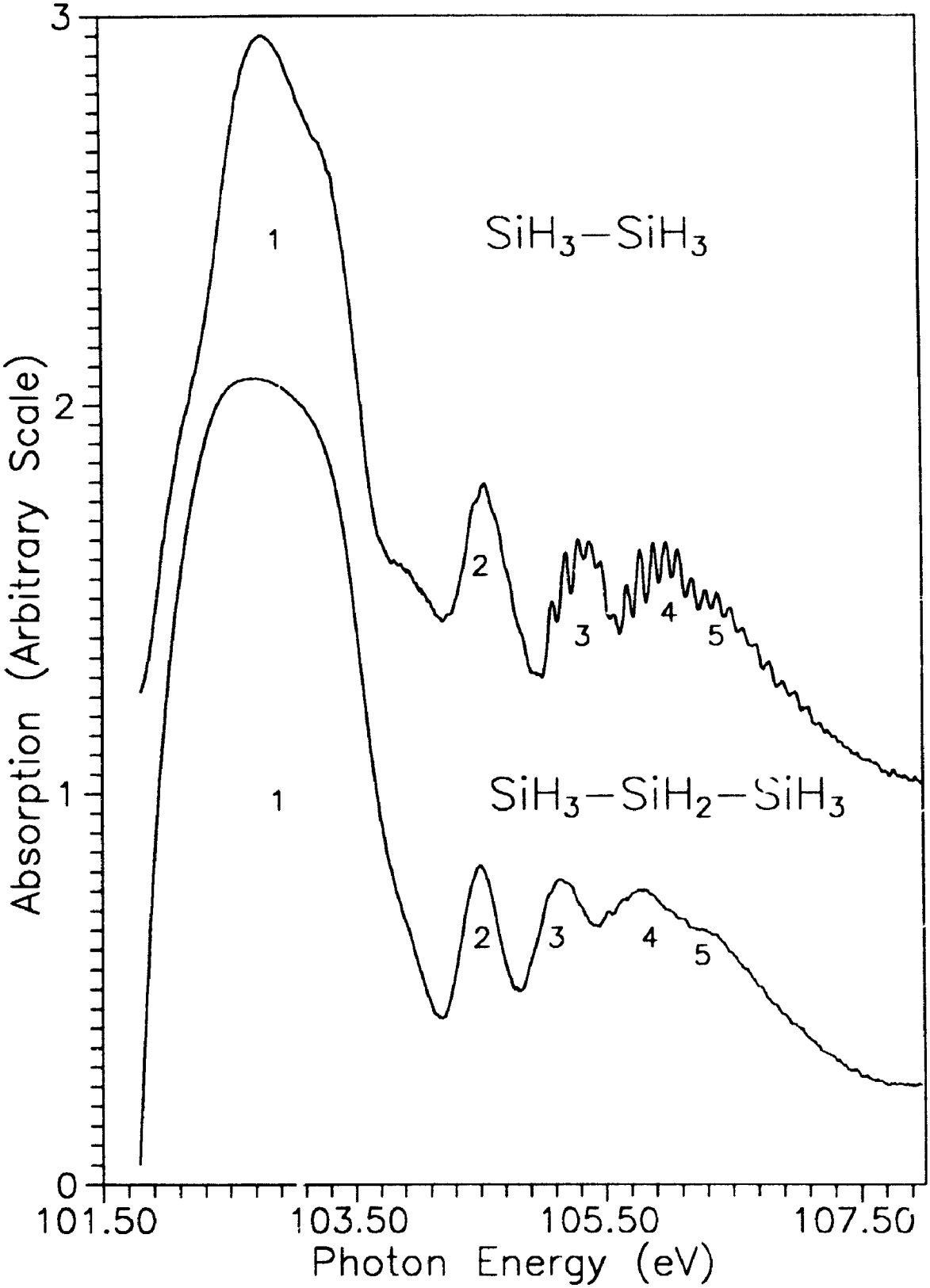
3
2
1
0
Absorption (Arbitrary Scale)
101.50
103.50
105.50
107.50
Photon Energy (eV)
SiH3—SiH3
SiH3—SiH2—SiH3
1
2
3
4
5
1
2
3
4
5

similar to that found in the photoelectron spectrum[9] of this compound. More importantly, the vibrational energy spacing in these peaks is exactly the same as that found in the photoelectron spectrum of disilane (0.102 eV or 827 cm^{-1}).

Table III-3 Positions of maxima in Si 2*p* photoabsorption spectra of disilane and trisilane.

Molecule	Peak	Position of First Vibration (eV)	Position of Maxima (eV)
Si_2H_6	1	-	102.79
	2	104.25	104.54
	3	105.08	105.29
	4	105.68	105.88
	5	-	106.30
Si_3H_8	1	-	102.69
	2	-	104.49
	3	-	105.13
	4	-	105.77
	5	-	106.26

The theory of vibrational structure in the core-level photoelectron and photoabsorption spectra of small molecules has been studied extensively from a theoretical[10] point of view. Because the theory for photoelectron and photoabsorption spectroscopy is essentially the same, no distinction between the two will be made here and the theories thus detailed will be equally applicable to the photoelectron results presented in Chapter V

The theory of vibronic coupling, which leads to the excitation of asymmetric vibrational modes, in core level spectroscopy was first discussed by Domcke and Cederbaum[10e,10f] in 1977. They suggested that the core level

spectra of molecules with two or more equivalent cores (such as the O 1s spectrum of CO_2) would exhibit the asymmetric vibrational mode as a result of vibronic coupling due to core-hole localization. However, it took until 1989[11] for technology to catch up to the point where the C 1s photoabsorption spectra of simple hydrocarbons (C_2H_2, C_2H_4, C_2H_6 and C_6H_6) could be recorded with sufficient resolution to observe the vibrational fine structure in their spectra.[11-14] The C 1s photoabsorption spectra of these molecules did indeed exhibit the excitation of the C-H asymmetric stretching frequency and thus vindicated the theory of Domcke and Cederbaum that was set down more than a decade earlier. Recently the Si 2*p* photoelectron spectrum of disilane[12] (Si_2H_6), the silicon analog of ethane, has been recorded with sufficient resolution to detect the excitation of asymmetric Si-H stretching modes in the photoelectron spectrum of this molecule; this was the first example of this effect in photoelectron spectroscopy (see Chapter V).

The complete Hamiltonian for the system in question can be written as,

$$\hat{H} = \hat{H}_E + \hat{H}_N + \hat{H}^1_{EN} + \hat{H}^2_{EN} \qquad \text{[Eq. III-3]}$$

where the first term, $\hat{H}_E$, describes the electronic motion when the nuclei are fixed at the Hartree-Fock (HF) ground state geometry. The second term, $\hat{H}_N$, describes the motion of the nuclei in the harmonic HF potential and the last two terms, $\hat{H}^1_{EN}$ and $\hat{H}^2_{EN}$, represent the coupling of the HF particles with the nuclear motion.[10b] Because the last term, $\hat{H}^2_{EN}$, is very small only the

third term in Equation III-3, $\hat{H}^{1}_{EN}$, is considered when discussing the coupling between electronic and vibrational modes.[10f]

The transition operator $\hat{T}$, relates to the promotion of an electron from some initial state *i* to some final state *j*. In the one-particle approximation of the occupation number representation[10c] $\hat{T}$ can be written as the product of electron creation and annihilation operators. For the photoelectron experiment where the electron is ejected, the transition operator would be written as,

$$\hat{T} = \alpha_i \hat{a}_i \qquad \text{[Eq. III-4]}$$

where $\hat{a}_i$ and α_i are, respectively, the annihilation operator for the particle in the one-particle state |i> and the matrix element for this process. In the case of photoabsorption where the electron is merely promoted to an excited state, $\hat{T}$ can be written as,

$$\hat{T} = \alpha_{ij} \hat{a}^{\dagger}_j \hat{a}_i \qquad \text{[Eq. III-5]}$$

where $\hat{a}^{\dagger}_j$ is the electron creation operator and, *i* and *j* represent the

initial and final one-particle states $|i\rangle$ and $|j\rangle$. The annihilation and creation operators can be written as a function of the normal vibrational coordinates of the molecule, Q_s (where s=1 to 3N-6), according to Equations III-6 and III-7.

$$\hat{a}_i(Q_s) = \sum_k \langle \phi_i(Q_s) | \phi_k(0) \rangle \hat{a}_k \qquad \text{[Eq. III-6]}$$

$$\hat{a}_i^+(Q_s) = \sum_k \langle \phi_k(0) | \phi_i(Q_s) \rangle \hat{a}_k^+ \qquad \text{[Eq. III-7]}$$

Using this formalism and $\hat{b}_s$ and $\hat{b}_s^+$, the annihilation and creation operators for vibrational quanta of the s^{th} normal mode, the three terms in Equation III-3 can be written[10f] according to Equations III-8, III-9 and III-10.

$$\hat{H}_E = \sum_i \varepsilon_i(0) \hat{a}_i^+ \hat{a}_i \qquad \text{[Eq. III-8]}$$

$$\hat{H}_N = \sum_s \omega_s (\hat{b}_s^+ \hat{b}_s + 1/2) \qquad \text{[Eq. III-9]}$$

$$\hat{H}_{EN} = \sum_i \sum_s 2^{-1/2} (\delta\varepsilon_i / \delta Q_s)_0 [\hat{a}_i^+ \hat{a}_i - n_i](\hat{b}_s + \hat{b}_s^+) \qquad \text{[Eq. III-10]}$$

where $\varepsilon_i(0)$ is the energy of the i^{th} orbital in the HF ground state, ω_s is the vibrational frequency of the s^{th} vibrational mode, n_i is the occupation number (n=0 or 1 in the one-particle approx.) and the other symbols retain their previously ascribed definitions.

Within the adiabatic approximation, $\hat{H}_{EN}$ now represents the coupling between the electronic and vibrational quantum states. However, for those vibrational modes which are not totally symmetric, the derivative $(\delta\varepsilon_i/\delta Q_s)_0$ in Equation III-10 is identically zero and thus there can be no linear coupling to vibrational modes of non-totally symmetric states. Thus the coupling to asymmetric vibrational modes is a second order phenomenon and the inclusion of non-adiabatic effects hinges upon the dependence of the electron annihilation and creation operators, $\hat{a}_i$ and $\hat{a}_i^+$, on the normal coordinates of the vibrational modes, Q_s. Thus, from Equation III-7,

$$\frac{\delta}{\delta Q_s}\hat{a}_i^+(Q) = \sum_k \langle\phi_k(0)|\frac{\delta}{\delta Q_s}|\phi_i(Q)\rangle\hat{a}_k^+ \qquad \text{[Eq. III-11]}$$

Given the fact that $|\phi_i(Q_s)\rangle$ obey the Schrodinger equation it is possible to write

$$\hat{H}_{el}(Q)|\phi_i(Q)\rangle = \varepsilon_i(Q)|\phi_i(Q)\rangle \qquad \text{[Eq. III-12]}$$

after which the matrix element in the right hand side of Equation III-11 becomes,[10f]

$$\langle \phi_k(Q) | \frac{\delta}{\delta Q_s} | \phi_i(Q) \rangle = \frac{\langle \phi_k(Q) | \delta \hat{H}_{el} / \delta Q_s | \phi_i(Q) \rangle}{\varepsilon_i(Q) - \varepsilon_k(Q)} \qquad \text{[Eq. III-13]}$$

Combining Equations III-13 and III-11 (in which you sum over <u>all</u> of the states k) it is obvious that the derivative of the electronic operators $\hat{a}_i^+$ and $\hat{a}_i$ (and hence the probability of exciting asymmetric vibrations) may become large if there exists two orbitals, $\varepsilon_i(Q)$ and $\varepsilon_k(Q)$ that are close in energy.

Disilane belongs to the D_{3h} point group and the 2 sets of $2p$ orbitals will form four molecular orbitals; namely a σ_g and σ_u will be formed from the two $2p_z$ orbitals and a π_g and π_u will be formed from the four $2p_x$ and $2p_y$ atomic orbitals. Considering a transition from the $2p$ σ orbital (the theory for the π-orbitals is analogous), it follows from Equation III-13 that the matrix element, $\langle \phi_{\sigma_g} | \frac{\delta}{\delta Q_u} | \phi_{\sigma_u} \rangle$ where Q_u denotes the normal coordinates of the asymmetric vibrational modes, may be very large due to the near degeneracy of the σ_g and the σ_u orbitals. The non-diagonal matrix elements of $\delta/\delta Q_g$ however, where Q_g denotes the coordinates of the symmetric vibrational modes, will all be zero because, $\langle \phi_{\sigma_g} | \frac{\delta \hat{H}_{el}}{\delta Q_g} | \phi_{\sigma_u} \rangle = 0$ due to the odd parity of the integral.

From symmetry considerations, taking $\phi_k(Q)=\sigma_g$ and $\phi_l(Q)=\sigma_u$ (which have, respectively, A_{1g} and A_{2u} symmetry), the matrix element in Equation III-13 can only have a non-zero value if $\delta\hat{H}_{el}/\delta Q_s$ transforms as the A_{2u} irreducible representation. That is, only the ν_6 vibrational mode of A_{2u} symmetry can couple these two electronic states. From the infrared spectrum[16,17] of disilane the frequency of the A_{2u} vibrational mode absorbs at 844 cm^{-1} which is only slightly higher than the frequency of 827 cm^{-1} observed in the Si 2*p* photoabsorption spectrum (Figures III-3, and III-4) of this molecule. Although it is unusual to have a vibrational frequency in the core-ionized species that is lower than that of the same vibrational mode in the neutral molecule, these findings are in accord with the C 1*s* spectra of the symmetrically equivalent molecules C_2H_6 and C_2D_6. Data for the A_{2u} vibrational mode of all three molecules is presented in Table III-4.

Table III-4. Vibrational frequencies for the A_{2u} mode in the neutral molecule and in the core-ionized species of ethane, ethane-d_6 and disilane.

Molecule	M-H bending Freq.[a]	Vib. Freq. of Ion[b]
CH_3-CH_3	1379 cm^{-1}	1290 cm^{-1}
CD_3-CD_3	1077 cm^{-1}	1048 cm^{-1}
SiH_3-SiH_3	844 cm^{-1}	827 cm^{-1}

(a) Observed infrared bending mode of A_{2u} symmetry where M= C or Si Data taken from ref.#17

(b) Observed vibrational frequency in the core-level photoabsorption spectrum; frequencies for ethane and ethane-d_6 were calculated from data presented in ref. # 13.

Unlike the disilane σ_{pz} molecular orbitals, which are of exactly the same symmetry as the σ_s orbitals in ethane, the Si $2p$ atomic orbitals combine in disilane to also form π_{Dxy} bonding and anti-bonding molecular orbitals that are of E_g and E_u symmetry respectively. Accordingly, the symmetry selection rules in Equation III-13 will be different here and it is found that the $2p$ π molecular orbitals can be coupled by any of the asymmetric vibrational modes; namely the A_{1u}, A_{2u} or the E_u. However, from the infrared data the vibrational frequency of the A_{1u} and the E_u modes is, respectively, ~200 cm^{-1} and 2179 $cm.^{-1}$ But, the long unbroken vibrational progression in the spectrum of disilane suggests the presence of only a single vibrational mode, and based on this, it is concluded that only vibrations of A_{2u} symmetry are excited in the Si $2p$ pre-edge photoabsorption spectrum of disilane.

Another difference between the spectrum of C_2H_6 and Si_2H_6 is that in the former the vibrational envelope is quite small, where as the long progression of the asymmetric vibrational mode in disilane is perhaps the best example of this phenomenon recorded to date. Also different from the spectrum of ethane is the fact that the totally symmetric Si-H vibration, which is coupled linearly to the electronic transition, is not observed in either the photoabsorption or the photoelectron spectrum of this compound where as the C-H symmetric vibration is clearly evident in the C $1s$ spectrum of ethane. However there is evidence of the symmetric Si-Si vibration in Figure III-4.

Figure III-4 shows an expansion of the region from 104.0 to 107.5 eV for disilane and trisilane. Vibrational effects on peak 2 are apparent only as weak shoulders but become evident in the first derivative which is plotted on the same x-axis in Figure III-4. Because peak 2 has

Figure III-4. An expansion of the region from 104.0 to 107.5 eV for disilane (top) and trisilane (bottom). The first derivative of peak 2 in disilane shows vibrational structure with an average energy spcaing of 0.056 eV.

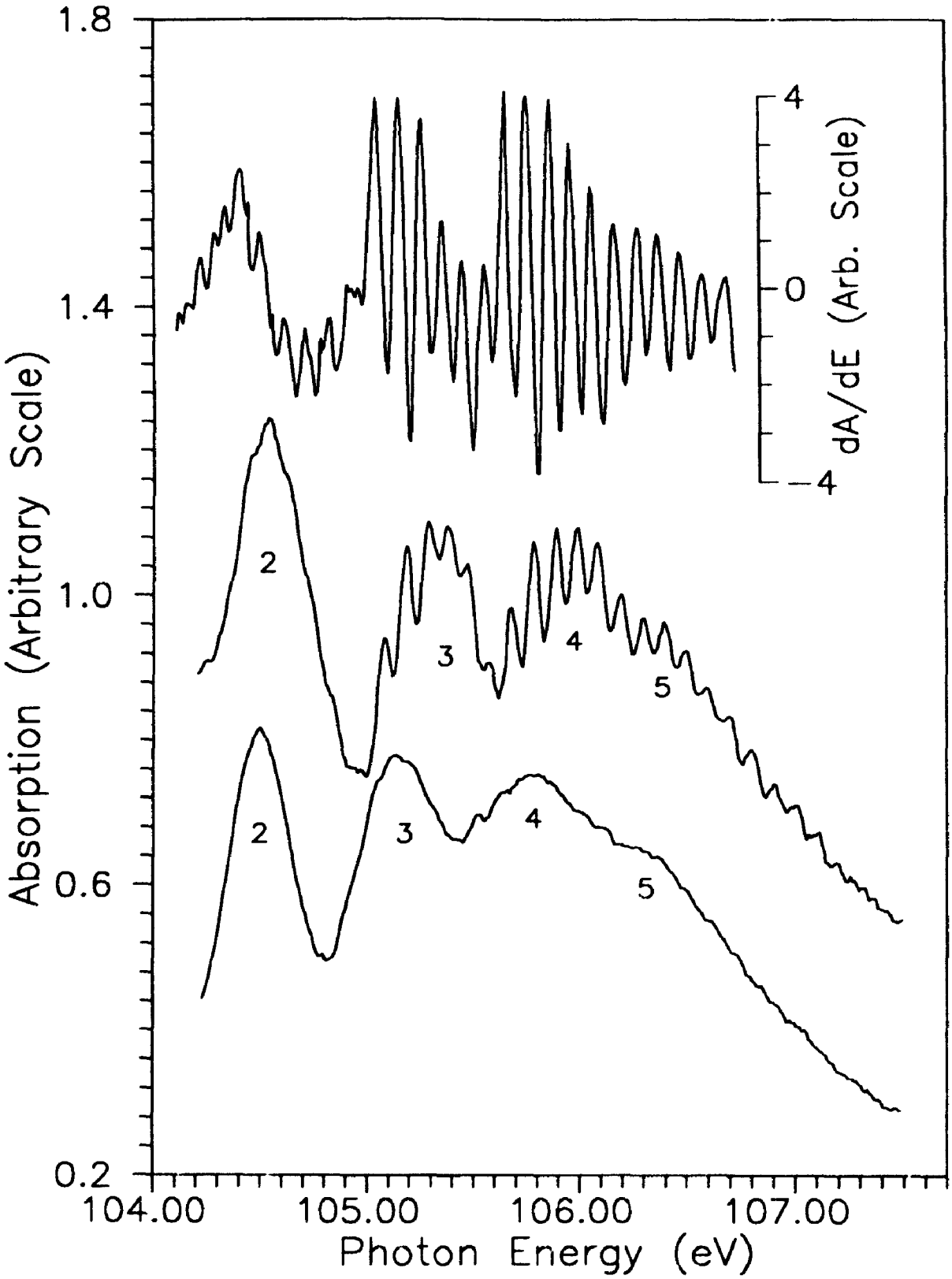
1.8
1.4
1.0
0.6
0.2
Absorption (Arbitrary Scale)
104.00
105.00
106.00
107.00
Photon Energy (eV)
4
0
−4
dA/dE (Arb. Scale)
2
3
4
5
2
3
4
5

approximately the same linewidth as peak 3 (where vibrational structure is clearly resolved) the vibrational energy spacing on peak 2 must be considerably less than the 102 meV measured for peaks 3, 4 and 5. The average energy spacing between maxima in the first derivative of peak 2 is 56 meV - very close to the 53.9 meV (434 cm^{-1}) for the Si-Si vibrational stretching mode as measure by infrared spectroscopy[17]. It is interesting to note that in both SiH_4 and Si_2H_6 that transitions from $2p \rightarrow 5s$ result in the excitation of unexpected vibrational modes: in SiH_4 the asymmetric Si-H bending mode is excited and in Si_2H_6 the Si-Si stretching mode is excited. These two vibrational modes may be present on other transitions in these two molecules but, because of the complexity of the spectra better resolution is needed to resolve this issue.

The spectrum of trisilane is essentially the same as that of disilane but with attenuated vibrational resolution. The obvious shoulders on peak 1 in disilane become washed out in the spectrum of trisilane (Figure III-3) due to the fact that there are Si atoms in two different chemical environments in this molecule. The expansion of peaks 2 through 5 (Figure III-4) does show some evidence of vibrational structure in peaks 3, 4 and 5 but even the first derivative (not shown) does not show a regularly repeating vibrational frequency. This is likely caused by interference resulting from the two different chemical environments of Si and the resultant difference in the types of Si-H bond in this molecule. Further complications may arise as a result of Si-Si vibrations in this molecule, especially in peak 2.

Section III-5; References.

1) W. Hayes, F.C. Brown and A.B. Kunz; Phys. Rev. Lett., **27**, 774, (1971)

2) W. Hayes and F.C. Brown; Phys. Rev. A, **6**, 21, (1972)

3) W.H.E. Schwarz; Chem. Phys. **11**, 217, (1975)

4) H. Freidrich, B. Sonntag, P. Rabe, W. Butscher and W.H.E. Schwarz; Chem. Phys. Lett., **64**, (1979)

5) M.B. Robin; Chem. Phys. Lett., **31**, 140, (1975)

6) J.D. Bozek, G.M. Bancroft, J.N. Cutler and K.H. Tan; Phys. Rev. Lett., **65**, 2757, (1990).

7) D.G.J. Sutherland, G.M. Bancroft and K.H. Tan; Surf. Sci. Lett., **262**, L96, (1992)

8) Z.F Lui, G.M. Bancroft, J.N. Cutler, D.G.J. Sutherland, J.S. Tse, R.G. Cavell and K.H. Tan; Phys. Rev. A, **46**, 1688, (1992).

9) D.G.J. Sutherland, G.M. Bancroft and K.H. Tan; J. Chem. Phys., **97(11)**, 7918, (1992).

10) a) L.S. Cederbaum and W. Domcke; Chem. Phys. Lett., **25(3)**, 357,(1974).

b) L.S. Cederbaum and W. Domcke; J. Chem. Phys. **60(7)**, 2878, (1974).

c) L.S. Cederbaum and W. Domcke; J. Chem. Phys. **64(2)**, 603, (1976).

d) L.S. Cederbaum and W. Domcke; J. Chem. Phys. **64(2)**, 612, (1976).

e) L.S. Cederbaum and W. Domcke; J. Chem. Phys. **66(11)**, 5084, (1977).

f) W. Domcke and L.S. Cederbaum; Chem. Phys. **25**, 189, (1977)

11) Y. Ma, F. Sette, G. Meigs, S. Modesti and C.T. Chen; Phys. Rev. Lett., **63**, 2044, (1989).

12) F.X. Gadea, H. Köppel, J. Schirmer, L.S. Cederbaum, K.J. Randall, A.

Bradshaw, Y. Ma, F. Sette, and C.T. Chen; Phys. Rev. Lett., 66, 883, (1991).

13) Y. Ma, C.T. Chen, G. Meigs, K.J. Randall, and F. Sette; Phys. Rev. A, **44(3)**, 1848, (1991).

14) M. Tronc, G.C. King and F.H. Read; J. Phys. B, **12**, 137, (1992)

15) K.H. Tan, G.M. Bancroft, L.L. Coatsworth, and B.W. Yates; Can. J. Phys., **60**, 131, (1982)

16) H.S. Gutowsky and E.O. Stejskal; J. Chem. Phys., **22**, 939, (1954)

17) G.W. Behtke and M.K. Wilson; J. Chem. Phys., **26**, 1107, (1957)

CHAPTER IV

Si L- and K-Edge XANES of Gas-Phase $Si(CH_3)_X(OCH_3)_{4-X}$: Models For Solid State Analogs

Section IV-1; Introduction.

Largely due to its importance in the semi-conductor industry, the Si L-edge and valence band spectra of SiO_2 have been a topic of continued interest throughout the past 25 years[1-9]. The tetrahedral symmetry of SiO_2 enables a molecular-orbital interpretation of the electronic structure[1] and most of the theoretical work has centered on the SiO_4^{-4} ion[10,11]. This ion however is not a particularly good model for SiO_2 for two reasons.[10] First, it is an ion with a large negative charge, and second, unlike SiO_2 where each O is bonded to two Si's, the oxygen atoms in SiO_4^{4-} each have a single dangling bond.

Surprisingly, very little work has been done to compare gas-phase analogs and solid state spectra. Dehmer[1] has compared the Si 2*p* photoabsorption XANES spectra of gaseous $SiCl_4$ and SiF_4 to that of solid state SiO_2 and SiF_6^{2-} to demonstrate the similarities between the tetrahedral and octahedral symmetries. In doing so, he showed that the spectra of the gas-phase compounds and the solid state SiO_2 are qualitatively similar. Furthermore, he was able to delineate the correspondence between the energies of the molecular orbitals of Si compounds with different symmetries (octahedral versus tetrahedral). More recently Filatova *et al.*[7] have published a similar comparison of the L-edge spectrum of SiO_2 and the solid state spectra of SiF_4 and SiH_4.

For reasons unknown, no investigation has been made of the more obvious analog, tetramethoxy silane, $Si(OCH_3)_4$. The tetrahedral arrangement of four oxygens around the silicon atom is identical to that in the SiO_2

structure, and the four methyl groups simulate the environment of a second Si bonded to each O. For these reasons it is felt that this is a far superior experimental model than $SiCl_4$, SiF_4 or SiH_4, and possibly a better theoretical model than SiO_4^{4-}.

This chapter presents: first, a complete analysis of the high resolution photoabsorption XANES spectra of the Si 1s, 2s and 2p edges of the five compounds in the series $Si(CH_3)_X(OCH_3)_{4-X}$; second, the theoretical cross section calculations of the two end members of the series, tetramethyl silane (TMS, $Si(CH_3)_4$) and tetramethoxy silane (TMOS, $Si(OCH_3)_4$); and third, a comparison of the gas-phase spectra with existing spectra of solid state analogs (ie. silicon carbide and silicon dioxide). The objectives of this chapter are three-fold: first, to show that the gas-phase XANES spectra of $Si(OCH_3)_4$ and $Si(CH_3)_4$ are indeed excellent analogs for the Si 2*p* spectra of the solid state compounds SiO_2 and SiC respectively. The second objective was to show that the MS-Xα cross section calculations of the molecular spectra can readily explain both the gas-phase and the solid state spectra. The third and final objective of this chapter was to show that the L-edge spectra of the compounds MO_4 (M= Si, P, S, Cl) are all qualitatively similar and can be explained analogously.

Section IV-2; Experimental and Theoretical.

All samples were purchased commercially from Huls America with purity greater than 99% and used without further purification. The photoabsorption spectra of the Si 2s and 2p edges of all five compounds were recorded in the gas-phase with a path length of 30 cm and a gas pressure of 30 milli torr. The attenuation of the radiation, I, by the sample was measured by monitoring the electrical current from a gold diode placed at the end of the gas cell. The background, I_o, for each spectra was determined separately by recording the spectrum of the evacuated cell both before and after recording the spectra of the compound. The two background spectra were then averaged and the final absorption, A, was calculated via Equation IV-1.

$$A=\log(I_o/I) \qquad \text{[Eq. IV-1]}$$

All L-edge spectra were recorded using the CSRF Mark IV Grasshopper monochromator[12] at the Aladdin synchrotron of the University of Wisconsin at Madison. The monochromator employs an 1800 groove/mm grating which yields a minimum practical photon resolution of 0.05 eV at 105 eV photon energy. The accuracy of the monochromator was calibrated by recording the position of the Kr $3d_{5/2}$ edge which has a binding energy of 93.798 eV.[13] The peak positions of the spectra in this chapter are accurate to within ±0.05 eV.

The five spectra of the Si 1s region were recorded in the gas-phase with a path length of 50 cm using a single ionization chamber on the CSRF Double Crystal[14] beam line at the Aladdin Synchrotron at the University of

Wisconsin. The Double Crystal monochromator employs twin InSb crystals and has a resolution of better than 0.80 eV at the Si 1*s* edge (approximately 1840 eV). Both I and I_o were measured simultaneously and the final absorption, A, was calculated from Equation IV-1. Calibration of the monochromator was done by recording the Si 1*s* spectrum of $SiCl_4$ and comparing this to previously published work.[15,16] Peak positions are accurate to within ± 0.1 eV.

The photoelectron spectrometer used to record the valence band spectrum of $Si(OCH_3)_4$ has been described in detail elsewhere.[17] Briefly, the spectrometer consists of a McPherson 36 cm mean radius electron energy analyzer with 1mm entrance and exit slits resulting in a theoretical electron resolution, $\Delta E/E$, of ~1/720. For electron kinetic energies of ~100 eV the theoretical value of ΔE is ~0.14 eV. Assorted differential pumping was used on the spectrometer and beamline to isolate the high pressure of the gas cell from the optical components of the beamline.

The L-edge solid state XANES spectrum of SiO_2 was recorded on the CSRF grasshopper beamline and the K-edge spectrum was recorded on the CSRF DCM beamline. The spectra of other solid state compounds, $((Ca)_3(PO_4)_2$, Na_2SO_4 and $NaClO_4$), were all recorded on the CSRF grasshopper beamline. All spectra were recorded in the total electron yield mode.[18]

Theoretical results, oscillator strengths and continuum cross sections of the Si 1s, 2s and 2p edges for the two molecules TMS ($Si(CH_3)_4$) and TMOS ($Si(OCH_3)_4$), were carried out using the MS-Xα method[19] and the continuum cross section program of Davenport[20]. The true symmetry of TMOS is S_4 which is not amenable to the MS-Xα technique and so the calculations on this molecule were carried out in C_{2v} symmetry. The calculations for TMS were carried out in the true tetrahedral symmetry. In both cases a Latter

tail[21] was added to account for the potential's asymptotic behavior at large distances.

Structural data for these two molecules was obtained from gas-phase electron diffraction studies,[22] and was used to calculate the atomic positions for the calculations. The values used for the sphere size, atomic exchange parameters and l_{max} values for all regions are listed in Table IV-1. The cross section and oscillator strength calculations for all edges were carried out using a converged transition state potential created by removing half an electron from the appropriate core-level in the ground state. All processes allowed by the dipole selection rules were included in the bound state and continuum cross section calculations.

Table IV-1: The sphere radii, α values and initial and final state values of l_{max} for the calculations of the two molecules $Si(OCH_3)_4$ and $Si(CH_3)_4$.

				l_{max}	
Molecule	Region	Radius (au)	α	Initial	Final
$Si(OCH_3)_4$	Outer Sphere	6.42	0.7545	4	7
	Si	1.99	0.7275	3	5
	O_1	1.43	0.7445	2	4
	O_2	1.43	0.7445	2	4
	C_1	1.51	0.7593	2	4
	C_2	1.51	0.7593	2	4
	H_1	1.04	0.7772	0	2
	H_2	1.04	0.7772	0	2
	H_3	1.01	0.7772	0	2
	H_4	1.01	0.7772	0	2
$Si(CH_3)_4$	Outer sphere	5.70	0.7620	4	6
	Si	2.06	0.7275	3	5
	C	1.48	0.7593	2	4
	H	1.00	0.7772	0	2

Section IV-3; Si 2p-Edge

Figure IV-1 shows the Si 2*p* and 2*s* XANES photoabsorption spectra of the five compounds in the series $Si(CH_3)_X(OCH_3)_{4-X}$ from 90 to 190 eV. All five spectra are superimposed upon the background of a decreasing valence cross section. Because the decrease in the valence cross section is much greater for O in this region than it is for C, the effect of the background becomes less prominent as the number of methoxy groups in the molecule decreases.

The overall shapes of the five spectra in Figure IV-1 are very similar to each other and to the spectra of other silicon-containing[1,23,24] molecules such as $SiCl_4$ and SiF_4. The peaks at ~114 and ~128 eV are labeled G and H respectively, (labels A to F are reserved for the pre-edge features in Figure IV-2) and are present in all five spectra with peak H shifting slightly to lower energy as the more electronegative methoxy groups are replaced with methyl groups (see Table IV-2). Features resulting from transitions of the Si 2*s* electrons at ~155 eV are not labeled in Figure IV-1 but will be discussed separately in reference to the K-edge spectra (see Figures IV-8 to IV-11). For the sake of consistency, throughout this report, wherever possible, peaks that arise from transitions to the same orbitals will be labeled with the same letter. In the case of L-edge spectra, the $p_{3/2}$ and $p_{1/2}$ components of the transition will be labeled with a letter and its *prime* (ie. peaks A and A'). Figure IV-2 shows the pre-edge region of the same five compounds shown in Figure IV-1 on an expanded scale from 101 to 111 eV, and the positions of the peaks from Figure IV-2 (peaks A to F)

Figure IV-1. The Si 2*p* and 2*s* XANES spectra of $Si(OCH_3)_x(CH_3)_{4-x}$ (x=0 to 4)

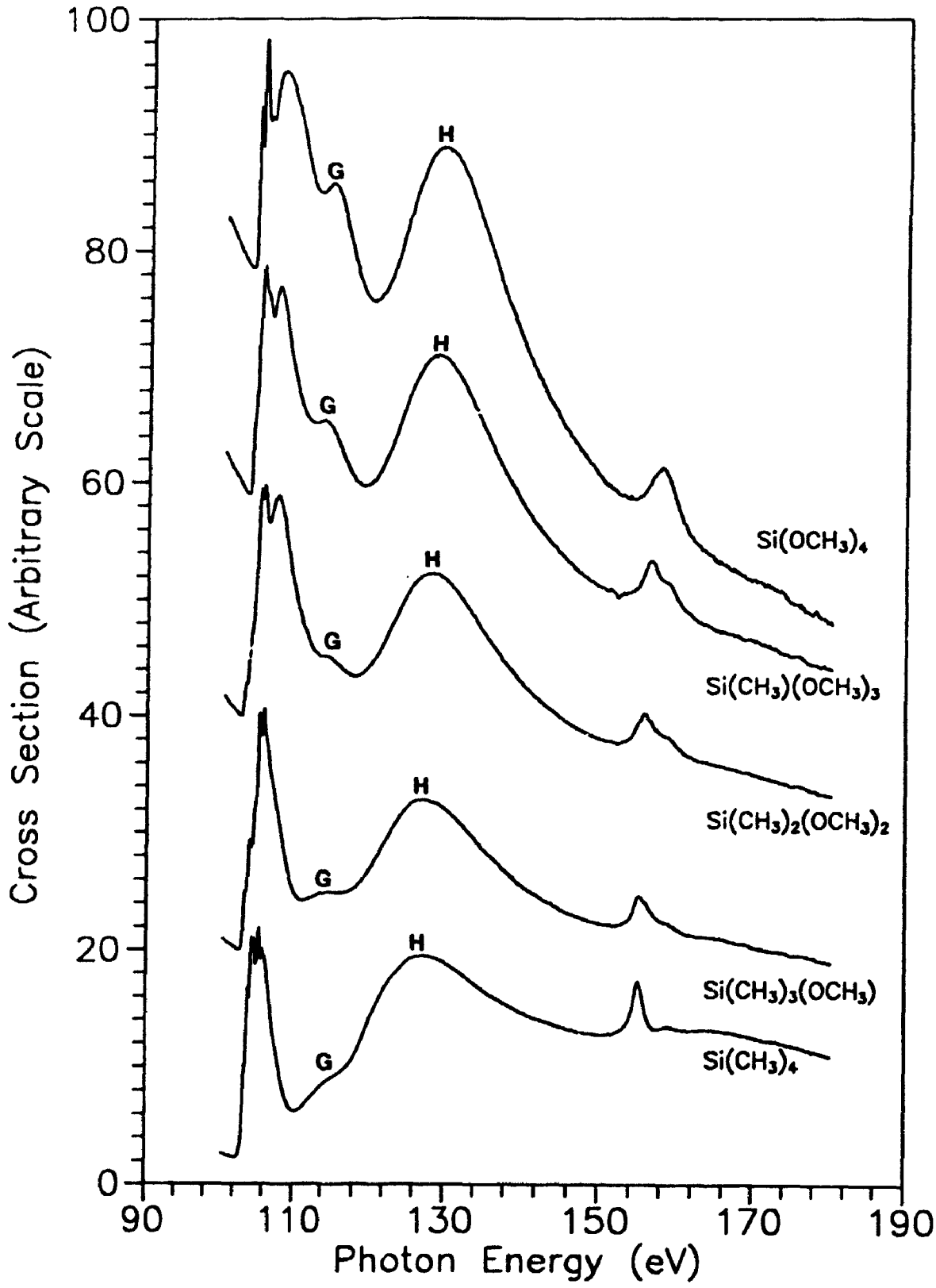
100
80
60
40
20
0
Cross Section (Arbitrary Scale)
90
110
130
150
170
190
Photon Energy (eV)
G
H
Si(OCH3)4
Si(CH3)(OCH3)3
Si(CH3)2(OCH3)2
Si(CH3)3(OCH3)
Si(CH3)4

Figure IV-2. The Si 2*p* XANES spectra of $Si(OCH_3)_x(CH_3)_{4-x}$ (x=0 to 4)

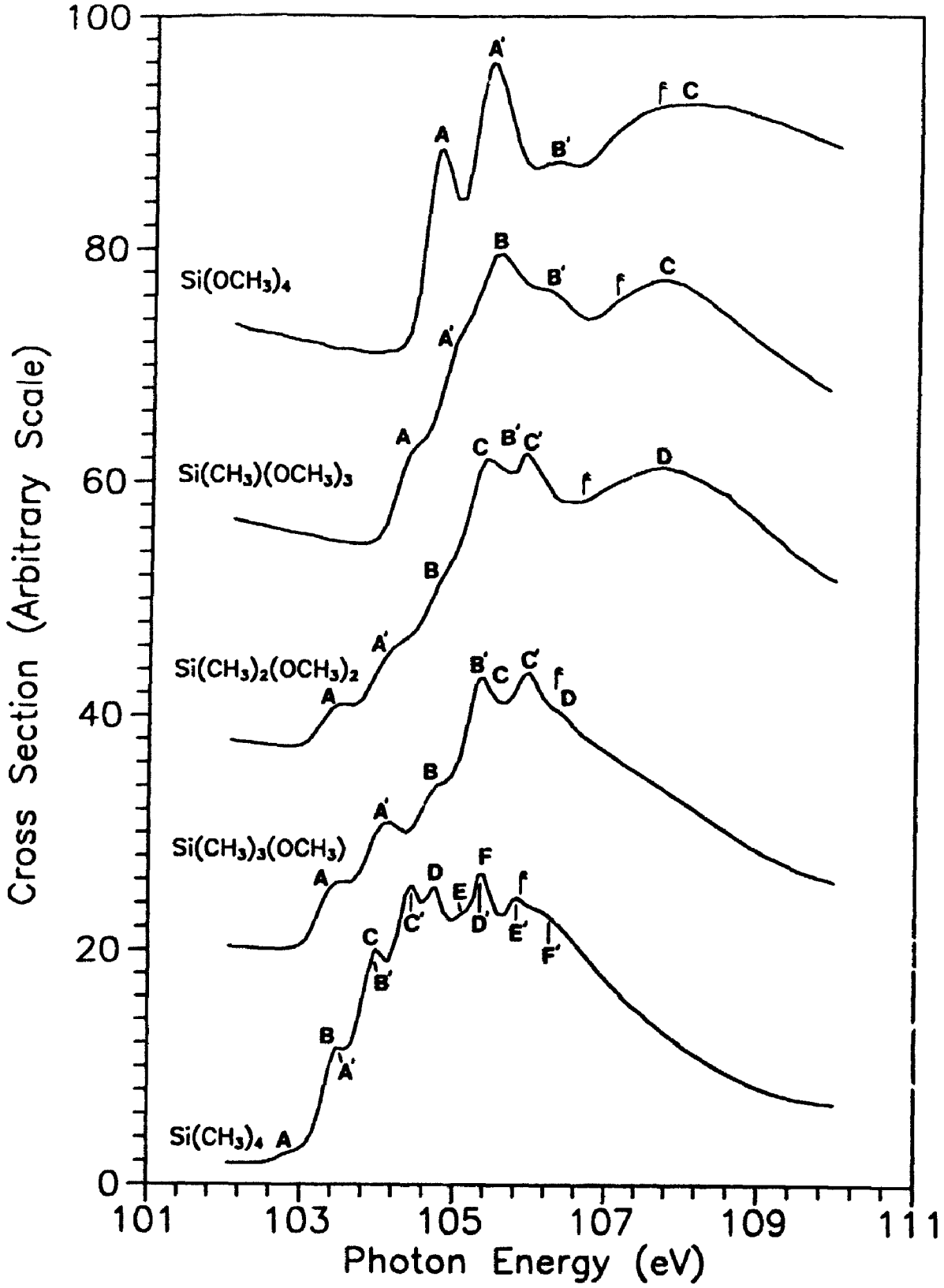
Cross Section (Arbitrary Scale)
Photon Energy (eV)
100
80
60
40
20
0
101
103
105
107
109
111
Si(OCH3)4
Si(CH3)(OCH3)3
Si(CH3)2(OCH3)2
Si(CH3)3(OCH3)
Si(CH3)4
A
A'
B
B'
C
C'
D
E
E'
F
F'
f
f'

and the peaks from Figure IV-1, (peaks G & H) are listed in Table IV-2. The position of the flag that marks the Si $2p_{3/2}$ adiabatic ionization potential is taken from reference 25.

Table IV-2: The peak positions (in eV ± 0.05 eV) of the spectra shown in Figures IV-1, IV-2 and IV-3A, and, the position of the Si $2p_{3/2}$ and $2p_{1/2}$ adiabatic binding energies from reference # 24.

	Molecule $Si(OCH_3)_X(CH_3)_{4-X}$ (Fig IV-1 & 2)					Figure IV-3A	
Peak	X=0	X=1	X=2	X=3	X=4	SiO_2	DOS (+ 95.9 eV)
A	102.82	103.52	103.52	104.47	104.76	105.57	105.9
A'	103.48	104.12	104.15	105.05	105.42	106.10	-
B	103.38	104.78	104.84	105.52	-	-	-
B'	103.98	105.34	105.52	106.13	106.27	-	-
C	104.00	105.39	105.40	107.69	108.10	108.04	107.9
C'	105.15	105.95	105.98	-	-	-	-
D	104.74	106.38	107.71	-	111.31	111.39	111.1
D'	105.37	-	-	-	-	-	-
E	105.15	-	-	-	-	-	-
E'	105.83	-	-	-	-	-	-
F	105.37	-	-	-	-	-	-
F'	106.26	-	-	-	-	-	-
G	114.65	114.55	114.02	114.19	114.82	114.51	118.1
H	126.85	127.10	128.18	128.70	129.36	130.53	-
Si $2P_{3/2}$	105.86	106.3(1)	106.6(1)	107.0(1)	107.42	103.8(1)*	-
Si $2P_{1/2}$	106.47	106.9(1)	107.2(1)	107.6(1)	108.03	104.4(1)*	-

* Si 2p ionization energies for SiO_2 were taken from reference 37

Immediately obvious is the increase in complexity of the spectra as you move through the series from TMOS ($Si(OCH_3)_4$) to TMS ($Si(CH_3)_4$). Nine peaks are observed in Figure IV-2 for the pre-edge region of TMS (some of which result from multiple transitions), in accord with previous work on this molecule[23], while only four peaks are observed for TMOS. The TMS peaks have been assigned to Si 2*p* to Rydberg transitions.[23] In contrast, the TMOS spectrum is more similar to that of SiF_4[23] in which the major peaks are due to Si 2*p* to antibonding transitions. In terms of Dehmer's *effective potential barrier model*[1] this decrease in complexity from TMS to TMOS is due to the creation of a potential barrier by the electronegative oxygen atoms allowing transitions only to an inner and outer potential-well and thereby obscuring the Rydberg fine structure in those compounds as the number of methoxy groups increases. By the time two methoxy groups have been replaced with methyl groups the pre-edge region (Figure IV-2) has become more like the spectrum of TMS while the post-edge region (Figures IV-1 & IV-2) has remained similar to that of TMOS.

Figure IV-3A shows the spectra of TMOS and SiO_2, and a density of states (DOS) calculation for SiO_2 (digitized from reference # 26) all plotted on the same axes while Figure IV-3B shows the spectrum of TMS and Filatova's spectrum of silicon carbide (digitized from reference # 7). The peak positions for the spectrum of SiO_2 and the DOS calculations in Figure IV-3A are detailed in the last two columns of Table IV-2. The spectra of SiO_2 and TMOS are remarkably similar; each has a sharp doublet centered at ~105.5 eV (peaks A and A' in Figure IV-3A) followed by a broader peak at ~107.5 eV (peak C). Peak D is a distinct feature in the solid state spectrum but shows up only as a shoulder on peak C in the gas-phase analog. This is followed by a broad, asymmetric peak at ~114 eV and a very broad

Figure IV-3. (A) The Si 2*p* gas-phase spectra $Si(OCH_3)_4$ (top), solid state SiO_2 (middle) and DOS calculation (bottom). (B) The Si 2*p* gas-phase spectra of $Si(CH_3)_4$ (top) and solid state SiC (bottom).

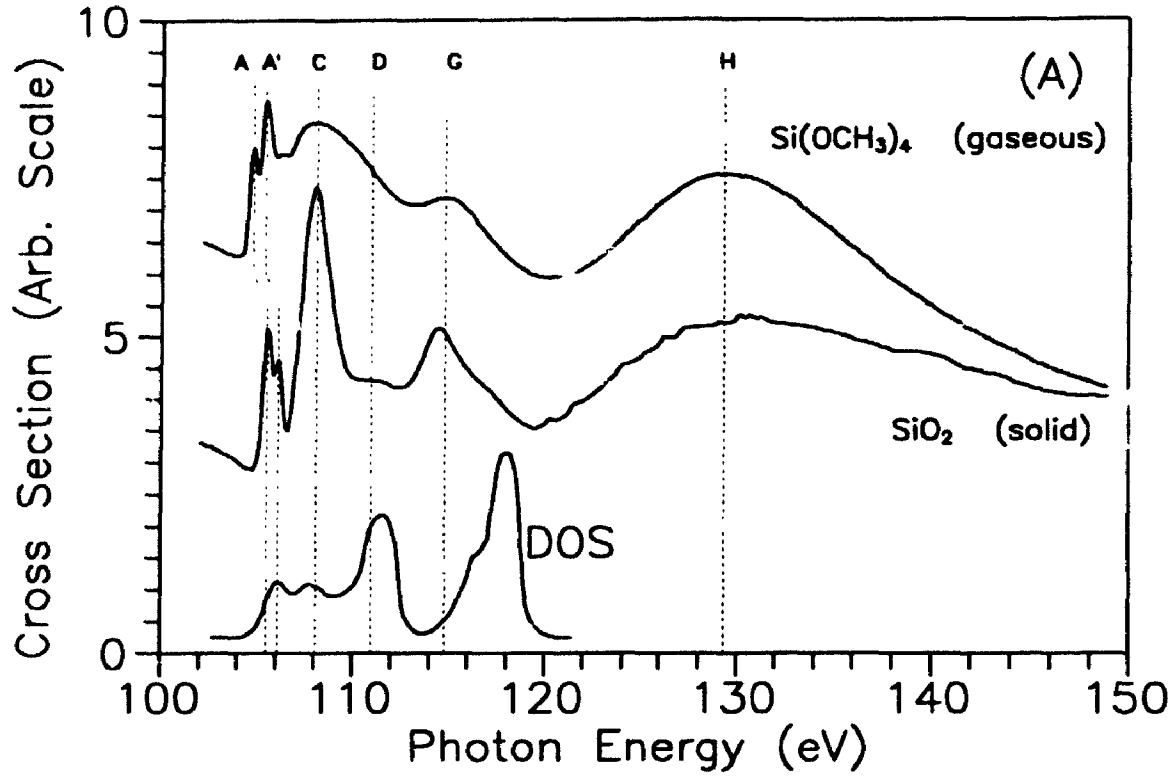
A
A'
C
D
G
H
(A)
Si(OCH3)4 (gaseous)
SiO2 (solid)
DOS
Cross Section (Arb. Scale)
10
5
0
100
110
120
130
140
150
Photon Energy (eV)

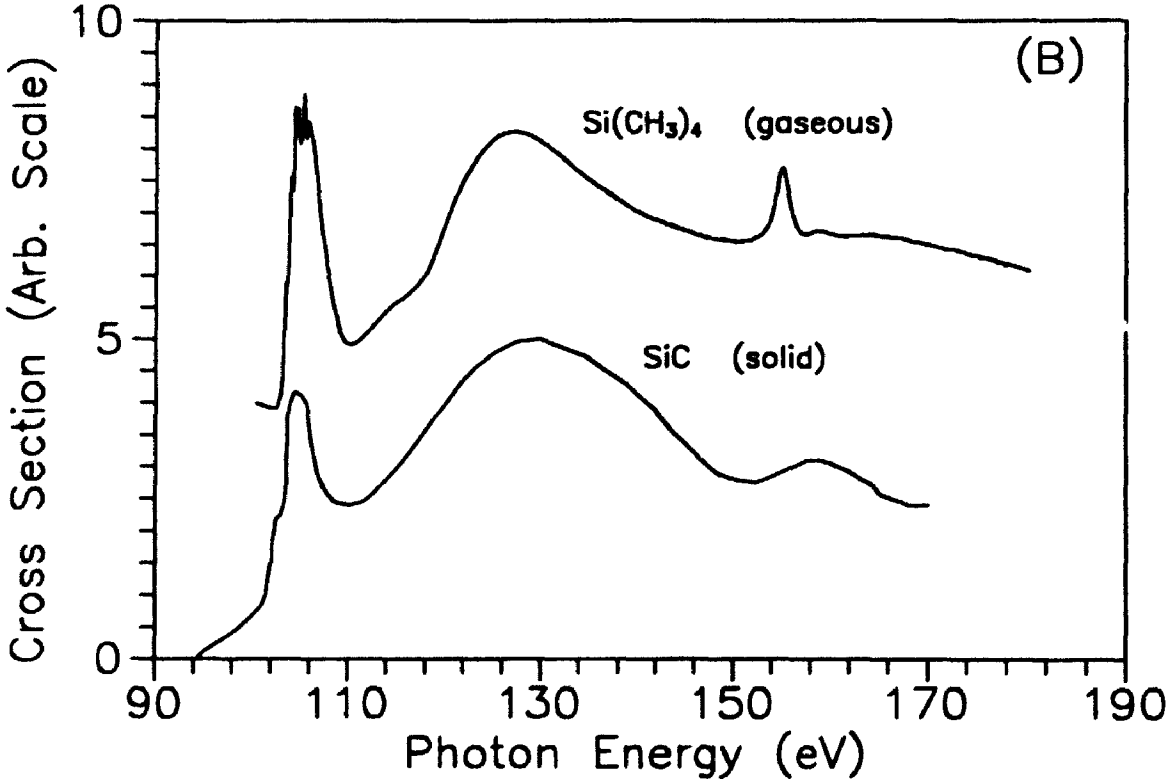
(B)
Si(CH3)4 (gaseous)
SiC (solid)
Cross Section (Arb. Scale)
10
5
0
90
110
130
150
170
190
Photon Energy (eV)

peak at ~130 eV (peaks G and H respectively). The initial doublet is shifted to higher energy in the spectrum of SiO_2; but, all other peaks occur at almost exactly the same position and have similar intensity.

The conduction band in the DOS calculation has been shifted by 95.9 eV to align it with the L-edge XANES spectrum of SiO_2. It is interesting to note that although the DOS calculation shows only the relative position of the unoccupied states (and not the *s* or *p* character of these states or the transition probabilities to these states) the overall shape of the DOS plot is quite similar to that of the Si 2*p* spectrum of SiO_2. Peaks A, C and D have similar relative positions in the DOS calculation and the SiO_2 spectrum. The difference in relative intensity could well be due to the different *s* and *p* character of the conduction band data. Obviously peak G is not well reproduced by the DOS calculations. Unfortunately, the original authors[26] did not assign or even discuss the *s* and *p* character of the conduction band and as such, no direct comparison can be made with the current calculations (see Figures IV-4 and IV-5). A more detailed comparison of the DOS calculation[26] and the SiO_2 spectrum will be dealt with in a future publication.[27] In Figure IV-3B the fine structure in the pre-edge region of the SiC spectrum is washed out compared to the spectrum of TMS but the spectra are otherwise qualitatively similar. Better quality spectra of SiC are required for a more detailed comparison.

Despite the similar general appearance, there are however some differences between the spectrum of the solid state SiO_2 and the gas-phase TMOS: the relative intensities of the initial doublet are reversed in the gas and solid state, and the small peak labeled B' in the spectrum of TMOS (Figure IV-2) is not present in the spectrum of SiO_2. Both of these differences can be rationalized by analysis of the MS-Xα simulation which is

discussed below. Peak C, centered at ~107 eV, is much sharper in the solid state spectrum than it is in the gas-phase and this may be the result of splitting of the energy levels due to the lower symmetry of TMOS compared with the tetrahedral symmetry of SiO_2. Also, there is a small feature in the spectrum of SiO_2 at ~111 eV (peak D, Figure IV-3A) that is washed out by peak C in the spectrum of TMOS and, peak G has a slight shoulder on the high energy side in the solid state that is not present in the gas-phase. The above discrepancies not withstanding, spectra of this similarity can only arise from almost identical electronic transitions in the two compounds and this is strong evidence that the Si 2*p* XANES features are dependent almost entirely upon the local environment of the central Si atom, with extended long range structure playing only a minor role. A similar conclusion has been reached[28] for the Si $L_{2,3}$ edge in the ELNES spectra of the nesosilicates Mg_2SiO_2, Fe_2SiO_4, Be_2SiO_4, Zn_2SiO_4.

Figures IV-4 and IV-5 show the pre-edge and continuum region of TMOS and TMS, respectively, together with their respective MS-Xα simulations. The simulation of TMS was carried out in T_d symmetry while that of TMOS was done in C_{2v} because the true S_4 symmetry of TMOS is not amenable to the MS-Xα technique. The present results for the Si 2*p* edge of TMS agree quantitatively with those of Bozek[23] and the assignments and oscillator strengths for TMOS and TMS are presented in Table IV-3.

The simulated pre-edge spectra in Figure IV-4 were calculated using the positions of the unoccupied molecular orbitals and their corresponding oscillator strengths. Each peak was coupled to its spin-orbit counter-part with a splitting of 0.613 eV and an intensity ratio of 2:1. Each transition was represented by a peak with a half-height width of 0.5 eV for TMOS and 0.4 eV for TMS and a 100% Lorentzian lineshape. In both cases the simulated

Figure IV-4. (A) The Si 2*p* pre-edge XANES spectra of $Si(OCH_3)_4$ (top) and the corresponding MS-Xα SCF simulation (bottom).
(B) The Si 2*p* pre-edge XANES spectra of $Si(CH_3)_4$ (top) and the corresponding MS-Xα SCF simulation (bottom). Dashed lines in both (A) and (B) mark the positions of the individual transitions.

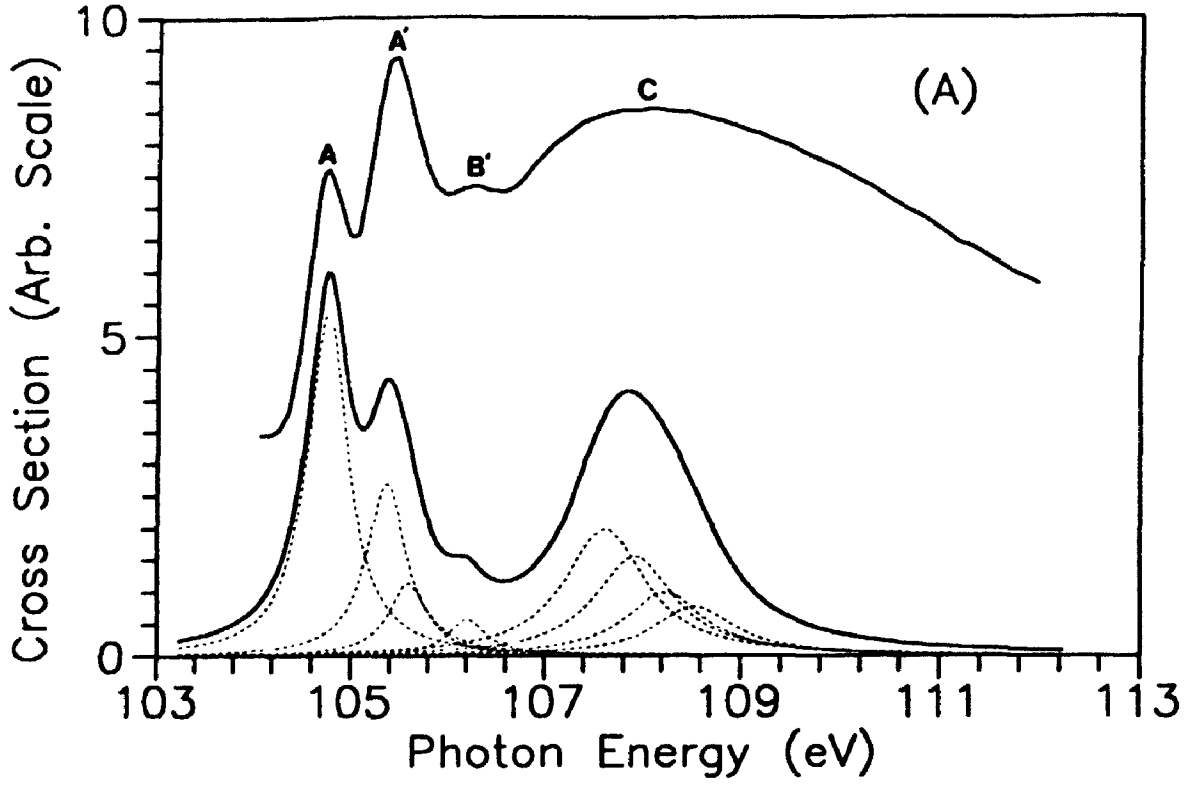
10
5
0
Cross Section (Arb. Scale)
A
A'
B'
C
(A)
103
105
107
109
111
113
Photon Energy (eV)

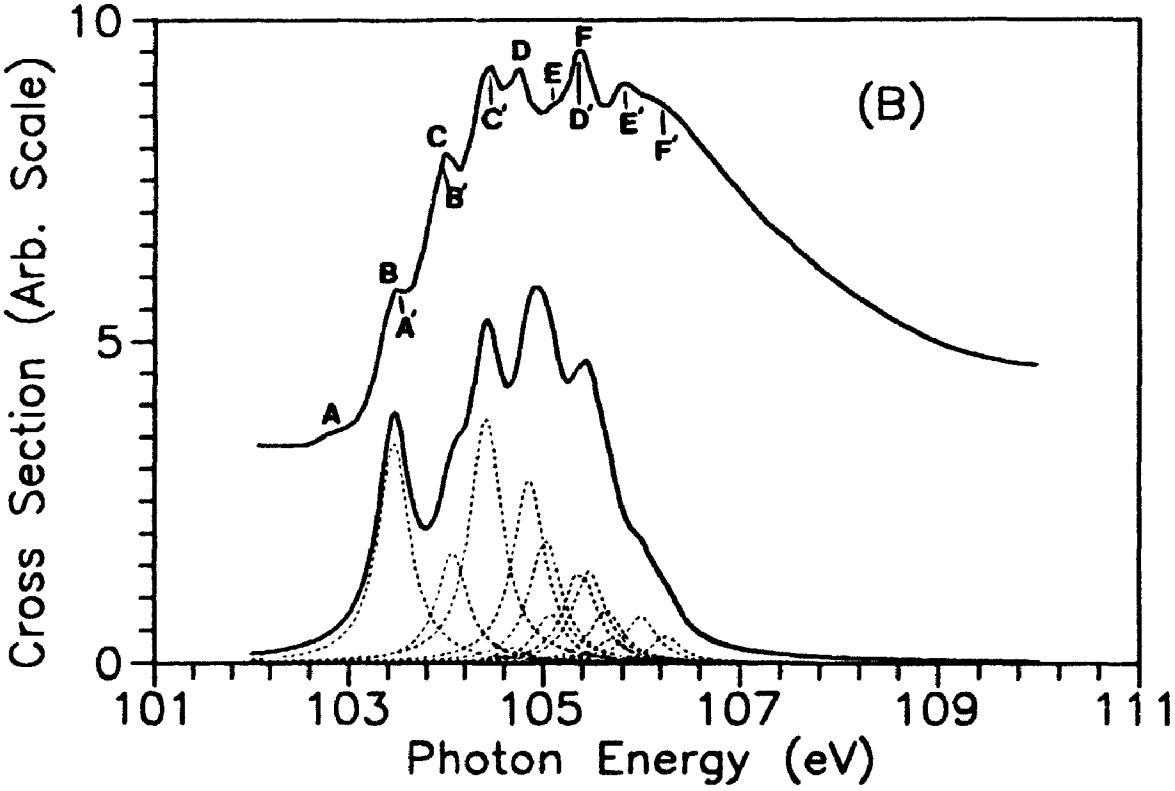
10
5
0
Cross Section (Arb. Scale)
A
B
A'
C
B'
C'
D
E
F
D'
E'
F'
(B)
101
103
105
107
109
111
Photon Energy (eV)

Figure IV-5. (A) The Si 2*p* continuum spectra of $Si(OCH_3)_4$ (top) and the corresponding MS-Xα SCF simulation (bottom). (B) The Si 2*p* continuum spectra of $Si(CH_3)_4$ (top) and the corresponding MS-Xα SCF simulation (bottom).

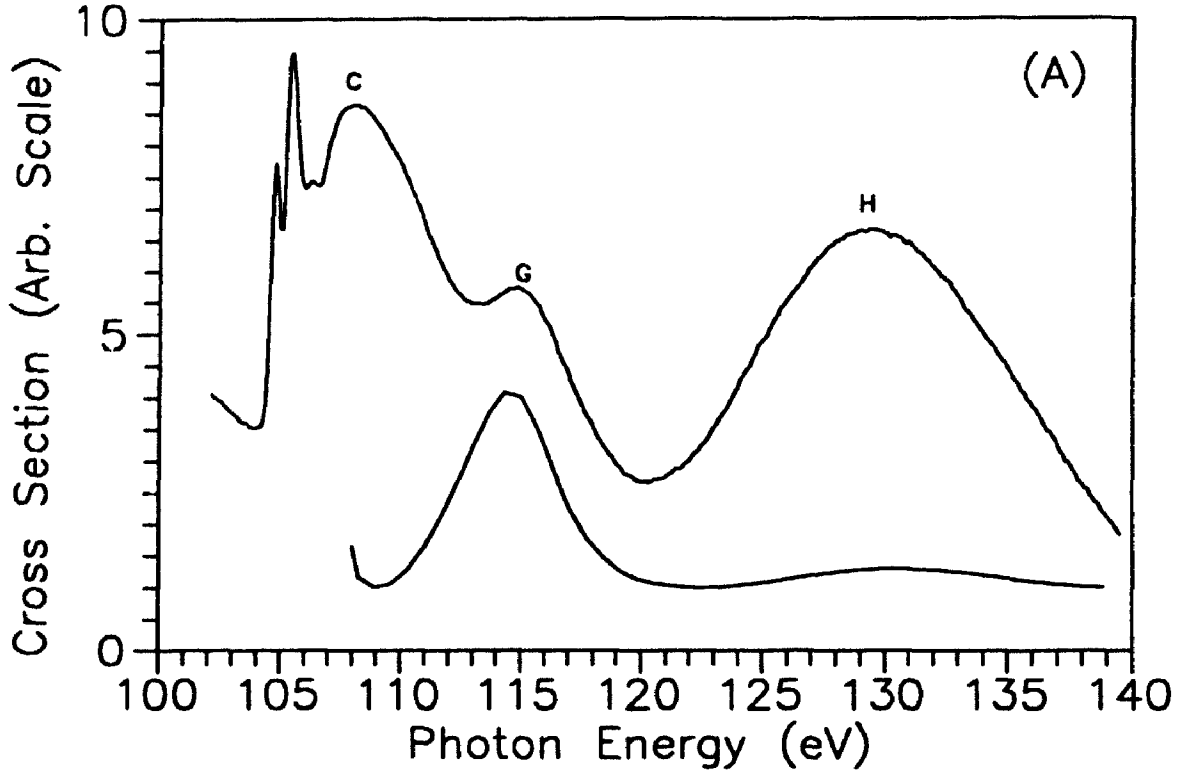
(A)
C
G
H
Cross Section (Arb. Scale)
10
5
0
100 105 110 115 120 125 130 135 140
Photon Energy (eV)

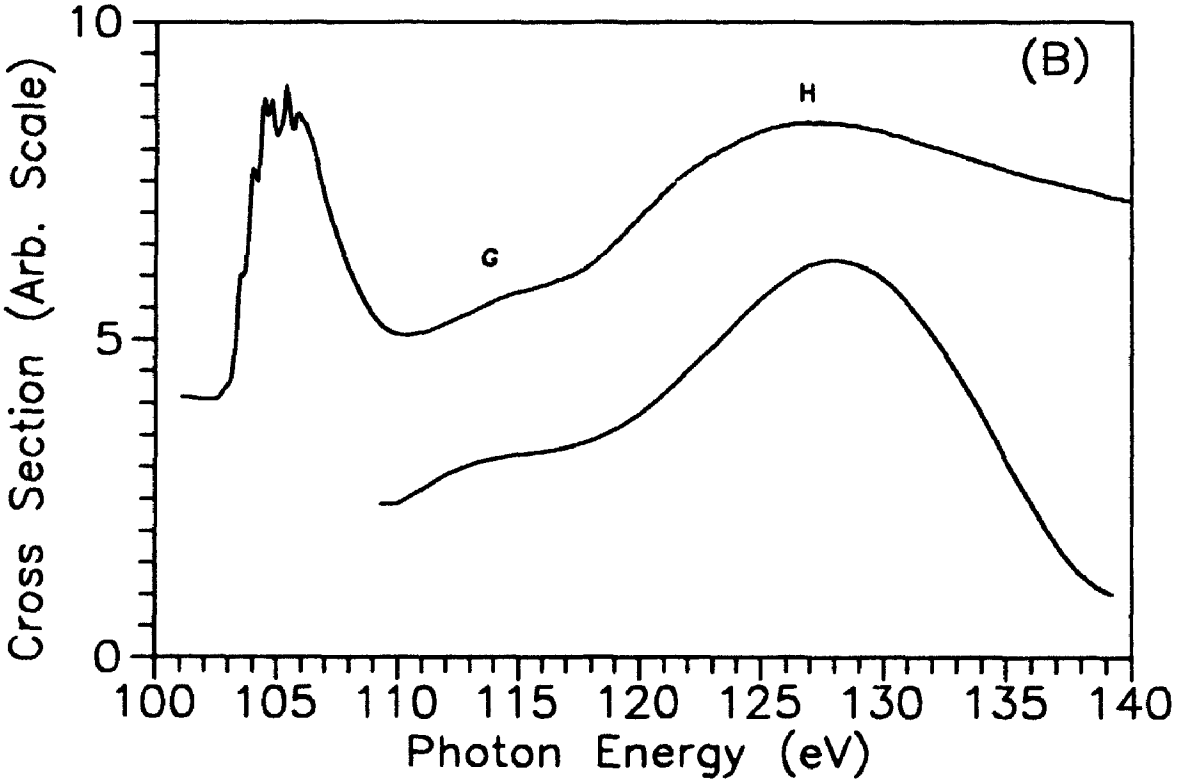
(B)
H
G
Cross Section (Arb. Scale)
10
5
0
100 105 110 115 120 125 130 135 140
Photon Energy (eV)

spectra had to be shifted by ~0.7 eV to align them with the experimental data.

Table IV-3: The calculated orbitals, transition energies, term values and oscillator strengths for the Si 2*p* edge of $Si(OCH_3)_4$ and $Si(CH_3)_4$. The Corresponding experimental peak is shown in parenthesis after the energy.

Orbital	Calc. Energy (exp peak) $P_{3/2}$ (eV)	$P_{1/2}$ (eV)	Term Value (eV)	Oscillator Strength	Remark
$Si(OCH_3)_4$					
a_1^*	104.84(A)	105.45(A')	2.58	1.26×10^{-3}	Antibonding
a_1	105.68(B)	106.29(B')	1.74	2.67×10^{-4}	Mixed Ryd.
a_1^*	107.70(C)	108.31(C)	-0.28	9.24×10^{-4}	Antibonding
b_1^*	108.00(C)	108.61(C)	-0.58	3.61×10^{-4}	Antibonding
b_2^*	108.00(C)	108.61(C)	-0.58	3.61×10^{-4}	Antibonding
$Si(CH_3)_4$					
$4t_2^*$	103.67(B)	104.28(B')	2.19	1.55×10^{-3}	Rydberg *p*
$5t_2^*$	104.63(C)	105.24(C')	1.23	1.75×10^{-3}	Rydberg *p*
$2e^*$	104.90(D)	105.51(D')	0.96	1.11×10^{-4}	Rydberg *d*
$6t_2^*$	105.07(E)	105.68(E')	0.79	1.31×10^{-3}	Rydberg *d*
$7t_2^*$	105.29(F)	105.90(F')	0.57	3.45×10^{-4}	Rydberg *p*
$9t_2^*$	105.59(F,)	106.20(F')	0.27	6.82×10^{-4}	Rydberg *d*
$10t_2^*$	105.70	106.31	0.16	8.43×10^{-5}	Rydberg *p*
$13t_2^*$	105.85	106.46	0.01	3.87×10^{-4}	Rydberg *d*

The spectrum of TMS has already been described by Bozek *et al.*[23] and thus will not be discussed here in detail. The peaks in this spectrum result from transitions to Rydberg-type orbitals mostly of atomic *p*- and *d*-character.

The agreement between experiment and theory in TMOS is very good with all of the features in the experimental spectrum being represented in the simulation with the relative peak positions agreeing to within 0.2 eV. In C_{2v} symmetry the *p* orbitals have a_1, b_1 and b_2 symmetry for the p_z, p_x and p_y orbitals respectively. Wherever transitions from more than one *p*-orbital occur at the same position (ie. p_x+p_y, $p_x+p_y+p_z$, etc.), only the sum of the transitions is shown; that is, no distinction is made between a transition from a p_x, p_y or p_z orbital.

The initial doublet, peaks A and A' in the simulation, results from a transition to an antibonding orbital of a_1^* symmetry which is split into a $p_{3/2}$ (peak A) and a $p_{1/2}$ (peak A') component. The reversal of the relative intensities of the spin orbit doublet in experimental spectra is not uncommon in photoabsorption spectroscopy[23,24] and this phenomenon has been discussed by Schwarz.[29,30] It is important to note here that the relative intensities in the simulation agree very well with the solid state spectrum of SiO_2 in Figure IV-3A.

Peak B', at 106.29 eV, is the $p_{1/2}$ component of a transition to a mixed Rydberg orbital of a_1 symmetry. If this peak in the simulation was given sufficient intensity to match its corresponding position in the experimental data, and its $p_{3/2}$ component (which is directly under peak A') was increased accordingly, then this would boost the intensity of peak A' in the simulation by a sufficient amount so as to match that of the experimental data. As noted in the discussion of the solid state spectrum,

the fact that peak B' does not appear at all in the spectrum of SiO_2, and the fact that the intensities of the initial doublet are reversed between the gas and solid state suggests that the transition which is responsible for peak B' in TMOS is not present in SiO_2. This issue is addressed below.

The broad band at ~108 eV (peak C) results from three transitions to three unoccupied orbitals of a_1^*, b_1^* and b_2^* symmetry, all three of which are just above the ionization threshold. The b_1^* and b_2^* orbitals are isoenergetic and thus show up as only a single spin-orbit doublet, the other doublet arising from the transition to the a_1^* orbital. (In Td symmetry these three orbitals combine to form the t_2^* antibonding orbital as will be discussed in reference to Figure IV-6 below). The broad nature of this peak in the experimental data suggests that there may be several other transitions here, such as Rydberg states, that are not accounted for in the simulation. This may be a manifestation of the fact that the simulation was carried out in C_{2v} symmetry while the true symmetry of the molecule is actually S_4.

The continuum region shown in Figure IV-5 is represented reasonably well by the calculations for TMOS and very well for TMS. Peaks G in both spectra result from a *d*-shape resonance[31] of *e*-symmetry and is simulated very well by the Xα calculation. The second peak, H, (at ~130 eV) which should be very intense shows up only as a very weak peak in the simulation of TMOS. This peak is present in virtually every Si 2*p* photoabsorption spectrum of all Si-containing compounds. It's position at ~130 eV is coincident with the maximum of the Si 2*p* cross section and this, coupled with its ubiquitous presence in all Si 2*p* spectra strongly suggests that it is the result of an atomic effect that is largely independent of the ligands to which the Si is attached. The fact that this is likely an atomic effect

and thus independent of the orbital structure of TMOS may account for the poor correspondence between theory and experiment in this region of the Si 2*p* spectrum of TMOS. Peak D has also been assigned (in the Si L-edge spectra of other Si compounds[31]) to the t_2 component of a *d*-shape resonance. Although not a perfect match, the Xα simulation of TMOS is a better theoretical model for the Si 2*p* spectrum of SiO_2 than the DOS calculation[26] (see Figure IV-3A) and has the distinct advantage of being more economical in terms of both time and cost. Only minor peaks - peak B' in TMOS (Figure IV-2) and D in SiO_2 (Figure IV-3A) - are not common to both spectra.

Derived from the MS-Xα calculations, Figure IV-6 shows a molecular orbital (MO) diagram for TMOS in C_{2v} symmetry and the corresponding orbitals in tetrahedral symmetry. For the sake of simplicity, the only orbitals shown are the occupied orbitals that constitute Si-O bonds, and, the first four unoccupied orbitals; namely, the first two a_1^* orbitals, the first b_1^* and the first b_2^* orbital. The orbitals in T_d symmetry were composed from those in C_{2v} from a standard group theory correlation table. To the left of each orbital in T_d symmetry is the combination of irreducible representations in C_{2v} from which it is composed and to the right is the T_d irreducible representation to which it belongs. The ordering of the orbitals in T_d is identical to that of similar MO diagrams[10,11] calculated for SiO_4^{4-} except that the ordering of the first two unoccupied states in the present calculation is reversed compared to that of Tossell *et al.*[10] This reversal is consistent with more recent calculations by McComb *et al.*[32] The positions of the occupied states in this calculation and those of Tossell[10] are compared in Table IV-4 along with the positions of peaks in the valence band photoelectron spectra of TMOS and SiO_2. The absolute values of the molecular orbital energies calculated for TMOS and SiO_4^{4-} are quite different

Figure IV-6. Molecular orbital diagram for $Si(OCH_3)_4$ in C_{2v} and T_d symmetries. To the left of the orbitals in T_d symmetry is the combination of C_{2v} irreducible representations from which they are comprised and to the right is the T_d representation to which they belong.

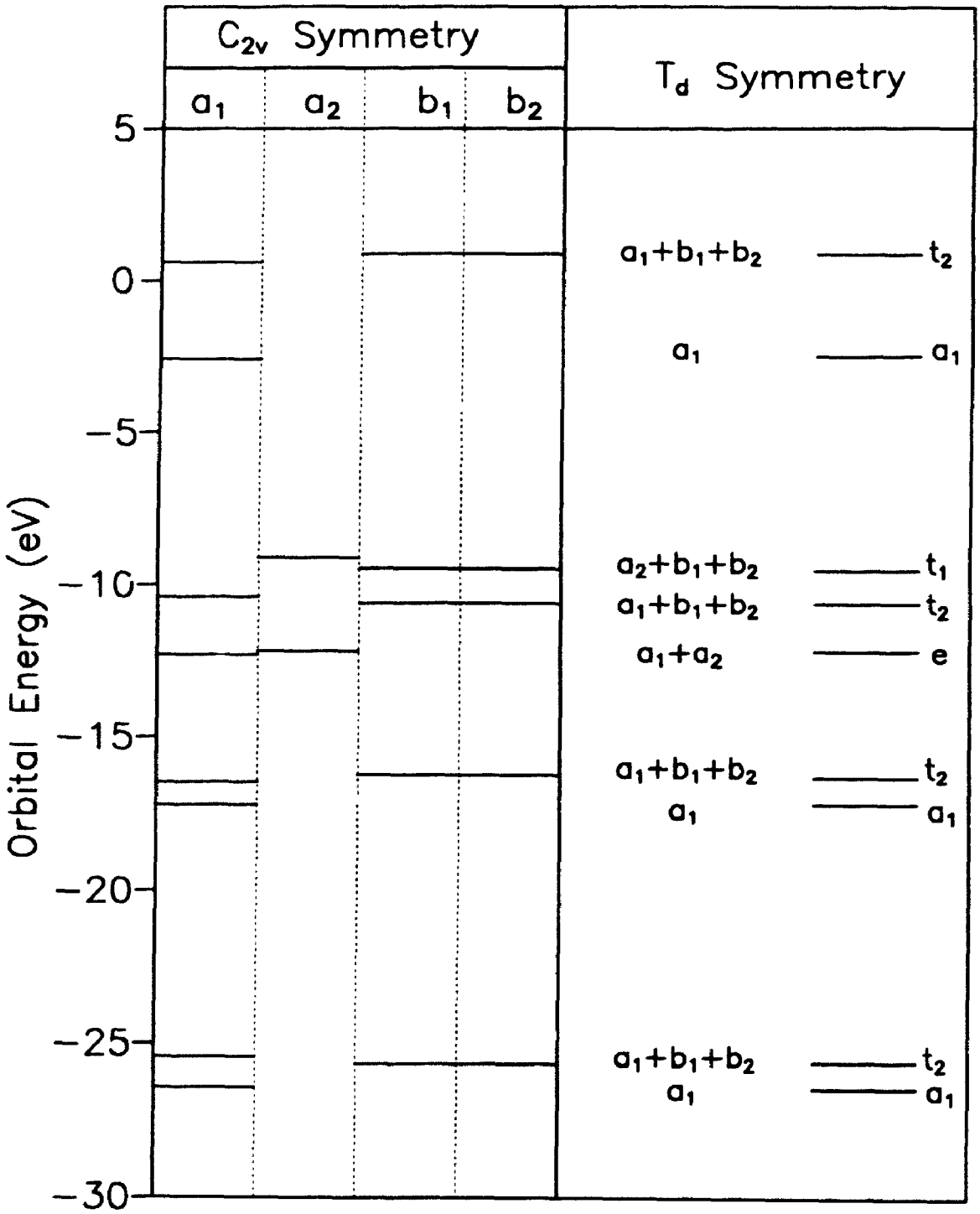
C2v Symmetry
a1
a2
b1
b2
Td Symmetry
Orbital Energy (eV)
5
0
−5
−10
−15
−20
−25
−30
a1+b1+b2
t2
a1
a1
a2+b1+b2
t1
a1+b1+b2
t2
a1+a2
e
a1+b1+b2
t2
a1
a1
a1+b1+b2
t2
a1
a1

mainly because of the large negative charge on the latter species, but the ordering is the same and the relative differences between states are very close in the two analogs.

Table IV-4: The positions of the Si-O bonding orbitals from the photoelectron spectra of $Si(OCH_3)_4$ and SiO_2 (Figure IV-7), the calculated positions of the MO's of $Si(OCH_3)_4$ (Figure IV-6) and the calculated MO's for SiO_4 (reference # 10). Both experimental and calculated values for SiO_2 have been shifted by 7 eV for comparison with the gas-phase data. The positions of the C-O and C-H bonding orbitals in $Si(OCH_3)_4$ (Figure IV-7) are also listed.

Peak Assignment	$Si(OCH_3)_4$ (eV)	SiO_2 (+ 7 eV)	SCF Calc. (eV)	SCF Calc[10] (- 7 eV)
t_1	8.95	8.05	-9.48	-7.0
t_2	9.71	9.37	-10.60	-8.0
e	10.71	10.97	-12.17	-8.5
C-O	13.22	-	-	-
t_2	13.99	13.63	-16.22	-12.4
C-H	13.99	-	-	-
a_1	16.71	16.80	-17.5	-15.5

From Table IV-3 and the MO diagram in Figure IV-6 it can be seen that the first three peaks in the Si 2*p* spectrum of TMOS (Peaks A, A' and B' in Figure IV-2) result from transitions to two orbitals of a_1 symmetry; the first being antibonding and the second being mixed Rydberg in character.

The second of these orbitals (the mixed Rydberg orbital) has been omitted from the MO diagram in Figure IV-6 because transitions to Rydberg-type orbitals are usually washed out in solid state spectra. The next three orbitals in TMOS are an a_1^*, a b_1^* and a b_2^*. These three orbitals are approximately isoenergetic and combine to form the t_2^* in tetrahedral symmetry. With this in mind it is reasonable to suggest that the initial doublet in the spectrum of SiO_2 results from a transition to a molecular orbital of a_1^* symmetry and that peak C in the spectrum of SiO_2 results from a transition to the t_2^* orbital. This type of assignment, based upon a molecular orbital interpretation of SiO_2, is very similar to that proposed by Filatova[7] *et al.*

Figure IV-7 shows a comparison of the photoelectron spectra of TMOS and SiO_2. The data for the valence band photoelectron spectrum of SiO_2 has been digitized from DiStefano and Eastman[2], deconvoluted with a series of 100% Gaussian peaks and shifted by 7 eV to better align it with the gas-phase spectrum. This spectrum has been interpreted by Tossell[10] in a fashion similar to that used for SiF_4 with the three lowest energy bands assigned to non-bonding orbitals of t_1, t_2 and e symmetry. Although this assignment is correct for SiF_4 or SiO_4^{4-}, it is not strictly correct for either SiO_2 or $Si(OCH_3)_4$. In the latter two cases each oxygen atom forms two bonds - to a second Si in SiO_2 or to a C in $Si(OCH_3)_4$ - and thus there are not enough non-bonding electrons on the four oxygen atoms to fill the three non-bonding orbitals. Despite this problem in SiO_2 and $Si(OCH_3)_4$, the Tossell-type assignment is in excellent qualitative agreement with band structure calculations[33,34] on SiO_2 and hence Tossell's MO assignment has been repeated here for the sake of comparison.

Although qualitatively very similar, the two spectra of TMOS and SiO_2

Figure IV-7. (A) The gas-phase valence band photoelectron spectra of $Si(OCH_3)_4$ and (B), the valence band of solid state SiO_2. Figure IV-7B is digitized from reference 2 and the energies have been shifted by 7 eV to better align it with the gas-phase data.

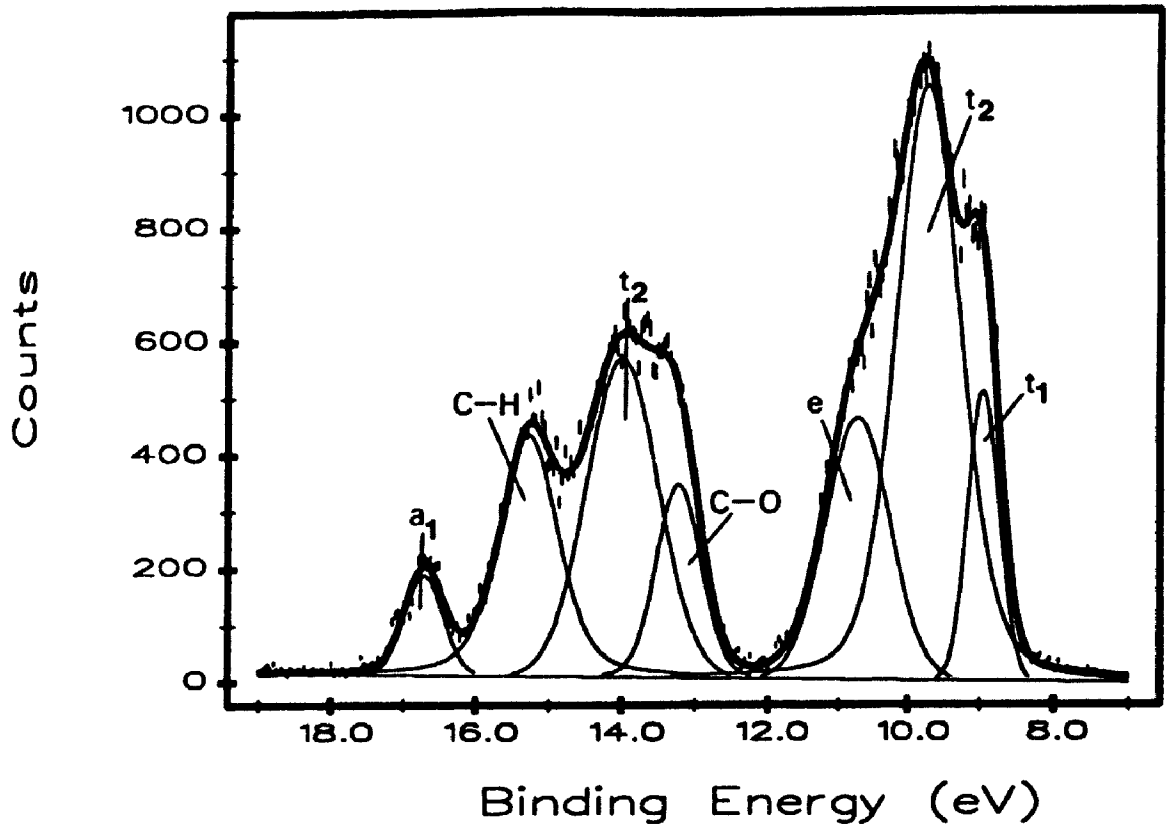
Counts
1000
800
600
400
200
0
C–H
t_2
C–O
a_1
e
t_2
t_1
18.0
16.0
14.0
12.0
10.0
8.0
Binding Energy (eV)

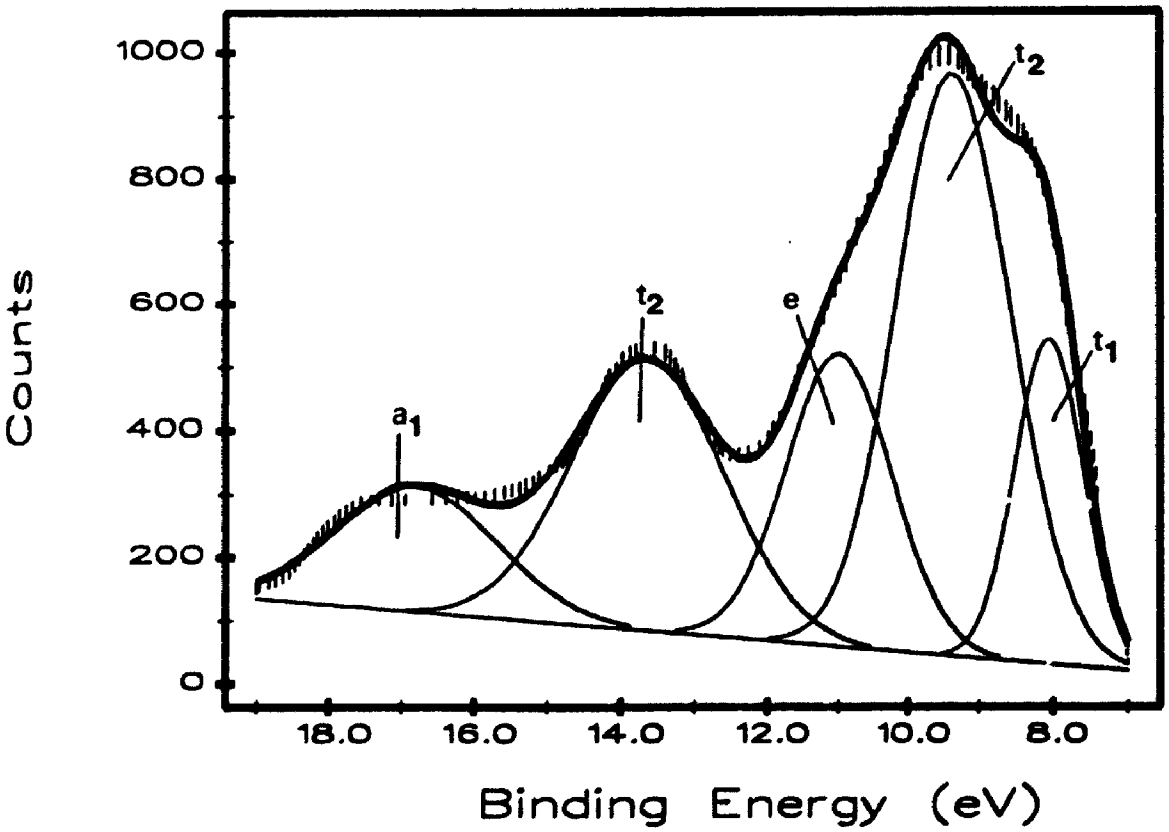
Counts
1000
800
600
400
200
0
a_1
t_2
e
t_2
t_1
18.0
16.0
14.0
12.0
10.0
8.0
Binding Energy (eV)

show that the occupied states in SiO_2 are separated from each other slightly more than they are in TMOS but it is impossible to say whether or not this trend also applies to the unoccupied antibonding orbitals. The largest peak, at ~10 eV in both Figures IV-7A and IV-7B, corresponds to ionizations of the three non-bonding orbitals of t_1, t_2 and e symmetry in Figure IV-6. The second largest peak in both spectra is centered at ~14 eV. In SiO_2 this corresponds to the Si-O bonding orbital of t_2 symmetry while in TMOS there are three components: (1) the O-C bonding orbital at 13.22 eV, (2) the Si-O bonding orbital at 13.99 eV (t_2 in Figure IV-6) and (3) the C-H bonding orbitals at ~15.27 eV. The final peak at ~17 eV corresponds to the Si-O bonding orbitals of a_1 symmetry in SiO_2 and TMOS. The excellent agreement between the valence band photoelectron spectra of TMOS and SiO_2 is further testimony to the similarity of the electronic structure in these two systems.

Section IV-4; The Si 1s and 2s Edges

Figure IV-8 shows the Si 1s photoabsorption spectra of the five compounds in the series $Si(CH_3)_X(OCH_3)_{4-X}$ from 1830 to 1880 eV and Table IV-5 gives the positions of the peaks. The spectrum of TMOS and TMS have been reported before and although the current work agrees well with previously reported spectra of TMS,[15,16] the previously reported spectrum of TMOS[16] shows only a single broad peak where Figure IV-8 shows beyond any doubt that this actually consists of at least two peaks. This fact is further supported by inspection of the spectra of the intermediate compounds in which this second peak is seen to increase in stoichiometric proportion to the number of methoxy groups in the molecule. The spectra of TMOS and TMS are qualitatively similar to those of SiF_4 and $SiCl_4$ in which the spectra consist of one (or two in the case of SiF_4) sharp transitions followed by two or three relatively weak peaks at higher energy.[15]

Figure IV-9A shows the spectra of the 1s regions in TMOS and SiO_2 and the DOS calculation (shifted by 1835 eV) all plotted on the same axes and Figure IV-9B shows the comparison of the Si 1s spectrum of TMS and silicon carbide (digitized from reference 35). The main peak in the spectrum of SiC is extremely broad and likely consists of several different transitions while the corresponding peak in SiO_2 is very narrow - narrower even then the corresponding peak in TMS! Furthermore, the spectrum of SiO_2 shows only a single sharp peak whereas the gas-phase analog, TMOS, has an obvious doublet structure. The absence of this doublet in the solid state spectrum is discussed below in the analysis of the MS-Xα simulation.

Figure IV-8. The Si 1*s* XANES spectra of of the five compounds in the series $Si(CH_3)_x(OCH_3)_{4-x}$ (X=0 to 4).

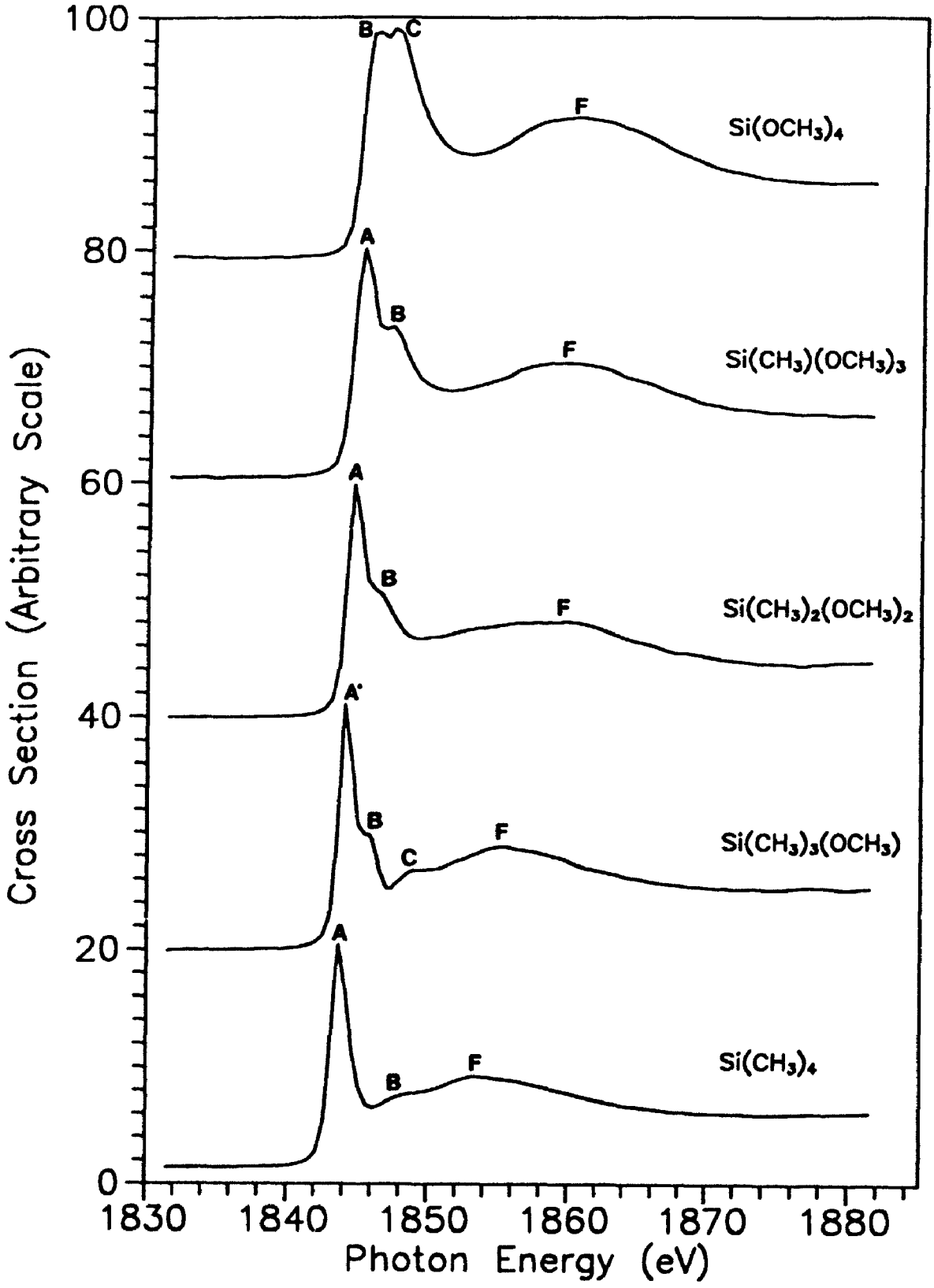
100
80
60
40
20
0
Cross Section (Arbitrary Scale)
1830
1840
1850
1860
1870
1880
Photon Energy (eV)
B
C
F
Si(OCH3)4
A
B
F
Si(CH3)(OCH3)3
A
B
F
Si(CH3)2(OCH3)2
A'
B
C
F
Si(CH3)3(OCH3)
A
B
F
Si(CH3)4

Figure IV-9. (A) Comparison of the Si 1*s* XANES spectra of gas-phase $Si(OCH_3)_4$ and solid state SiO_2. (B) Comparison of the Si 1*s* XANES spectra of gas-phase $Si(CH_3)_4$ and solid state SiC.

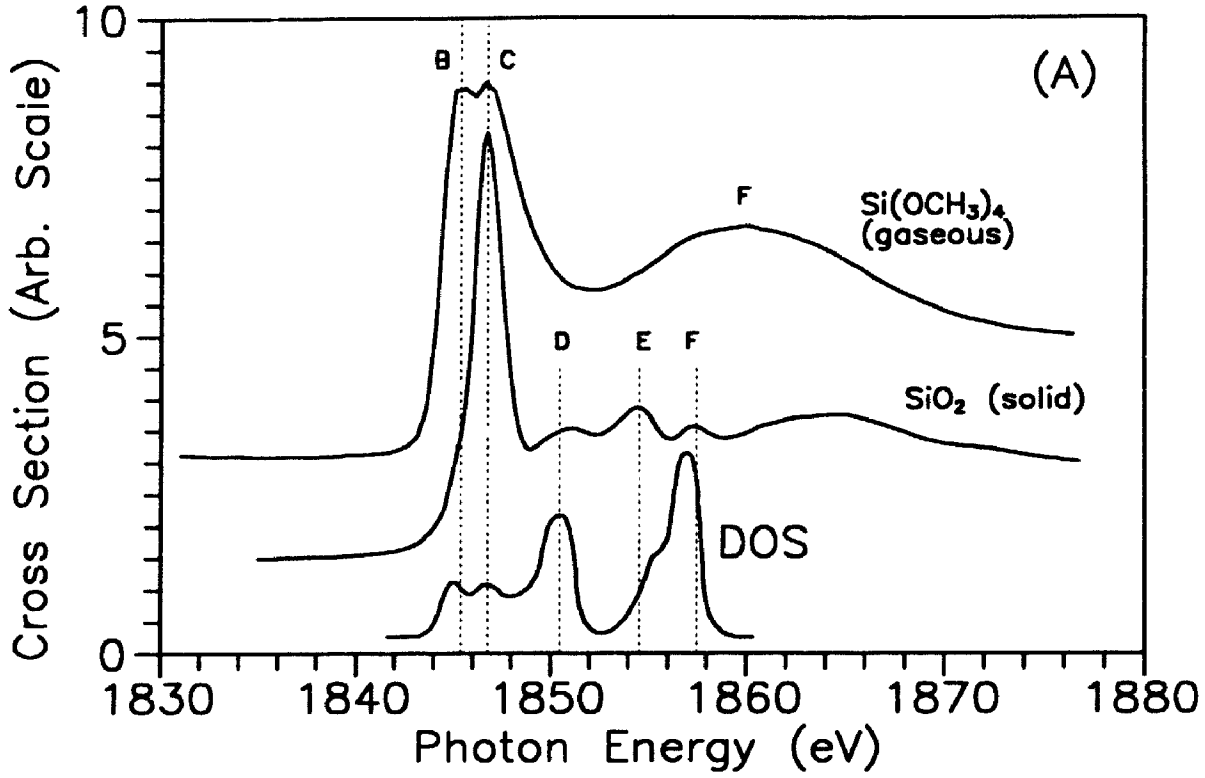
10
5
0
Cross Section (Arb. Scale)
B
C
(A)
F
Si(OCH3)4
(gaseous)
D
E
F
SiO2 (solid)
DOS
1830
1840
1850
1860
1870
1880
Photon Energy (eV)

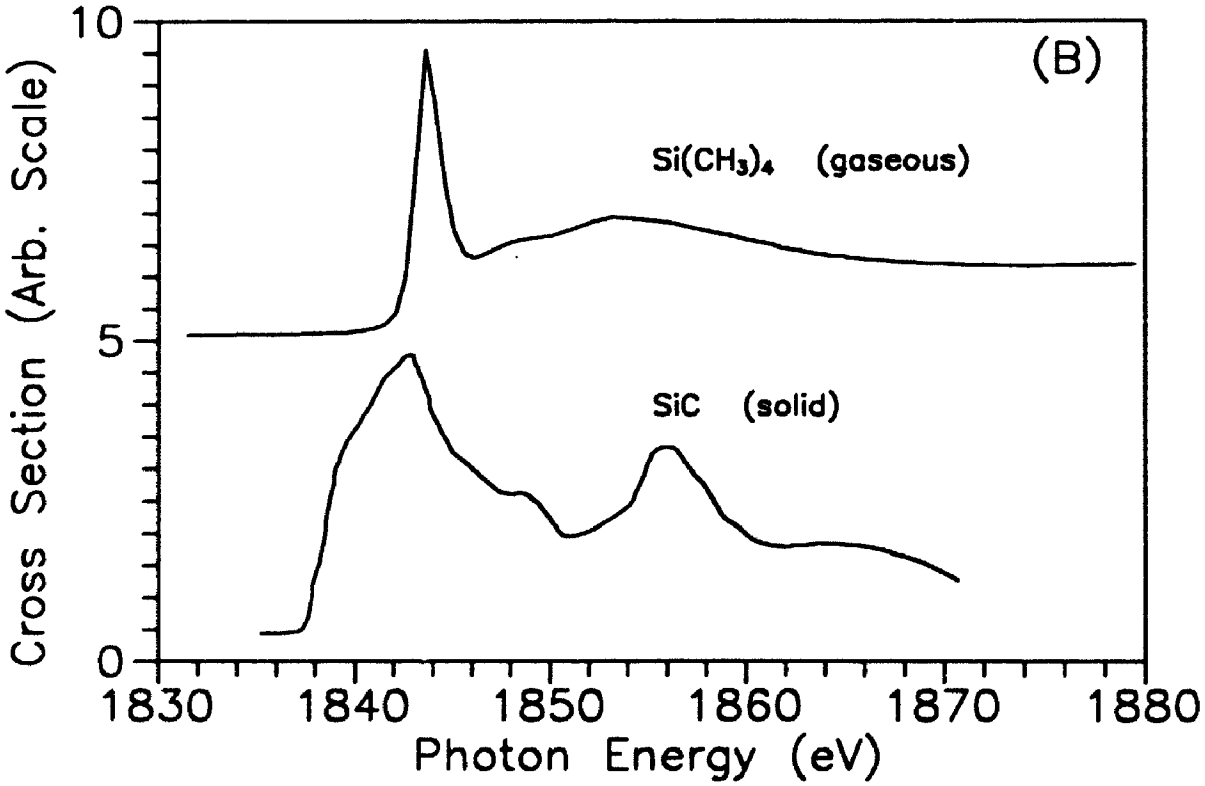
10
5
0
Cross Section (Arb. Scale)
(B)
Si(CH3)4 (gaseous)
SiC (solid)
1830
1840
1850
1860
1870
1880
Photon Energy (eV)

Table IV-5: The positions (in eV) of the peaks in the spectra shown in Figures IV-8 & IV-9A, and the Si 1*s* binding energies. The binding energies of $Si(OCH_3)_4$ and $Si(CH_3)_4$ were determined by comparison of the term values with those of the L-edge spectra and the binding energies of the three intermediate compounds were approximated by linear interpolation from the two end members of the series.

	Molecule $Si(OCH_3)_X(CH_3)_{4-X}$ (Fig IV- 8)					(Fig IV-9)	
Peak	X=0	X=1	X=2	X=3	X=4	SiO_2	DOS (+ 1835 eV)
A	1843.6	1844.0	1844.6	1845.2	-	-	-
B	1848.5	1845.6	1846.5	1847.2	1845.9	1845.1	1845.1
C	-	1849.1	-	-	1847.3	1846.8	1846.8
D	-	-	-	-	-	1850.9	1850.5
E	-	-	-	-	-	1854.5	1855.4
F	1853.3	1855.3	1859.7	1859.8	1860.6	1857.3	1856.9
Si 1*s*	1845.8	1846.3	1846.7	1847.2	1847.6	-	-

Not only are the pre-edge features dissimilar but the continuum shows, perhaps, an even more pronounced difference; however, the continuum features in the solid state do show a qualitative correspondence to the DOS calculation. The fact that there seems to be little correspondence between the gas-phase and the solid state spectra in both the pre-edge and the continuum regions of the 1s edge implies that, unlike the Si 2*p* spectra, the extended long range structure of the solid state SiO_2 has a significant effect on the K-edge spectra.

Figure IV-10 shows the 1s region of TMOS and TMS together with their respective simulations of the pre-edge and the continuum shown below the

experimental data and Figure IV-11 shows the same plot of the 2s region. Table IV-6 lists the peak positions, term values, assignments and oscillator strengths for both the 1s and 2s regions of TMOS and TMS. Because the 2s peak is so weak (see Figure IV-1) no continuum calculation was performed in this study. Although the overall shape of the simulations match that of the experimental data very well, the calculated oscillator strengths are much too low for the Si K-edge of both TMOS and TMS. This results from a large integration mesh that leads to numerical instability when calculating the overlap integral between a very contracted 1*s* and an oscillating outgoing wave. However, because the 1*s* region is so similar to the 2*s* (which is less contracted and hence unaffected by a large integration mesh), and because of the close match between the theory and the experimental data, it is felt that the poor reproduction of the 1*s* oscillator strength is (comparatively) unimportant to this report.

In TMOS the experimental and simulated data match very well in terms of peak position in the 1s region but the simulation of the 1s continuum is much too narrow. The pre-edge features consist of two transitions, both to bound states of a_1 symmetry, with half-height line widths of 2.0 eV. The 2s region of TMOS is essentially identical, but had to be deconvoluted with a slightly broader linewidth (2.5 eV) to create one contiguous peak as seen in the experimental data. The term values of the two peaks in both the Si 1*s* and 2*s* regions are very close with values of 1.70 and -0.23 eV for the two peaks in the 1*s* spectrum and 1.76 and -0.25 eV for the same two peaks in the 2*s* spectrum (see Table IV-6). These values are essentially the same as the second and third transitions in the Si 2*p* spectrum (Table IV-3) which have term values of 1.74 and -0.28 eV respectively.

Figure IV-10. (A) The Si 1*s* XANES spectra of $Si(OCH_3)_4$ (top) and the corresponding MS-Xα SCF simulation (bottom). (B) The Si 1*s* XANES spectra of $Si(CH_3)_4$ (top) and the corresponding MS-Xα SCF simulation (bottom). Dashed lines in both (A) and (B) mark the positions of the individual transitions.

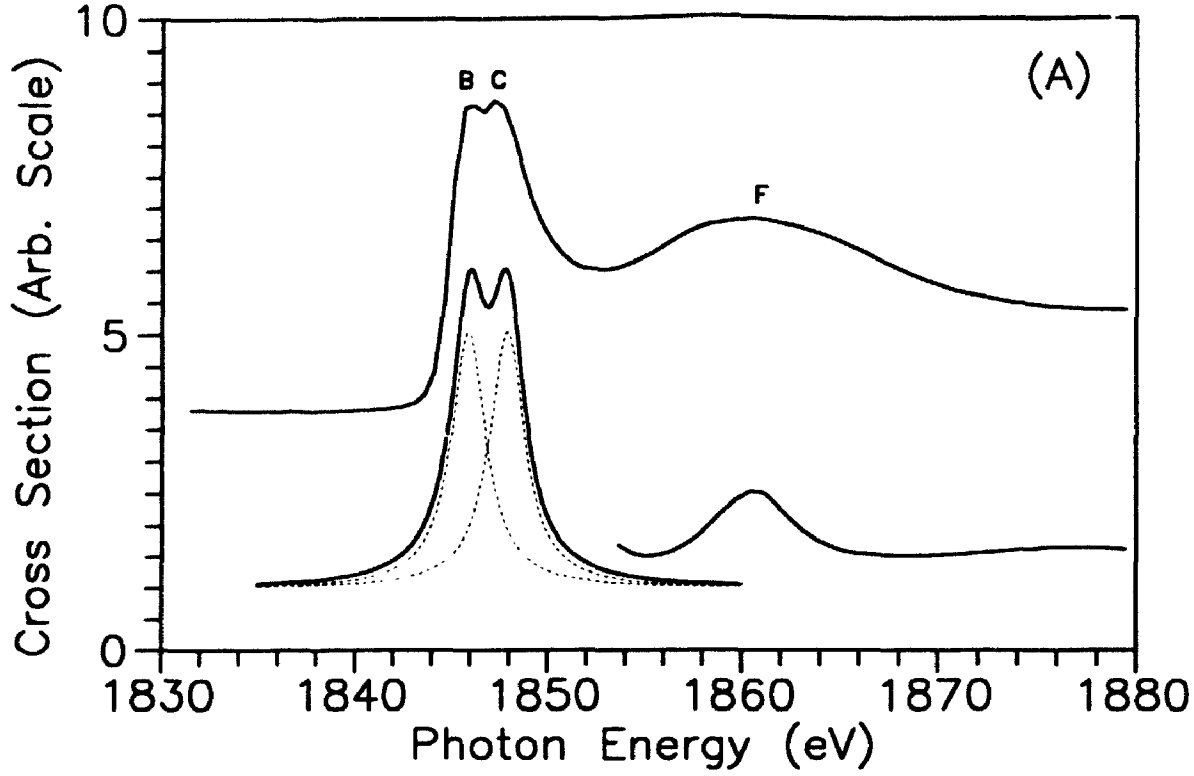
(A)
B C
F
Cross Section (Arb. Scale)
10
5
0
1830
1840
1850
1860
1870
1880
Photon Energy (eV)

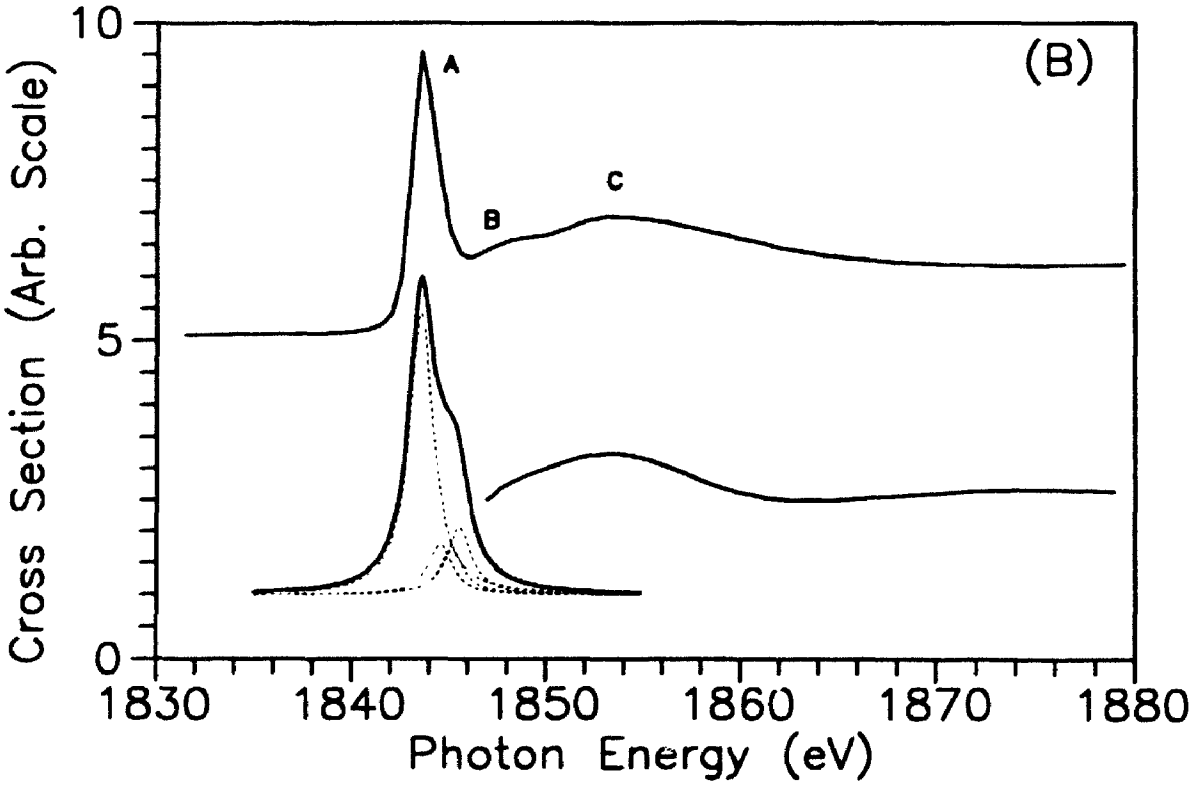
(B)
A
B
C
Cross Section (Arb. Scale)
10
5
0
1830
1840
1850
1860
1870
1880
Photon Energy (eV)

Figure IV-11. (A) The Si 2*s* XANES spectra of $Si(OCH_3)_4$ (top) and the corresponding MS-Xα SCF simulation (bottom). (B) The Si 2*s* XANES spectra of $Si(CH_3)_4$ (top) and the corresponding MS-Xα SCF simulation (bottom). Dashed lines in both (A) and (B) mark the positions of the individual transitions.

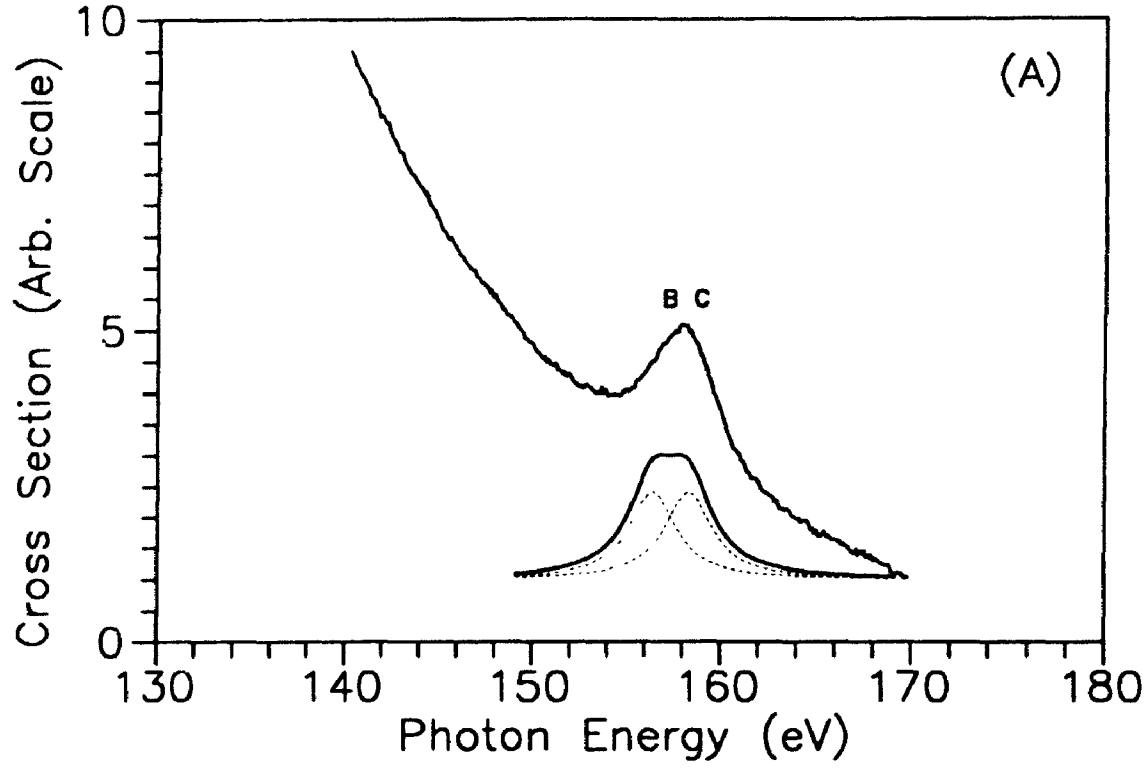
(A)
B C
Cross Section (Arb. Scale)
10
5
0
130
140
150
160
170
180
Photon Energy (eV)

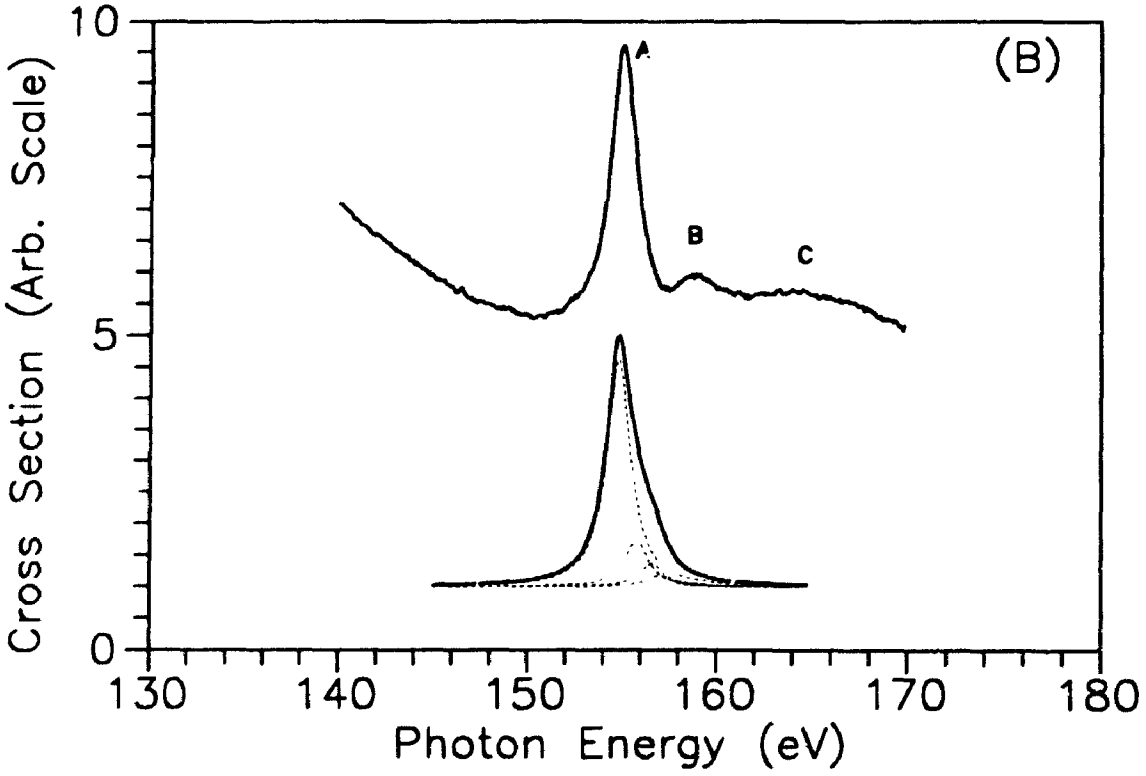
(B)
A
B
C
Cross Section (Arb. Scale)
10
5
0
130
140
150
160
170
180
Photon Energy (eV)

Table IV-6: The calculated orbitals, transition energies, term values and oscillator strengths for the Si 1*s* and Si 2*s* edges of $Si(OCH_3)_4$ and $Si(CH_3)_4$. The Corresponding experimental peak is shown in parenthesis after the energy.

Orbital	Energy (Exp. Peak) (eV)	Term Value (eV)	Oscillator Strength	Remark
$Si(OCH_3)_4$ 1*s*				
a_1	1845.90 (B)	1.70	1.37×10^{-8}	Mixed Ryd.
a_1^*	1847.83 (C)	-0.23	1.42×10^{-8}	Antibonding
$Si(OCH_3)_4$ 2*s*				
a_1	156.26 (B)	1.76	2.67×10^{-5}	Mixed Ryd.
a_1^*	158.12 (C)	-0.25	2.61×10^{-5}	Antibonding
$Si(CH_3)_4$ 1*s*				
$4t_2^*$	1843.65 (A)	2.18	9.95×10^{-9}	Rydberg *p*
$5t_2^*$	1844.62 (A)	1.21	1.78×10^{-9}	Rydberg *p*
$7t_2^*$	1845.26 (A)	0.57	1.58×10^{-9}	Rydberg *p*
$10t_2^*$	1845.69 (A)	0.14	2.39×10^{-9}	Rydberg *p*
$Si(CH_3)_4$ 2*s*				
$4t_2^*$	154.64 (A)	2.20	4.97×10^{-5}	Rydberg *p*
$5t_2^*$	155.67 (A)	1.23	1.00×10^{-5}	Rydberg *p*
$7t_2^*$	156.25 (A)	0.59	5.01×10^{-6}	Rydberg *p*
$10t_2^*$	156.71 (A)	0.13	2.43×10^{-6}	Rydberg *p*

As mentioned above, peaks B and C in the 1*s* spectrum of TMOS result from transitions from the 1*s* orbital to two different orbitals of a_1 symmetry. Both of these transitions are allowed in C_{2v}. In tetrahedral symmetry only transitions from the 1*s* to orbitals of t_2 symmetry are allowed. The second a_1^* orbital (peak C), in tetrahedral symmetry, is the a_1

component of the t_2^* orbital and thus, this transition is allowed in SiO_2. The first a_1^* orbital (peak B) does not transform as the t_2 in tetrahedral symmetry and thus this transition should be completely forbidden in the K-edge spectrum of SiO_2 (Figure IV-9). The weak shoulder on the low energy side of peak C in SiO_2 does however line up with peak B in the spectrum of TMOS suggesting that this transition is weakly allowed even in the tetrahedral environment of SiO_2.

The experimental line widths of the 1s and 2s regions are nearly identical in the case of both TMOS and TMS; but, in the former molecule the 2s peak is slightly broader which obscures the separation of the two peaks. Otherwise, although the relative oscillator strengths differ, the term values for the 1s and 2s regions are essentially identical (see Table IV-6). Because of the strong background in the 2s region of TMOS, direct comparison of the 1s and 2s regions in this compound is difficult. However, it is interesting to note that the 1s and 2s regions in TMS are essentially identical, both consisting of a sharp peak with a half-height width of 1.65 eV followed by two weak features in the continuum which occur at 3.9 and 9.5 eV above the main peak (these are peaks A, B and C in Figures IV-10B & IV-11B). Furthermore, comparison of the 1s region in Figure IV-8 with the 2s region in Figure IV-1 shows remarkable similarities indicating that the features in these regions result from transitions to the same unoccupied orbitals as indicated by the essentially equivalent term values documented in Table IV-6.

In TMS both the 1s and 2s regions are dominated by a single strong transition to a bound orbital of t_2 symmetry accompanied by three smaller transitions each with a linewidth of 1.5 eV. The shoulder on the high energy side of the 1s simulation seems to have no counterpart in the

experimental data. The 2s region of TMS is represented by exactly the same four transitions but the slight difference in relative oscillator strengths in the 2s region yields a better agreement with the experimental data.

The cross section in the Si 1*s* region (pre-edge and continuum) is much smaller than that of the corresponding 2*p* region. Above-edge features in the 2*p* spectra are dominated by intense shape resonances that swamp any small peaks that may be due to the extended band structure or multiple-scattering. In the 1*s* region, because the cross section is much lower, small peaks due to multiple-scattering of the outgoing electron wave become apparent. Because the scattering process depends on long range structure, (at least three atoms from the central species), only very large gas-phase molecules such as $Si[Si(CH_3)_3]_4$ and $Ge[Si(CH_3)_3]_4$ will be helpful in the analysis of K-edge solid state spectra.[36] However, because multiple-scattering plays only a very minor role in the L-edge spectra, gas-phase compounds may be used here as excellent models for solid state systems.

Section IV-5; The L-Edge of The Oxides of The Third Row Elements.

Having established that the L-edge spectra of the gas-phase TMOS and solid state SiO_2 are very similar, it is interesting to compare the L-edge spectra of analogous tetrahedral oxides of the third row elements. Figure IV-12 shows the spectrum of SiO_2, $(Ca)_3(PO_4)_2$, Na_2SO_4, and $NaClO_4$ all plotted on the same scale and Table IV-7 documents the pertinent data. In each compound, the zero point marks the position of the ionization edge.[37] Certain similarities are readily apparent between the four spectra and each spectrum can be broken down into three main regions relative to their respective ionization thresholds: (i) 0-8 eV, (ii) 8-15 eV and (iii) 15 eV and above.

Table IV-7. The peak positions (in eV) relative to their $2p$ ionization edges and assignments for the four spectra shown in Figure IV-12.

Peak	SiO_2	PO_4	SO_4	ClO_4	Assignment
A	0.73	0.82	0.79	1.20	$p_{3/2} \rightarrow a_1^*$
A'	1.30	1.76	2.06	2.78	$p_{1/2} \rightarrow a_1^*$
C	2.93	2.43	2.73	2.01	$p_{3/2} \rightarrow t_2^*$
C'	3.49	3.33	4.04	3.62	$p_{1/2} \rightarrow t_2^*$
D	6.72	5.51	5.28	5.54	Multiple-Scattering
G	9.64	10.11	9.80	10.80	$p_{3/2} \rightarrow d$-Shape Res.
G'	10.25	11.00	11.04	12.35	$p_{1/2} \rightarrow d$-Shape Res.
H	25.7	20.8	18.6	20.5	Maximum of Atomic Cross Section
I	-	-	27.3	26.5	Multiple-Scattering
J	-	-	32.9	33.1	Multiple-Scattering

As one moves across the third row of the periodic table, the peaks in the first region of Figure IV-12 seem to broaden out and coalesce into one broad peak. Part of this broadening is due to the steady increase in the spin-orbit splitting: 0.613 for Si,[23,25] 0.86 for P,[38] 1.21 for S[38] and 1.64 for Cl.[39] A second reason for the broadening and coalescence is the decrease in the lifetime of the $2p$ hole as one moves across the period, although, this is likely a negligible effect because the linewidths here are so much broader than the lifetime widths which are all less than 0.15 eV.

From an analysis of the valence band photoelectron spectra[40] and of molecular orbital calculations[41] of the three isoelectronic anions, PO_4^{3-}, SO_4^{2-} and ClO_4^-, it is obvious that the occupied MO's span a greater range of energy as one moves across the period from phosphorus to sulfur to chlorine. However, the same MO calculations[41] show that the exact opposite is true in the case of the unoccupied antibonding orbitals. That is, the antibonding orbitals become more compressed and span a lesser range of energies as this period is traversed from P to Cl.

It then stands to reason that if the first peaks in the Si $2p$ spectrum of SiO_2 (A, A', C, and C' in Figure IV-12) result from transitions to a_1^* and t_2^* orbitals, then, the first peaks in the spectra of the isoelectronic anions, PO_4^{3-}, SO_4^{2-} and ClO_4^-, should also result from the same transitions. Furthermore, because the energies of the unoccupied orbitals become compressed[41] as one moves from P to Cl, one would expect these peaks to coalesce due to the fact that the a_1^* and t_2^* become closer together. The compression of the unoccupied orbitals coupled with the increase in spin-orbit splitting, explains the trend in the first region of these spectra. In all four spectra, peaks A and A' result from the $p_{3/2}$ and $p_{1/2}$ components of a transition to an a_1^* antibonding orbital and peaks C and C'

Figure IV-12. The 2*p* XANES spectra of the four isoelectronic species SiO_2, PO_4, SO_4 and ClO_4 shifted by 103.65, 131.10, 169.40 and 208.70 eV respectively, so that the 2*p* ionization energy has a value of 0.00 eV. The 2*p* ionization energies were taken from reference 37.

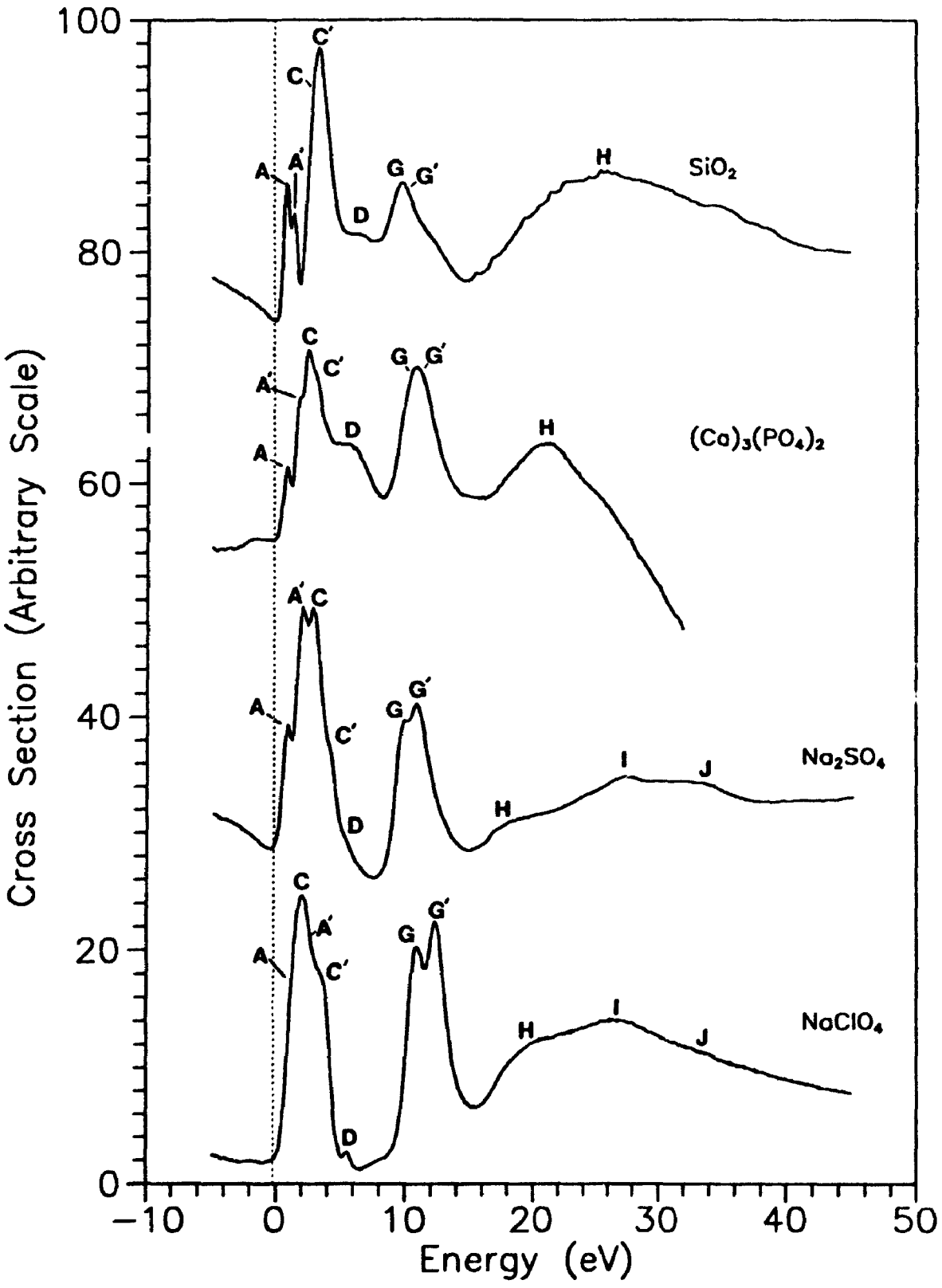
Cross Section (Arbitrary Scale)
Energy (eV)
100
80
60
40
20
0
−10
0
10
20
30
40
50
A
A′
C
C′
D
G
G′
H
I
J
SiO2
(Ca)3(PO4)2
Na2SO4
NaClO4

are the $p_{3/2}$ and $p_{1/2}$ components of a transition to a t_2^* antibonding orbital. In the case of ClO_4^-, the a_1^* and t_2^* are so close together that the $p_{3/2}$ peak of the t_2^* (peak C) is at a lower energy than the $p_{1/2}$ peak of the A_1^* (peak A'). Peak D in this same region also shifts closer to the ionization edge as the period is traversed from Si to Cl; however, the low intensity and large linewidth has prevented resolution of the spin-orbit splitting on this feature.

The second region, from 8-15 eV, has a very strong absorption band in each spectrum (peaks G & G'). In SiO_2 this peak is quite broad, becoming sharper in PO_4^{3-} and then splitting in the case of SO_4^{2-} and splitting even more so in the case of ClO_4^-. The splitting of this peak in the latter two species results from their respective spin-orbit splitting of 1.21 eV for S and 1.64 eV for Cl. The shoulder on the high energy side of this peak in the spectrum of SiO_2 is coincident with a large peak in the DOS calculation presented in Figure IV-3A. The Xα simulations of TMOS suggest that peak G is due to a *d*-shape resonance in TMOS and SiO_2 and thus a similar assignment has been made for the other three solid state spectra in Figure IV-12.

The third region consists of a single broad structureless peak in the case of SiO_2 and PO_4^{3-} with the last two compounds showing more structure in this area. In all four cases peak H corresponds to the position of the cross section maximum[42] for the 2*p* level of Si, P, S and Cl relative to their respective 2*p* ionization edges. Peak H has also been attributed to a t_2 shape resonance and this may also account for some of the intensity. Peaks I and J for the S and Cl moieties may be due to multiple-scattering of the outgoing electron. Other differences in these four spectra may be due to manifestations of the different counter ions in the four examples shown.

Section IV-6; Conclusions.

The $Si(OCH_3)_4$ molecule (TMOS) is an excellent experimental model for the Si 2*p* photoabsorption spectrum and the valence band photoelectron spectrum of SiO_2. The features in the Si 2*p* XANES spectrum of SiO_2 are due primarily to the local structure surrounding the Si atom with long range order playing only a minor role. Furthermore, the MS-Xα SCF calculations on TMOS provide, perhaps, the best explanation of the Si 2*p* spectrum of SiO_2 to date. Density of states calculations may be helpful in this regard but are considerably more time consuming as well as being more expensive, and, calculations done on the SiO_4^{4-} ion suffer from the effects of having a single dangling bond on each of the oxygens.

Gas-phase molecules can be used to model the spectra of solid state compounds in the low energy domain where cross sections are high.For K-edge spectra, or wherever the cross section is low, the dominant features in the above edge region of the XANES spectra of solids will be the result of the extended long range structure (as reflected in the DOS calculations) or due to multiple-scattering of the electron wave off of neighboring atoms in the matrix.

The L-edge spectra of the four isoelectronic species SiO_4^{4-}, PO_4^{3-}, SO_4^{2-} and ClO_4^- are qualitatively very similar despite the fact that their respective 2*p* ionization thresholds range from 103.6 eV for SiO_2 to 208.7 eV for ClO_4^-. This is further evidence that the solid state spectra can be interpreted in terms of molecular orbital theory derived from small molecular analogs.

A suggested use of gas-phase systems to interpret solid state phenomena is in the case of the interfacial regions between bulk Si and SiO_2 monolayers where the actual oxidation state of Si is in question. Here a series of molecules such as $Si[Si(CH_3)_3]_X[OCH_3]_{4-X}$ could be synthesized which mimic the effect of one to four oxygens bonded to a silicon atom in the bulk Si environment. This type of work has already been done by Sutherland *et al.* in which the series $Si[Si(CH_3)_3]_XH_{4-X}$ was successfully used to mimic the effect of one to four hydrogens bonded to a silicon atom on a Si surface.[25]

Section IV-7; References.

1) J.L. Dehmer; J. Chem. Phys., 56(9), 4496, (1971).

2) T.H. DiStefano and D.E. Eastman; Phys. Rev. Lett., 27(23), 1560, (1971).

3) F.C. Brown, R.Z. Bachrach and M.Skibowski; Phys. Rev. B, 15(10), 4781, (1977).

4) A. Bianconi; Surf. Sci. 89, 41, (1979).

5) A. Bianconi and R.S. Bauer; Surf. Sci. 99, 76, (1980).

6) G. Hollinger and F.J. Himpsel, Appl. Phys. Lett., 44, 93, (1983).

7) E.O. Filatova, A.S. Vinogrdov and T.M. Zimkina; Sov. Phys. Solid State, 27(4), 606, (1985).

8) F.J. Himpsel and F.R. McFeely, A. Taleb-Ibrahimi and J.A. Yarmoff; Phys. Rev. B, 38, 6084, (1988).

9) G.R. Harp, Z.L. Han and B.P. Tonner; J. Vac. Sci. Technol. A, 8(3), 2566, (1990).

10) J.A. Tossell; J. Am. Chem. Soc., 97(17), 4840, (1975).

11) J.A. Tossell, D.J. Vaughan and K.H. Johnson; Chem. Phys. Lett., 20(4), 329, (1973).

12) K.H. Tan, G.M. Bancroft, L.L. Coatsworth, and B.W. Yates; Can. J. Phys., 60, 131, (1982).

13) R. Haensel, C Keitel, P. Schreiber and C. Kunz; Phys. Rev., 188, 1375, (1969).

14) B.X. Yang, F.H. Middleton, B.G. Olson, G.M. Bancroft, J.M. Chen, T.K. Sham, K. Tan and D.J. Wallace; Nuc. Instr. and Meth. in Phys. Res., 316,

422, (1992)

15) S. Bodeur, P. Millie and I. Nenner; Phys. Rev. A, 34(4), 2986, (1986).

16) S. Bodeur, P. Millie and I. Nenner; Phys. Rev. A, 41(1), 252, (1990).

17) J.D. Bozek, J.N. Cutler, G.M. Bancroft, L.L. Coatsworth, K.H. Tan, D.S. Yang and R.G. Cavell; Chem. Phys. Lett., 165, 1, (1990).

18) M. Kasrai, M.E. Fleet, T.K. Sham, G.M. Bancroft K.H. Tan and J.R. Brown; Solid State Comm., 68, 507, (1988)

19) K.H. Johnson; Adv. Chem. Phys., 7, 143, (1973).

20) J.W. Davenport, Ph.D. Thesis, Univ. of Pennsylvania, USA, (1976)

21) L. Latter; Phys. Rev. 99, 510, (1955).

22) *Numerical Data and Functional Relationships in Science and Technology*, K.H. Hellwege and A.M. Hellwege Editors, Springer-Verlag, New York, (1976), Vol. 7 page 296 and Vol 15 page 454.

23) J.D. Bozek, G.M. Bancroft and K.H. Tan; Chem. Phys., 145, 131, (1990) and references therein.

24) J.S. Tse, Z.F. Liu, J.D. Bozek and G.M. Bancroft; Phys. Rev. A, 34, 2986, (1989).

25) D.G.J Sutherland, G.M. Bancroft and K.H. Tan; J. Chem. Phys., 97(11), 7918, (1992).

26) R.N. Nucho and Anupam Madhukar; Phys. Rev. B, 21, 1576, (1980).

27) D. Li, G.M. Bancroft, M. Kasrai, M.E. Fleet, X.E. Feng, K.H. Tan and B.X. Yang; to be published.

28) D.W. McComb, P.L. Hansen and R. Brydson; Microsc. Microanal. Microstruct., 2, 561, (1991).

29) W.H.E. Schwarz; Chem. Phys., 13, 153, (1976).

30) W.H.E. Schwarz; Chem. Phys., 11, 217, (1975).

31) Z.F. Liu, J.N. Cutler, G.M. Bancroft, K.H. Tan, R.G. Cavell and J.S.

Tse; Chem. Phys., 168, 133, (1992)

32) D.W. McComb, R. Brydson, P.L. Hansen and R.S. Payne; J. Phys. Cond. Matter, 4, 8363, (1992)

33) J.R. Chelikowsky and M. Schlüter; Phys. Rev. B, 15, 4020, (1977).

34) Yong-nian Xu and W.Y. Ching; Phys. Rev. B, 44, 11048, (1991)

35) Ph. Sainctavit, J. Petiau, C. Laffon, A.-M. Flank and P. Lagarde; *X-Ray Absorption Fine Structure*; S.S. Hasnain, Editor; Ellis Harwood, Publishers; New York; 38-40 (1991)

36) J. Li, D.G.J. Sutherland, T.K. Sham, G.M. Bancroft and K.H. Tan; to be published.

37) *Practical Surface Analysis by Auger and X-ray Photoelectron Spectroscopy*; Eds. D. Briggs and M.P. Seah, John Wiley and Sons, New York, (1983)

38) R.G. Cavell and K.H. Tan; Chem. Phys. Lett., 197, 161, (1992).

39) K. Ninomiya, E. Ishiguro, S. Iwata, A. Mikuni and T. Sasaki; J. Phys. B, 14, 1777, (1981).

40) V.I. Nefedov, YU. A. Buslaev, N.P. Sergushin, YU.V. Kokunov, V.V. Kovalev and L. Bayer; J. Elec. Spec. and Rel. Phen., 6, 221, (1975).

41) H. Johansen; Theoret. Chim. Acta, 32, 273, (1974).

42) J.J Yeh and I. Lindau; Atomic Data and Nuclear Data Tables, 32, 1, (1985).

CHAPTER V:

VIBRATIONAL SPLITTING IN Si 2p CORE-LEVEL PHOTOELECTRON SPECTRA OF SILICON MOLECULES

Section V-1; Introduction.

Gelius[1] *et al* first observed core-level vibrational structure on the C 1*s* level in the photoelectron spectrum of CH_4. Prior to this observation it was normally assumed that non-bonding core orbitals, like non-bonding valence levels[2], would exhibit little or no vibrational splitting. Using monochromatized synchrotron radiation to obtain narrow photon linewidths (<0.1 eV) work from this lab has recently resolved and characterized vibrational structure on the Si 2*p* and P 2*p* levels of five molecules: SiH_4[3], SiF_4[3], SiD_4[4], CH_3-SiH_3[3] and PH_3[5]. Also characterized in these studies were the unresolved vibrational structure on such molecules as $Si(CH_3)_4$, $SiCl_4$, and $(CH_3)_3SiX$ (X=H, Cl, I)[6]. In all molecules studied thus far the vibrational structure is dominated by the totally symmetric vibrational mode which transforms as the totally symmetric a_1 irreducible representation.

The core-equivalent model has proven valuable in determining not only when vibrational splitting will be present but also in predicting the magnitude of the vibrational frequency in the ion state[3,6]. For example, the substantial decrease (0.06 Å) in bond length in going from SiH_4 to its core-equivalent[7] PH_4^+ (or PH_3) is consistent with a large vibrational progression in the Si 2*p* photoelectron spectrum of SiH_4. Furthermore, the observed ion-state Si-H vibrational frequency of 2379 cm^{-1} is much closer to that of the core-equivalent PH_3 (2327 cm^{-1}) than it is to the ground-state vibrational frequency of SiH_4 (2180 cm^{-1}). On the other hand, the very small change in bond length between GeH_4 and its core-equivalent AsH_3, or between HI and HXe^+ is helpful in rationalizing the fact that there is

little vibrational structure in the photoelectron spectra of the Ge 3*d* levels of GeH_4[5] and the I 4*d* levels of HI.[8]

This chapter reports the high resolution Si 2*p* gas-phase photoelectron spectra of 23 molecules: the SiH_XD_{4-X} (X=0-4) series; the $Si(CH_3)_X(OCH_3)_{4-X}$ (X=0-4) series; the $Si(CH_3)_X[N(CH_3)_2]_{4-X}$ (X=1-4) series; the $SiH_X[Si(CH_3)_3]_{4-X}$ (X=0-4) series, and SiH_3-CH_3, SiH_3-SiH_3, SiH_3-SiH_2-SiH_3, $Si(CH_3)_3$-$Si(CH_3)_3$, $Ge[Si(CH_3)_3]_4$ and $[Si(CH_3)_2]_6$.

The objectives of this chapter are listed as follows:

(i) To record the Si 2*p* photoelectron spectra of a wide variety of silicon compounds in order to systematically compare the effects that different ligands (ie. H, D, CH_3, $[N(CH_3)_2]$, OCH_3, F and $Si(CH_3)_3$) have on the vibrational manifold observed in core-level photoelectron spectroscopy. This is important for testing the validity of the core-equivalent model, which is of particular importance for interpreting the resolved spectra and as a predictive tool for analyzing the unresolved spectra.

(ii) To use the vibrationally resolved spectra of the five compounds in the hydrogen/deuterium series (SiH_XD_{4-X}) to verify the model previously used by Bozek[7] *et al* for the unresolved spectra of the series R_xSiH_{4-x} ($R=CH_3$, C_2H_5; X=0-4). This model, using vibrational overtones, is essential to the interpretation of the spectra of silicon compounds where all four ligands are not the same.

(iii) To study the chemical dependence of binding energy more accurately than could have been done previously, with particular attention paid to the difference between the adiabatic and the vertical ionization potentials that results from a large vibrational manifold. This may be of importance when

correlating binding energies with theoretical calculations or Si KLL Auger shifts

(iv) To study the effect of equivalent cores[7,9] (as in the molecules SiH_3-SiH_3, SiH_3-SiH_2-SiH_3 and $Si[Si(CH_3)_3]_4$) where vibronic coupling caused by core-hole localization in the ion state can lead to a dramatically different vibrational manifold than that observed for SiH_4 or $Si(CH_3)_4$.

(v) To use this first extensive series of high resolution core-level spectra to predict the importance of vibrational structure in the photoelectron spectra of other molecules, polymers and surfaces. In particular this Si data can be used to predict the expected C *1s* vibrational structure (and linewidth) in photoelectron spectra of organic molecules and polymers such as the C *1s* spectrum of polyethylene[10] and vibrational structure present in the photoelectron spectra of surface adsorbates on Si.

Section V-2; Experimental.

All compounds were obtained commercially in high purity from The Aldrich Chemical Company (TMS, TKTS), Huls America (all methoxy and dimethyl-amino compounds), Matheson Gas Company (Silane), MSD Isotopes (disilane and all deuterated compounds) and Solkatronics (trisilane) and used without further purification except for the following four:

(i) 1,1,1-Trimethyl disilane (TMDS, $SiH_3[Si(CH_3)_3]$) was purchased commercially from Huls America and purified by vacuum distillation.

(ii) Tris trimethylsilyl silane (TTMS, $H\text{-}Si[Si(CH_3)_3]_3$) was synthesized from tetrakis trimethylsilyl silane (TKTS, $Si[Si(CH_3)_3]_4$) according to Gillman[11].

(iii) Bis trimethylsilyl silane (BTMS, $H_2Si[Si(CH_3)_3]_2$) was synthesized from TTMS (see ii above) according to Gillman[11].

(iv) Tetrakis trimethylsilyl germane (TKTG, $Ge[Si(CH_3)_3]_4$ was synthesized according to Brook[12] *et al.*

The samples were introduced directly into the gas cell of the spectrometer at pressures of ~ $5X10^{-3}$ torr. Gaseous samples were used as received, and liquid samples were de-aerated by repeated freeze-pump-thaw cycles to remove any dissolved oxygen or nitrogen. The solid TKTS (see ii above) was heated to 60°C to increase its vapor pressure. Constant sample pressure was maintained for the time required to accumulate the data for each spectrum.

The photoelectron spectrometer used to record the spectra has been described in detail elsewhere[13] and to a lesser extent in Chapter II.

Briefly, the spectrometer consists of a McPherson 36 cm mean radius electron energy analyzer with 1mm entrance and exit slits resulting in a theoretical electron resolution, $\Delta E/E$, of 1/720. For electron kinetic energies of ~25 eV the theoretical value of $\Delta E/E$ is ~0.04 eV but in practice the electron linewidth is 50 ± 10 meV. Assorted differential pumping was used on the spectrometer and beamline to isolate the high pressure of the gas cell from the optical components of the beamline.

With the exception of SiD_4, the spectra of the other four compounds (SiH_4, SiH_3D, SiH_2D_2 and $SiHD_3$) in the hydrogen deuterium series, disilane (SiH_3-SiH_3) and trisilane (SiH_3-SiH_2-SiH_3) were recorded using a Quantar model #3395A position sensitive detector (PSD). All other spectra were recorded using a single channel electron multiplier. The decreased acquisition time of the PSD allowed the use of narrower slit widths on the monochromator thereby affording the narrower photon line widths required to resolve the features in the spectrum of disilane.

All spectra were recorded using the CSRF Mark IV Grasshopper monochromator at the Aladdin synchrotron of the University of Wisconsin at Madison. An 1800 groove/mm grating was employed in the monochromator resulting in a minimum *practical* photon resolution of 0.12 eV at 130 eV photon energy with the channeltron and 0.08 eV with the PSD. Total line widths of ~150 meV were obtained for the resolved photoelectron spectra obtained with the channeltron and <130 meV for those recorded with the PSD. The spectra obtained with the PSD were of very similar quality to those obtained previously on the undulator beamline at the Aladdin synchrotron[3]. Unlike the C 1*s* photoelectron spectra of organic molecules, post-collisional interaction (PCI) in the photoelectron spectra of silicon compounds does not play a significant role due to the long lifetime of the Si 2*p* hole state and

the relatively low energy of the Auger electron.

The binding energy of each compound was measured through the use of an internal calibrant, namely the $3d_{5/2}$ line of krypton which has a binding energy of 93.798 eV. Calibration spectra were recorded with a photon energy of 128 eV which created a kinetic energy window void of any Kr Auger peaks that might interfere with the Si 2*p* spectrum. At low kinetic energies (20 to 25 eV) the velocity of the photoelectrons is approximately 1% of the speed of light and thus relativistic effects are negligible; hence, all binding energies reported are accurate to within ≤0.01 eV.

Spectra recorded with the PSD originally had approximately 800 data points per spectrum. This number was reduced by averaging five points into one using binomial coefficients according to Equation V-1.

$$m_i = (n_{i-2} + 4n_{i-1} + 6n_i + 4n_{i+1} + n_{i+2})/16 \qquad \text{[Eq. V-1]}$$

where n_i is the number of counts in the i^{th} original data point and m_i is the weighted average of the five points surrounding n_i. The factor 1/16 is introduced to normalize the sum of the coefficients.

The spectra that were fit to a vibrational progression were deconvoluted with a Lorentzian-Gaussian line shape using a nonlinear least squares procedure constrained to use only one peak shape split by the Si 2*p* spin-orbit and vibrational splitting[3,6].

Section V-3; The Series SiH_xD_{4-x}.

The isotope effect for the Si 2*p* core-level vibrational splitting is beautifully shown by the photoelectron spectra of SiH_4 and SiD_4 shown in Figure V-1. The linewidths in the SiD_4 spectrum are considerably larger (see Table V-1) than in SiH_4 because the SiD_4 spectrum was recorded prior to the installation of the position sensitive detector (PSD).

Table V-1. Binding energy, linewidth, Si 2*p* ion state vibrational frequency and Frank-Condon factors for the five molecules SiH_xD_{4-x} (X=0 to 4).

Molecule	Binding Energy (eV)	Linewidth (meV)	Bond	Vibrational Frequency (meV)	Frank - Condon Factors
SiH_4	107.316(5)	128	Si-H	295(5)	66.3:29.1:4.6
SiH_3D	107.31(1)	127	Si-H	294(10)	75.5:19.7:3.8
			Si-D	202(10)	78.6:16.4:3.4:0.5
SiH_2D_2	107.30(1)	131	Si-H	305(10)	83.4:12.2:2.3
			Si-D	219(10)	67.4:26.3:5.9:1.0
$SiHD_3$	107.31(1)	130	Si-H	305(10)	91.1:8.5:0.5
			Si-D	210(10)	59.6:31.0:7.7:1.7
SiD_4	107.31(1)	153	Si-D	212(5)	53.6:34.5:9.6:2.3

Figure V-1. Si $2p$ photoelectron spectra of SiH_4 (Top) and SiD_4 (Bottom). The fine lines in the spectra represent the individual contributions from each vibrational and spin-orbit quantum state. The heavy line running through the data points represents the sum of all individual contributions. Error bars mark the raw data points.

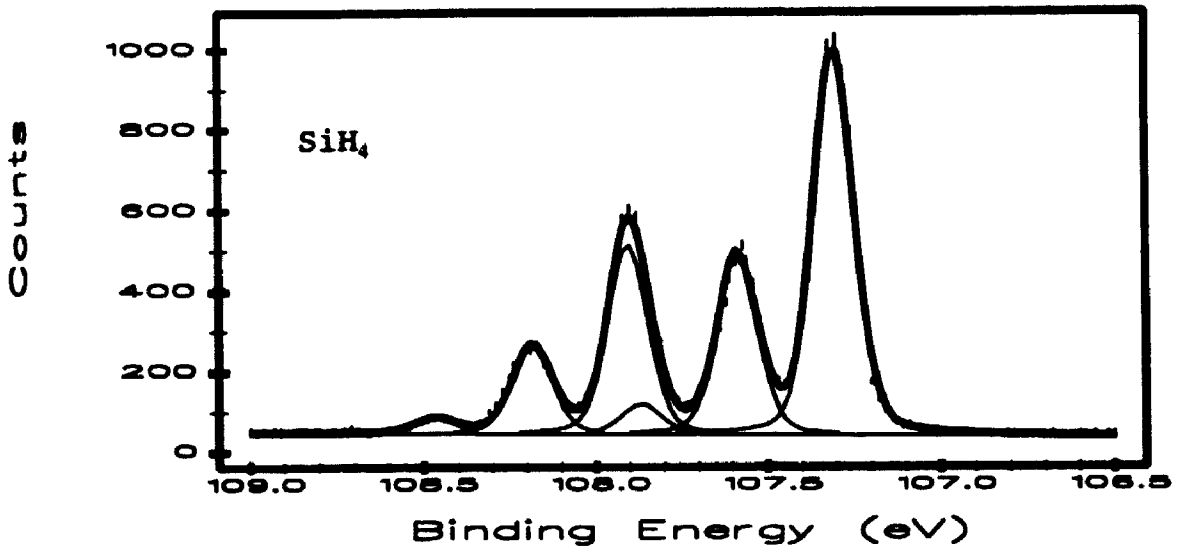
Counts
1000
800
600
400
200
0
SiH4
109.0
108.5
108.0
107.5
107.0
106.5
Binding Energy (eV)

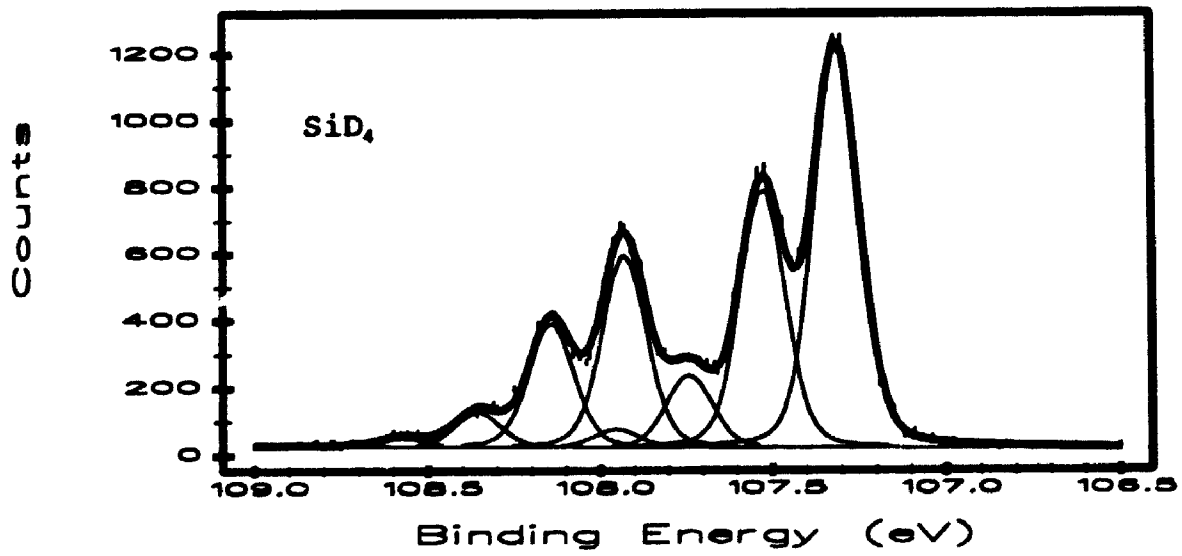
Counts
1200
1000
800
600
400
200
0
SiD4
109.0
108.5
108.0
107.5
107.0
106.5
Binding Energy (eV)

The largest peak in each spectrum (at lowest binding energy - 107.31 eV) corresponds to the Si $2p_{3/2}$ adiabatic ν=0 to ν'=0 transition. In each spectrum this line is then split in two by spin-orbit coupling to yield the $2p_{3/2}$ and $2p_{1/2}$ lines separated by the Si 2p spin-orbit splitting of 0.613 eV. In both spectra the two spin-orbit lines are then further split by a vibrational manifold corresponding to the totally symmetric ν_1 vibrational mode of a_1 symmetry. In SiH_4 the vibrational manifold consists of three peaks (ν'=0,1,2) with an energy spacing of 0.295 eV. This frequency is very similar to that expected from the core-equivalent species, PH_3[6] (see Table V-2). The last vibrational peak (ν'=2) in the $2p_{3/2}$ series falls almost directly under the first peak of the $2p_{1/2}$ series and thus can only be detected directly in the Si $2p_{1/2}$ series as the smallest peak at highest binding energy. In SiD_4 there are four vibrational peaks corresponding to ν'=0,1,2,3 with an energy spacing of 0.212 eV. Again, there is some overlap between the $2p_{3/2}$ and the $2p_{1/2}$ vibrational series. The vibrational frequency is, again, very close to that of the core-equivalent species PD_3 (Table 2).

The ratio of the two vibrational frequencies (0.212/0.295 = 0.719) is exactly that predicted from the square root of the ratio of the reduced masses of Si-H and Si-D according to Equation V-2,

$$(\nu(\text{Si-D})/\nu(\text{Si-H})) = [\mu(\text{Si-H})/\mu(\text{Si-D})]^{1/2} \qquad \text{[Eq. V-2]}$$

where ν(Si-D) and ν(Si-H) are the vibrational frequencies, respectively, for

Table V-2. Bond length, bond angle, ground state (ν(GS)) and ion state (ν(IS)) vibrational frequency for several simple silicon molecules, their respective core-equivalents and some organic analogs and their core-equivalents.

Molecule	Bond	Bond Length (Å)	Bond Angle	ν(GS) (cm^{-1})	ν(IS) (cm^{-1})
SiH_4	Si-H	1.4811	109.5	2180	2379
PH_3	P-H	1.4200	93.345	2327	2331
PH_4^+	P-H	-	-	2295	-
SiD_4	Si-D	1.4786	109.5	1545	1710
PD_3	P-D	-	93.3	1694	-
PD_4^+	P-D	-	-	1654	-
$Si(CH_3)_4$	Si-C	1.875	109.5	693.7	-
$P(CH_3)_3$	P-C	1.844	98.8	652	-
$Si[N(CH_3)_2]_4$	Si-N	1.725	-	892	-
$P[N(CH_3)_2]_3$	P-N	1.70	96.5	985	-
$Si(OCH_3)_4$	Si-O	1.614	115.5	840	-
$P(OCH_3)_3$	P-O	1.620	100.5	1012	-
SiF_4	Si-F	1.5535	109.5	800.8	847
PF_3	P-F	1.5633	97.7	893	-
CH_4	C-H	1.08070	109.5	2917	3162
NH_3	N-H	1.0138	107.23	3335.9	-
NH_4^+	N-H	-	-	3040	-
CD_4	C-D	1.079	109.5	2085	-
ND_3	N-D	1.013	107.21	2419	-
ND_4^+	N-D	-	-	2214	-
$C(CH_3)_4$	C-C	1.537	109.5	1455	-
$N(CH_3)_3$	N-C	1.458	110.9	1043	-
CF_4	C-F	1.31925	109.5	908.4	-
NF_3	N-F	1.3648	102.37	1035	-

the Si-D and Si-H bonds and $\mu_{(Si-H)}$ and $\mu_{(Si-D)}$ are, respectively, the reduced masses of Si-H and Si-D.

The larger Frank-Condon factors (see Table V-1) and larger vibrational manifold in SiD_4 is expected as a result of the lower vibrational frequency in the neutral molecule, and this fact is supported by theoretical calculations done on both molecules[14].

In compounds where there is only one type of ligand (ie. CH_4, SiH_4, SiD_4, SiF_4 and PH_3) it is comparatively easy to determine the nature of the vibrational manifold provided that the energy spacing between successive vibrational quantum states in the ion is large enough to be resolved. In all such cases reported thus far there is only one vibrational mode that transforms as the totally symmetric a_1 irreducible representation, and this single vibrational mode is the only one that has been observed for molecules with the same ligands. As dissimilar ligands are substituted, the spectrum becomes more complicated for two reasons. First, there is the simple fact that there are now two different vibrational frequencies; one for ligand(s) "A" and another for ligand(s) "B" and this leads to the possibility of overtone[6] bands in the photoelectron spectrum. Secondly, as dissimilar ligands are added, the point group of the molecule changes, thereby allowing several vibrational modes, each with a different frequency, to transform as the same totally symmetric a_1 representation. Assuming that *all* vibrational modes of a_1 symmetry are allowed, then there exists the possibility of each type of ligand exhibiting more than one vibrational frequency. Bozek[6] *et al* investigated this problem with the R_xSiH_{4-x} (R=CH_3, C_2H_5) compounds at ~170 meV resolution but could not resolve the different modes or overtones. The spectra, however, were deconvoluted using one vibrational frequency for each type of ligand, and overtone bands.

Figure V-2. Si 2*p* photoelectron spectra of SiH_3D (Top), SiH_2D_2 (Middle) and $SiHD_3$ (Bottom).

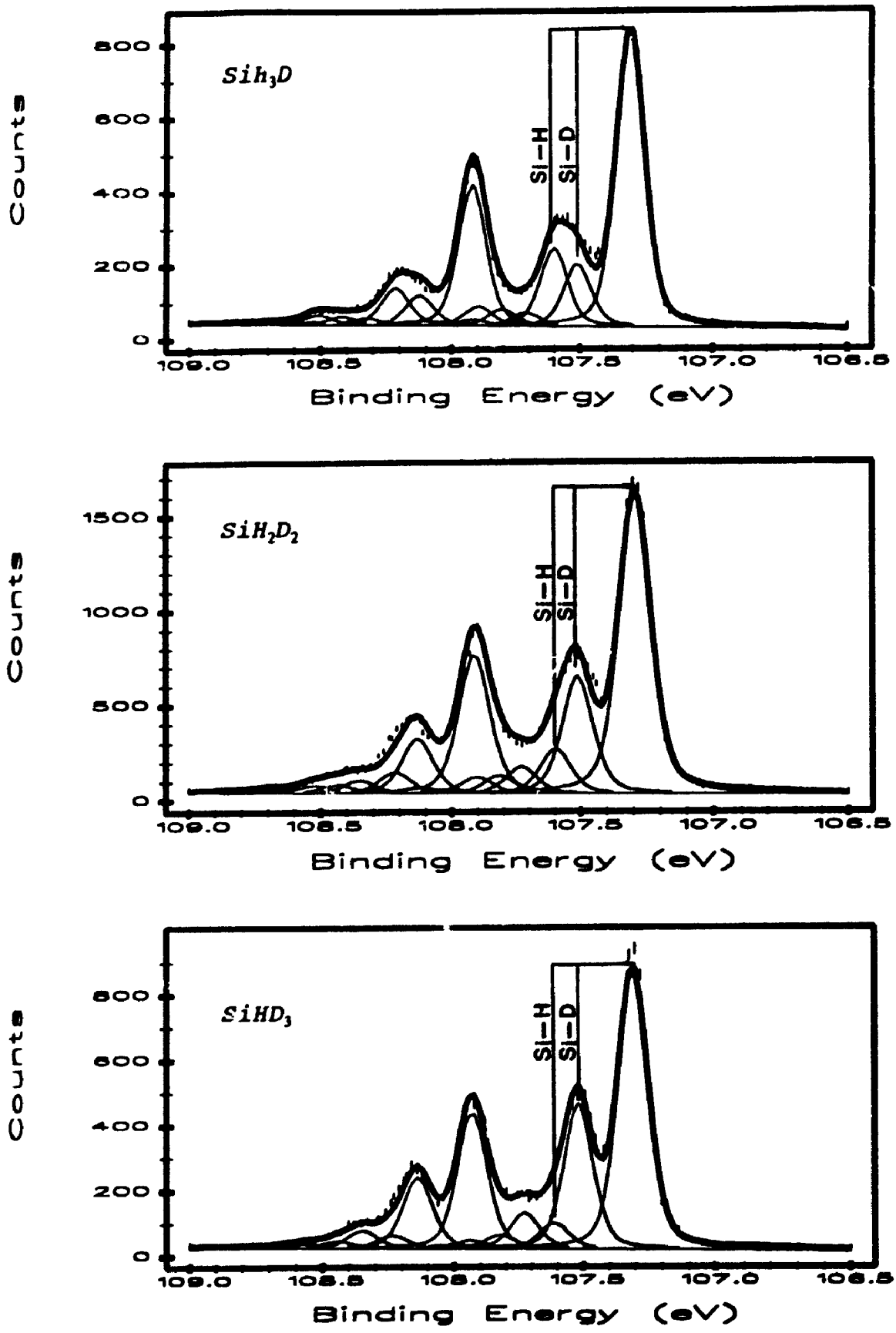
SiH_3D
SiH_2D_2
$SiHD_3$
Si–H
Si–D
Counts
Binding Energy (eV)
109.0
108.5
108.0
107.5
107.0
106.5

To investigate the effect of two different ligands more carefully the spectra of the three compounds SiH_xD_{4-x} (x=1-3), shown in Figure V-2, were recorded. Qualitatively the trend in the vibrational manifolds from SiH_4 to SiD_4 is obvious. In SiH_3D the most intense *vibrational* peak (ν'=1, at ~107.60 eV) corresponds to the Si-H symmetric stretch with a frequency of 0.294 eV, while for $SiHD_3$ the most intense *vibrational* peak (ν'=1 at 107.52 eV) corresponds to the symmetric vibrational mode for Si-D with a frequency of 0.210 eV. It is immediately obvious that in all three spectra in Figure V-2 the peaks corresponding to the fundamental Si-D vibrations are proportionally much more intense than those of the Si-H fundamental vibrations.

The Frank-Condon factors reported in Table V-1 for SiH_4 and SiD_4 were calculated by normalizing the sum of the areas of the vibrational bands to equal 100. In the mixed compounds there are two vibrational series but the initial peak, at ~107.31 eV, is the ground state vibrational level in the ion and as such is common to both series. Because one cannot tell what percentage of this peak is due to Si-H or Si-D vibrations, the Frank-Condon factors for the mixed compounds were calculated by using the full intensity of the initial peak at ~107.31 eV as the first peak in both series; for both series in each molecule the Frank-Condon factors total 100. It is clear from Table V-1 that the Frank-Condon factors for the Si-H vibrations in SiH_3D are quite similar to those for SiH_4. Similarly, the Frank-Condon factors for the Si-D vibrations in $SiHD_3$ are very close to those of SiD_4, thus emphasizing the smooth trend from SiH_4 to SiD_4 seen in Figures V-1 and V-2.

The vibrational frequencies for the Si-H and Si-D stretching modes were not fixed during the fitting procedure for any of the three mixed

hydrogen/deuterium compounds and hence the values are not exactly the same as those found for SiH_4 and SiD_4 (Table 1). The small differences in the ion state vibrational frequencies are commensurate in magnitude with those found in the infrared[15] spectra of the same series of compounds.

More quantitatively, SiH_3D is a symmetric top belonging to the point group C_{3v} and from the infrared spectra[15] of this molecule it has three vibrational modes that transform as the a_1 representation. Two of these (at 2187 cm^{-1} and 1597 cm^{-1}) correspond to within ±50 cm^{-1} to the totally symmetric stretching mode (ν_1 of symmetry a_1) observed in silane[15] and silane-d_4[15] (see Table V-2), while the third mode of a_1 symmetry corresponds to the hydrogen bending mode (914 cm^{-1})[15] in the neutral species SiH_3D.

If there was a substantial contribution from any of these three vibrational modes other than the totally symmetric stretching vibration then one would expect, from the infrared data presented earlier (Table V-2), to see a substantial change in the linewidth of the initial peak in the photoelectron spectrum of SiH_3D. For instance, one might expect to see a distinct shoulder on the high binding energy side, separated from the main peak by ~914 cm^{-1} (0.113 eV) - the energy of the third vibrational mode of a_1 symmetry in SiH_3D. This possibility has been abandoned on the basis of two facts: (i) the line width in SiH_3D is actually slightly smaller than the other two spectra in Figure V-2 and (ii) the linewidth and line shape in SiH_3D is essentially identical to that of SiH_4 in which there is only one vibrational mode of a_1 symmetry, namely that of the totally symmetric stretching vibration. On the basis of this evidence the mixed hydrogen/deuterium silanes have been fit to only two vibrational frequencies - one corresponding approximately to that found in the photoelectron spectrum of SiH_4, and a second one corresponding approximately to that found

in SiD_4 (see Table V-1).

It is interesting to note that the spectral data for SiH_3D cannot be satisfactorily fit by simple proportional addition (ie. in a ratio of 3:1) of the spectra of SiH_4 and SiD_4. Frank-Condon factors for vibrational quantum states where $\nu'>1$ are much smaller in the case of all the mixed hydrogen/deuterium compounds than in either silane or silane-d4. Furthermore, as suggested above, the vibrational peaks that result from Si-D vibrations seem to dominate the spectra in all three compounds shown in Figure V-2. Even in the spectrum of SiH_3D where the H:D ratio is 3:1 the $\nu'=1$ peaks (~107.52 eV for Si-D; 107.61 eV for Si-H) are quite close in intensity.

Vibrational overtones result when one of the excited vibrational states of one ligand acts as the ground vibrational state of the other. Thus, for instance, in the spectrum of SiH_3D each of the three vibrational peaks resulting from Si-H vibrations can act as the ground state for the four Si-D vibrations. As a result, taking into account spin-orbit splitting, three Si-H vibrations and four Si-D vibrations each spectra in Figure V-2 is fit to 2X3X4=24 individual peaks. However, because the intensity of overtones is given by the product of the intensity of the fundamental vibrations, many of them are too small to be seen. Indeed, the spectra could be fit reasonably well with just the three Si-H and the four Si-D vibrational peaks. (The clearest example of vibrational overtones is in methyl silane - Figure V-8 below)

Section V-4; The Series $Si(CH_3)_x(OCH_3)_{4-x}$.

Figure V-3 shows the spectra of tetramethyl silane (TMS, $Si(CH_3)_4$) and tetramethoxy silane (TMOS, $Si(OCH_3)_4$) with the scale in the TMOS spectrum shifted by 1.5 eV to higher binding energy. Each spectrum has been fit to a vibrational progression with the energy spacing determined from that of the core-equivalent molecules, $P(CH_3)_3$ and $P(OCH_3)_3$ (see Table V-3). The P-C vibrational frequency in trimethyl phosphine is 652 cm^{-1} (0.081 eV)[16] and the P-O frequency in trimethyl phosphite is 1012 cm^{-1} (0.125 eV)[16] (Table V-2). These values, respectively, have been used to fit the vibrational progressions in the photoelectron spectra of TMS and TMOS. Although the vibrational modes in TMOS are not quite resolved there are strong suggestions of a vibrational manifold very similar to that found previously in SiF_4[3]. The spectrum of TMOS is fit to a vibrational manifold of ten peaks each split by the spin-orbit interaction for a total of twenty different states each with a half-width of 170 meV, where as the spectrum of TMS is fit to a vibrational manifold of 7 peaks for a total of 14 states each with a half-width of 150 meV. The large linewidths in TMOS are likely due to the excitation of other vibrations such as C-O or C-H which blur the resolution of the Si-O stretching frequency. Because the vibrational energy spacing is too small to be resolved (especially in the case of TMS) it is impossible to tell if these fits are exact, but, certainly *they are a very reasonable representation of the vibrational manifolds in the photoelectron spectra of these compounds.*

The spectrum of TMS is deconvoluted in a considerably different

Figure V-3: Si 2*p* Photoelectron spectra of TMS (top) and TMOS (bottom). The vibrational energy spacing was chosen from that of the core-equivalent species (see text).

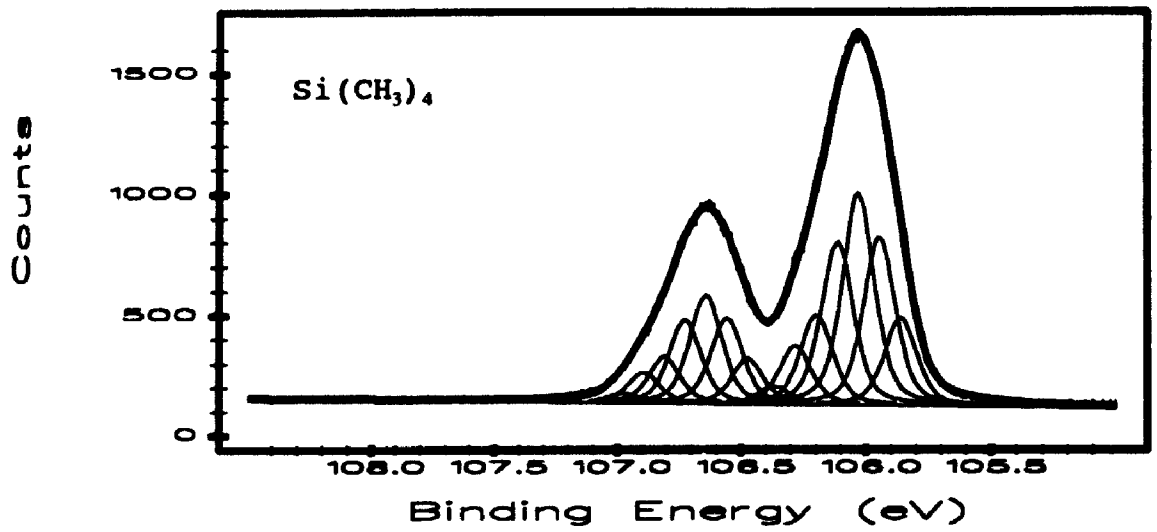
Si(CH3)4
Counts
1500
1000
500
0
108.0 107.5 107.0 106.5 106.0 105.5
Binding Energy (eV)

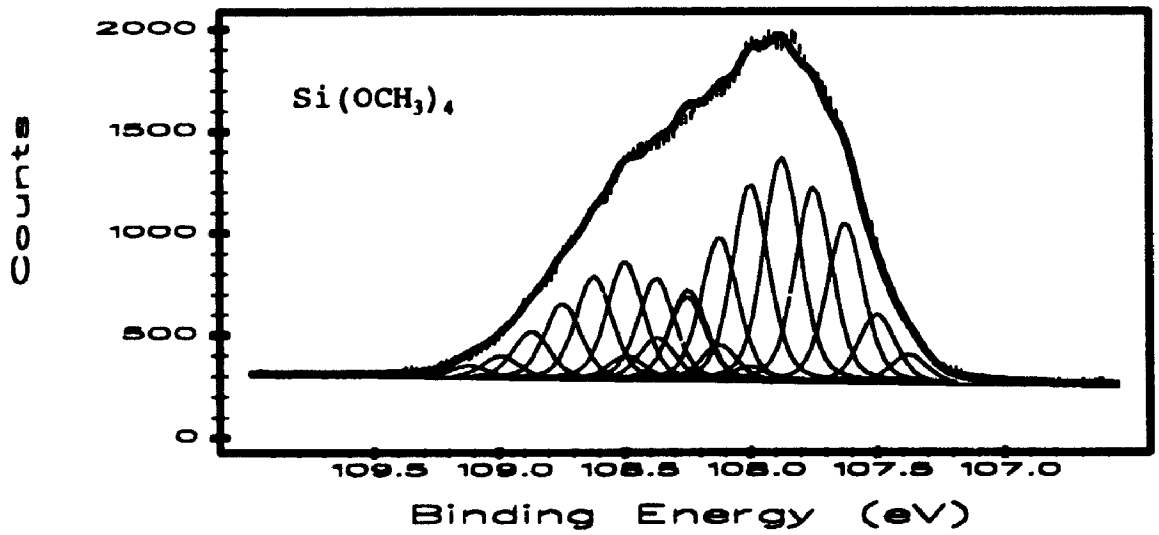
Si(OCH3)4
Counts
2000
1500
1000
500
0
109.5 109.0 108.5 108.0 107.5 107.0
Binding Energy (eV)

manner from that published previously by Bozek[6] *et al*: this work uses a fairly symmetric vibrational progression whereas they used a very asymmetric progression. Bozek *et al* argue that electron donation from the four carbons to the silicon will increase the rate of Auger decay and thereby shorten the lifetime of the core hole causing a broadening of the linewidth via Heisenberg's uncertainty principle. However, recent calculations[17] show that the SiH_4 inherent linewidth is ~32 meV and the lifetime width of a Si 2*p* line does not increase by more than 5 meV in going from SiH_4 to $Si(CH_3)_4$. Given this small change in the calculated inherent linewidth it seems very unlikely that the methyl substituents in TMS could elicit a change in the lifetime great enough to justify the 242 meV linewidths in TMS (compared with 117 meV SiH_4) suggested by Bozek[6]. Furthermore, the I 4*d* linewidth does not change by more than 50% in going from ICl to I_2CH_2[18].

As a result of this new information, the spectrum of TMS has been fit to seven vibrational states (instead of six suggested previously[6]) each with a linewidth of 150 meV (as opposed to 242 meV[6]) with a vibrational energy spacing of 0.084 eV (0.081 eV[6]). The slightly larger vibrational energy spacing and the extra vibrational state compensate for the smaller linewidth but combine to force a reorganization of the Frank-Condon factors. The present spectrum is deconvoluted with a symmetric vibrational envelope; the intensity starts out quite small, increases to a maximum value in the third vibrational state and then steadily decreases for the remaining four. Although this is in contrast with the non-symmetric (steadily decreasing) vibrational envelope used by Bozek *et al*[6] it is more in keeping with the vibrational manifolds of other molecules, such as SiF_4[3] and TMOS, that have relatively small vibrational frequencies. Even though SiI_4 and SiD_4 both exhibit a non-symmetric (steadily decreasing) vibrational envelope, it can

be argued that evidence for a symmetric vibrational envelope in molecules with lower vibrational frequency is suggested even in the spectrum of SiD_4. Here the the Frank-Condon factor for the vibrational state corresponding to $\nu'=1$ is much larger (see Figure V-1 and Table V-1) than the same vibrational state in SiH_4 which of course has a much larger vibrational frequency. If this "trend" can be extrapolated to the case of $Si(CH_3)_4$ then its vibrational envelope should have a more symmetric distribution of intensities, similar to the resolved vibrational spectrum of SiF_4[3].

As a result of the large vibrational manifolds in the spectra of TMS and TMOS, the mixed methyl/methoxy compounds, including overtones, could have as many as 2x7x10=140 vibrational excitations. However, given the example of the hydrogen/deuterium series where vibrational states that have $\nu'>1$ are very weak, the actual number of states that make significant contributions to the spectra in the methyl/methoxy series is much less than 140. Such a large number of peaks is likely never to be resolved in molecules of this type, and hence the three spectra of the mixed methyl/methoxy silanes have been fit only to a simple spin-orbit doublet. For the sake of comparison with the remainder of the series the data for TMS and TMOS shown in Figure V-3 has also been re-fit in the same manner. The data for all five spectra, each fit to a spin-orbit doublet, is shown in Figures V-4 and V-5 and the spectral parameters are summarized in Table V-3. On going from TMS to TMOS, the series of five compounds shows the gradual disappearance of the valley that separates the two peaks and the linewidth of the two-peak fit increases. This is clearly indicative of the increased vibrational manifold that results from the replacement of methyl ligands with methoxy groups (Figure 3). Table V-3 gives both the vertical and the estimated position of the adiabatic binding energy for these five compounds.

Figure V-4: Si 2*p* photoelectron spectra of TMS (top) and TMOS (bottom). The same data presented in Figure V-3 has been fit to only a simple spin-orbit doublet.

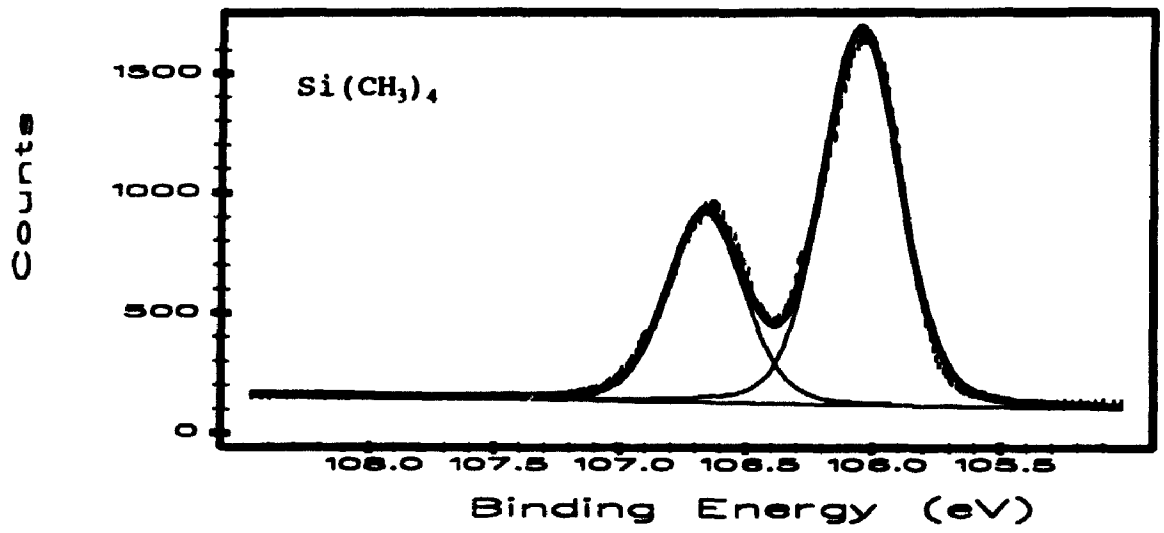
Si(CH3)4
Counts
1500
1000
500
0
108.0 107.5 107.0 106.5 106.0 105.5
Binding Energy (eV)

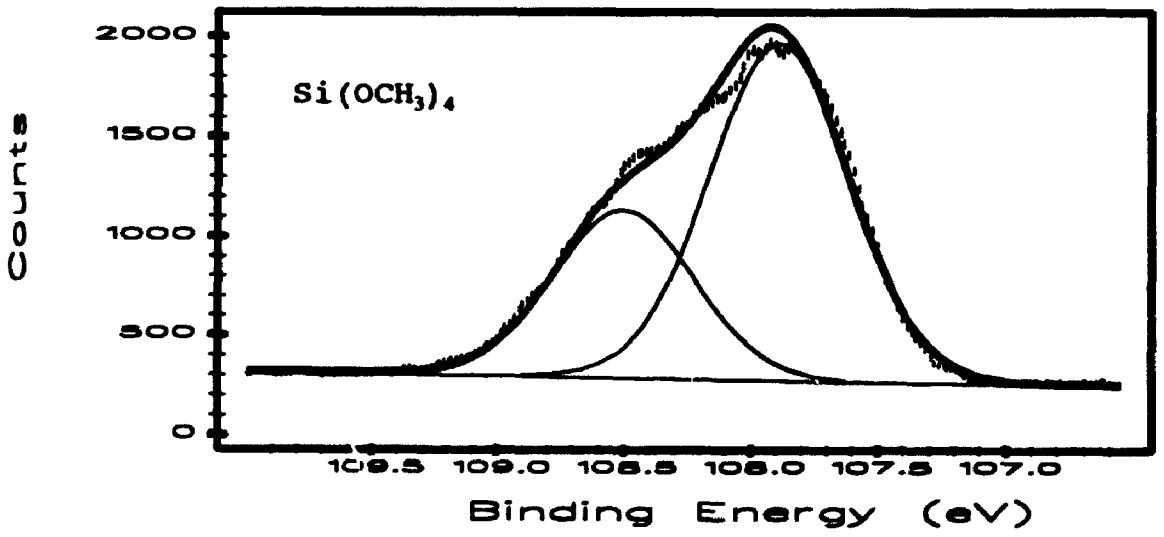
Si(OCH3)4
Counts
2000
1500
1000
500
0
109.5 109.0 108.5 108.0 107.5 107.0
Binding Energy (eV)

Figure V-5. Si 2*p* photoelectron spectra of $(CH_3)_3Si(OCH_3)$ (top), $(CH_3)_2Si(OCH_3)_2$ (Middle) and $(CH_3)Si(OCH_3)_3$ (Bottom).

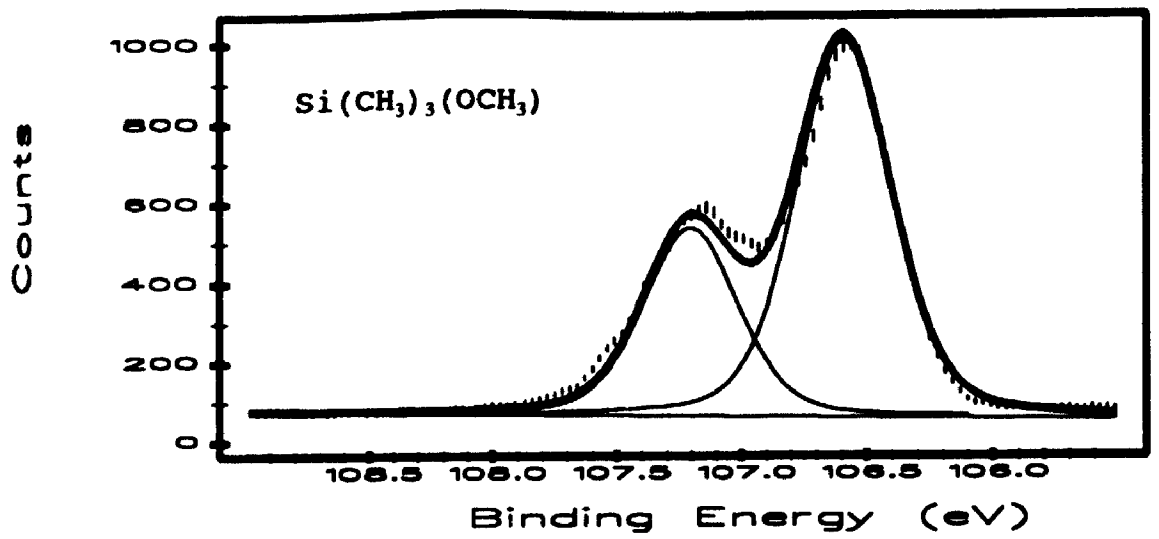
Si(CH3)3(OCH3)
Counts
1000
800
600
400
200
0
108.5 108.0 107.5 107.0 106.5 106.0
Binding Energy (eV)

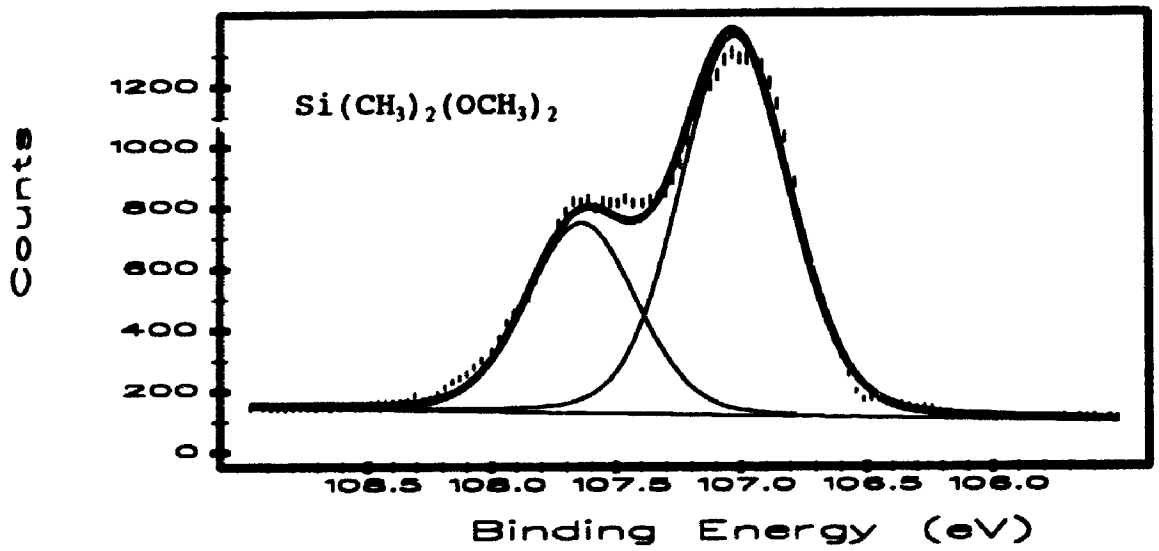
Si(CH3)2(OCH3)2
Counts
1200
1000
800
600
400
200
0
108.5 108.0 107.5 107.0 106.5 106.0
Binding Energy (eV)

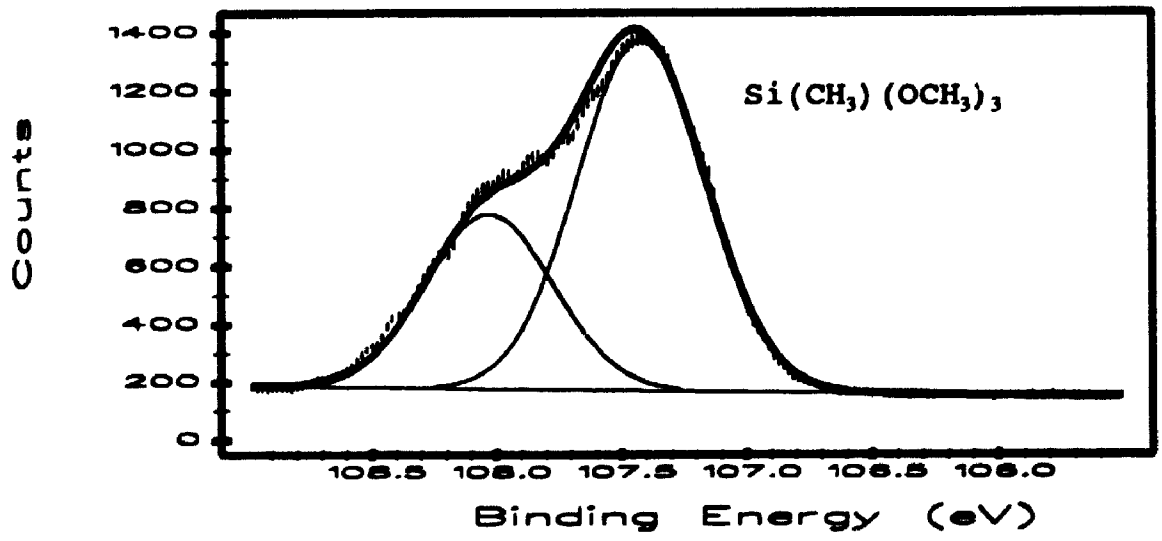
Si(CH3)(OCH3)3
Counts
1400
1200
1000
800
600
400
200
0
108.5 108.0 107.5 107.0 106.5 106.0
Binding Energy (eV)

Obviously, the adiabatic binding energy has larger errors because one cannot be sure whether one is actually seeing the ν=0 -> ν'=0 transition, especially in the mixed compounds. The *difference* between the vertical and adiabatic binding energies varies from 0.18 eV in TMS to 0.50 eV in TMOS. Note the smooth change in linewidth across the series (See Figure V-6).

Table V-3. Linewidths, vertical binding energy and adiabatic B.E. for the eight compounds in the methyl/methoxy and the methyl/dimethyl amino series (Figures V-4, V-5 and V-7). The linewidths quoted from the two-peak fit are accurate to within ± 20 meV.

Molecule	Line Width (meV)	Vertical B.E. (eV)	Adiabatic B.E. (eV)	Vibrational Frequency*
$Si(CH_3)_4$	355	106.04(1)	105.86(2)	0.084
$Si(CH_3)_3(OCH_3)$	449	106.59(1)	106.3(1)	-
$Si(CH_3)_2(OCH_3)_2$	514	107.02(1)	106.6(1)	-
$Si(CH_3)(OCH_3)_3$	605	107.41(1)	107.0(1)	-
$Si(OCH_3)_4$	647	107.89(1)	107.42(2)	0.125
$Si(CH_3)_3[N(CH_3)_2]$	414	106.09(1)	105.7(1)	-
$Si(CH_3)_2[N(CH_3)_2]_2$	467	106.14(1)	105.7(1)	-
$Si(CH_3)[N(CH_3)_2]_3$	498	106.18(1)	105.8(1)	-

* As seen in Figure V-3

Figure V-6. Plot of linewidth versus the number of methoxy (or dimethyl amino) ligands attached to silicon. The point at (0,355) corresponds to TMS which is common to both series.

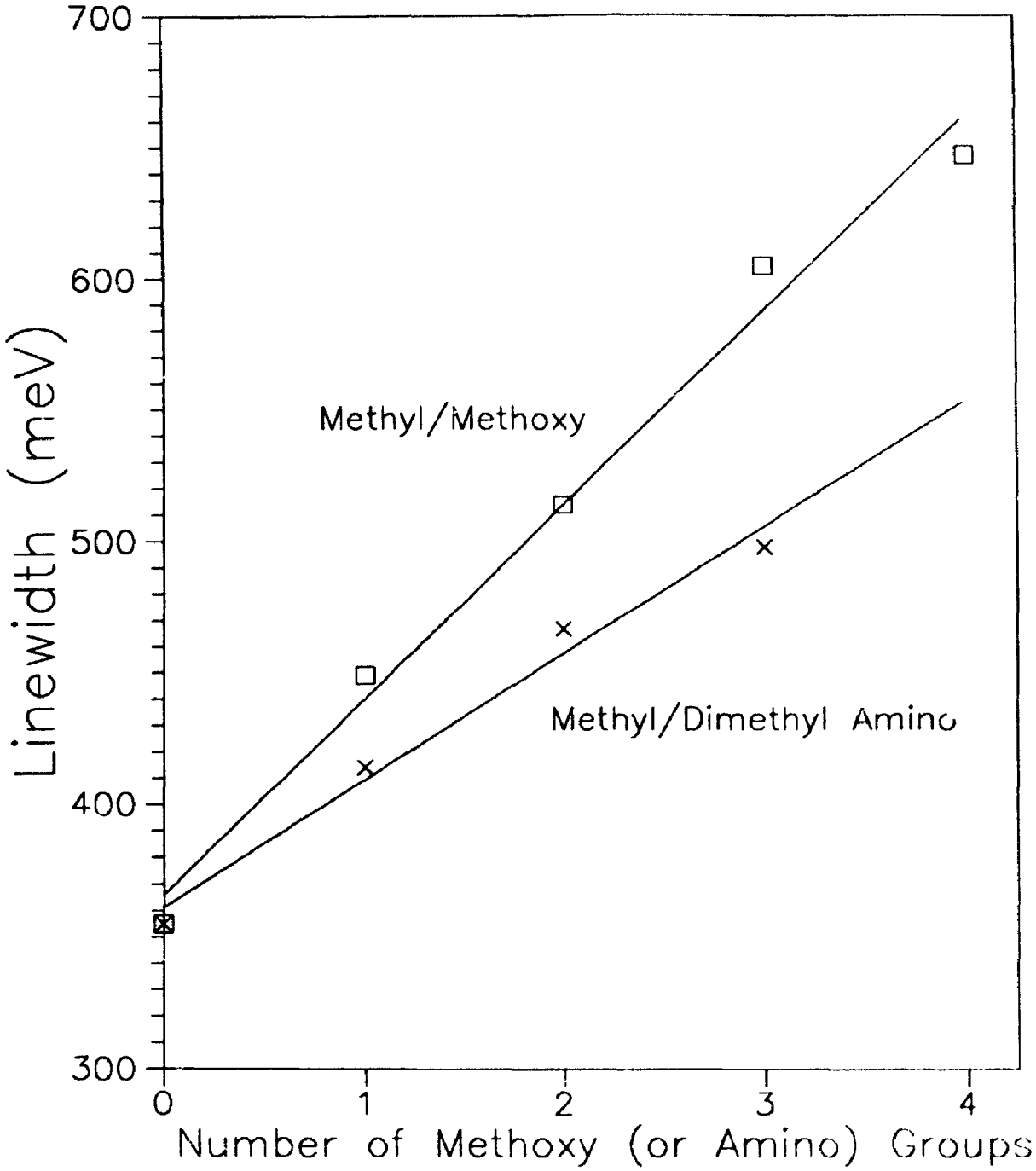
700
600
500
400
300
Linewidth (meV)
Methyl/Methoxy
Methyl/Dimethyl Amino
0
1
2
3
4
Number of Methoxy (or Amino) Groups

Section V-5; The Series $Si(CH_3)_x[N(CH_3)_2]_{4-x}$.

Figure V-7 shows the spectra of the three compounds $Si(CH_3)_3[N(CH_3)_2]$, $Si(CH_3)_2[N(CH_3)_2]_2$ and $Si(CH_3)[N(CH_3)_2]_3$. The first compound in this series is TMS (discussed in Section V-4) and the last compound, $Si[N(CH_3)_2]_4$, could not be procured. As in the case of the methyl/methoxy series each spectrum has been fit only to a simple spin-orbit doublet in order to avoid the complexity of trying to fit multiple vibrational overtones. The spectral parameters are summarized in Table V-3.

From the core-equivalent species (Table 2) the $^{+}$Si-N stretching frequency in the Si 2*p* ion should be approximately 985 cm^{-1} (0.122 eV)[16]. As in Section V-4, when the methyl groups are replaced with the dimethylamino groups the linewidths become considerably larger, but at a much slower rate than in the methyl/methoxy series. For instance, the spectrum of the tri-amino compound in Figure V-7 has approximately the same linewidth (0.498 eV, see Table V-3), as that of the the di-methoxy compound (0.513 eV, see Table V-3) and a considerably smaller linewidth than its tri-methoxy analog which was shown in Figure V-5. Figure V-6 shows a plot of linewidth verses the number of substituents for the five compounds in the methyl/methoxy series and for the four compounds in the methyl/dimethyl amino series. The datum point at the coordinates (0,355) corresponds to TMS and is common to both series. The strong linear correlation here is, again, indicative of an incremental increase in the number of vibrational states that become populated when methyl ligands are substituted with either methoxy or dimethyl amino groups. Since the vibrational frequencies are

Figure V-7. Si 2*p* photoelectron spectra of $(CH_3)_3Si[N(CH_3)_2]$ (top), $(CH_3)_2Si[N(CH_3)_2]_2$ (Middle) and $(CH_3)Si[N(CH_3)_2]_3$ (Bottom).

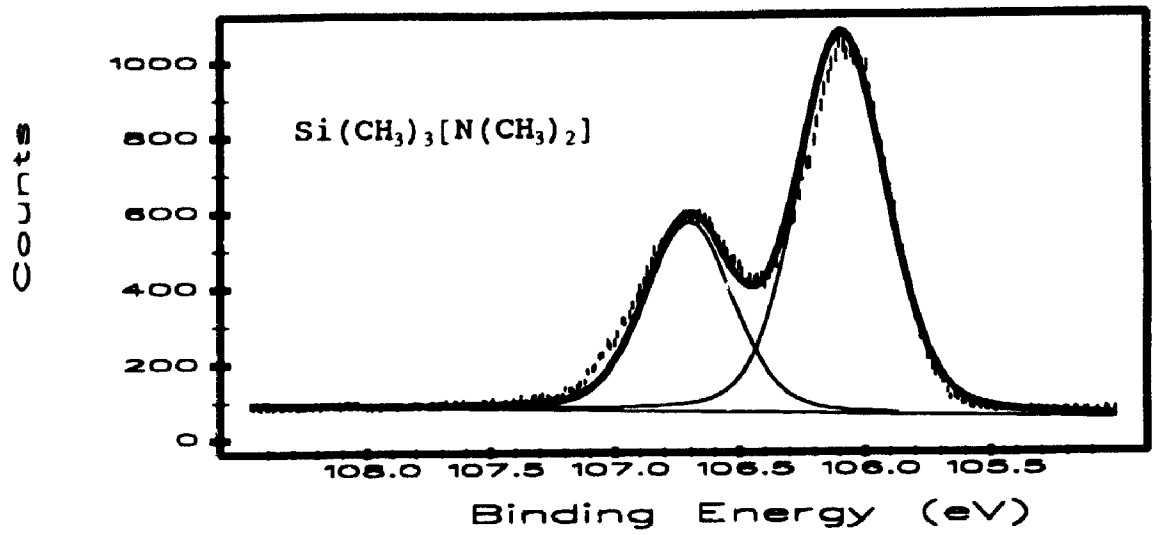
Si(CH3)3[N(CH3)2]
Counts
1000
800
600
400
200
0
108.0 107.5 107.0 106.5 106.0 105.5
Binding Energy (eV)

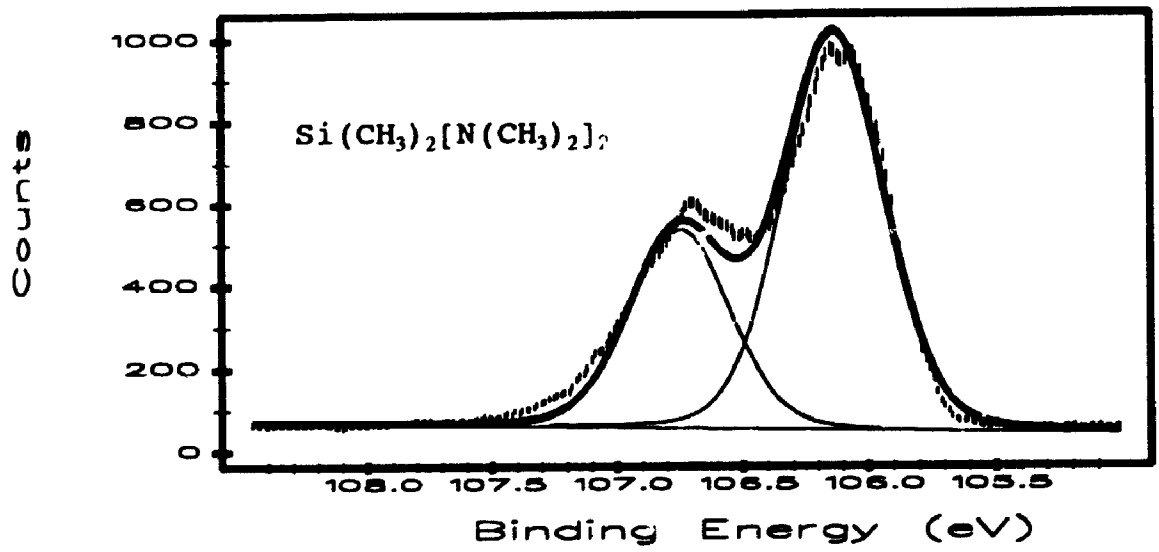
Si(CH3)2[N(CH3)2]2
Counts
1000
800
600
400
200
0
108.0 107.5 107.0 106.5 106.0 105.5
Binding Energy (eV)

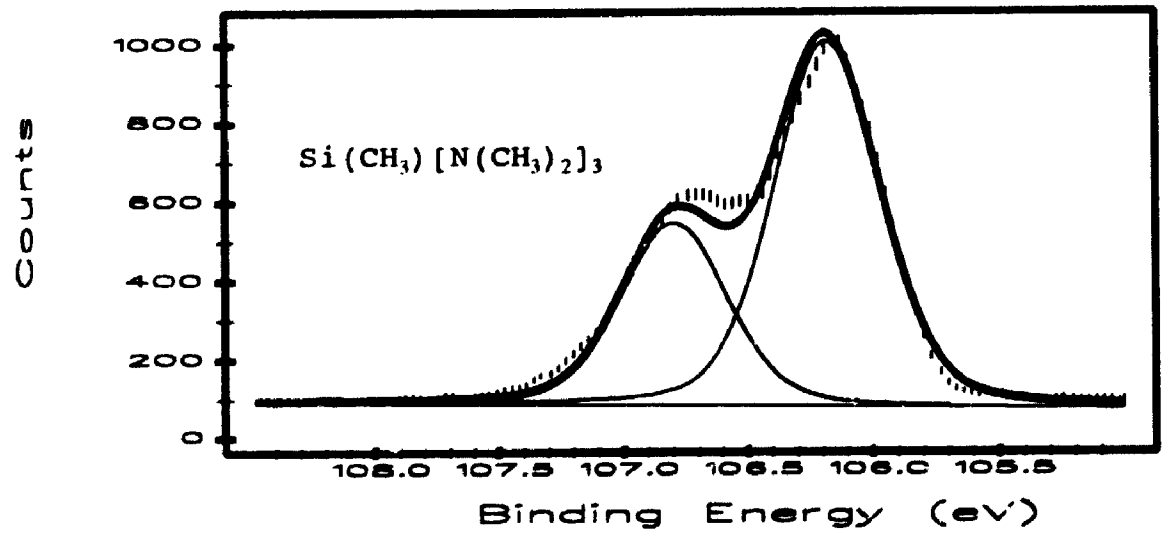
Si(CH3)[N(CH3)2]3
Counts
1000
800
600
400
200
0
108.0 107.5 107.0 106.5 106.0 105.5
Binding Energy (eV)

very similar for $Si[N(CH_3)_2]_4$ and for $Si(OCH_3)_4$ (and for their core-equivalents), the smaller linewidths for the amino compounds compared with the methoxy analogs shows that the vibrational manifold for the Si-N vibrations is larger than that for the Si-C vibrations but smaller than that of Si-O. This is commensurate with nitrogen's intermediate position in the periodic table. It also establishes a trend for the vibrational manifold of light elements bonded to silicon (the number of vibrations is shown in parenthesis): H(3); D(4); C(7); N(>7,<10); O(10); F(11)[3,6].

The Si-X bond length in SiX_4 compounds decreases steadily by approximately 0.1 Å as one moves across the periodic table from X=CH_3, $N(CH_3)_2$, OCH_3 and F (Table 2); this delineates the increasing bond strength across this series. Although one might expect, from the increase in the vibrational manifold, to find that the *difference* in bond length between Si-X and P-X would increase across this series, no such trend relating the bond length in silicon compounds to their core-equivalents can be found (Table 2). It could be that because of the different geometry in the core-equivalent molecules, PX_3 may not be a suitable analog when X is a large ligand such as methoxy or dimethyl amino. The bond angles in these PX_3 compounds are far from the 109.5° found in SiX_4 and vary from 93.3° to 100.5°. The core-equivalent model seems to work well for simple molecules such as CH_4, SiH_4 and SiD_4, but clearly the phosphine analogs are not good core-equivalents in most cases. Even in the case of SiF_4, the core-equivalent, PF_3, provides no better approximation to the vibrational frequency or to the bond length in the ion state than does the neutral species SiF_4 (Table 2). Clearly better energy resolution is still required to test the consistency of this model in predicting ion state vibrational frequencies in core-level electron spectroscopy.

It is important to note that although the term "binding energy" refers to the *adiabatic ionization potential* (the transition from ν=0 to ν'=0) it is usually measured as the *vertical ionization potential* (the position of greatest intensity). The distinction between these two terms is very important. As seen from the spectrum of TMOS in Figure V-3 the vertical binding energy can differ from that of the adiabatic binding energy by as much as 0.50 eV. This can be of significant importance when comparing experimental data with theoretical calculations or when comparing the binding energies of two different molecules[19]. For instance, as mentioned above the difference between the vertical and the adiabatic binding energies for TMOS is 0.50 eV whereas for TMS the difference is only 0.18 eV. Thus, even relative chemical shifts cannot be measured reliably unless the position of the adiabatic ionization potential is known thereby emphasizing the importance of vibrational resolution.

Kelfve[19] *et al.* have plotted the observed vertical binding energy versus the calculated binding energy for a large series of silicon compounds (Figure # 9 in ref. 19). They have constrained the line of best fit to the ideal condition of unit slope but the actual best fit of the data (by inspection) has a slope that is much closer to a value of 2. Although they cite insufficiencies in the calculation procedure as possible sources of error there can be no doubt that other errors are introduced due to their inability to measure adiabatic binding energies. There is no way to tell from their data whether the use of adiabatic binding energies will improve or degrade the agreement with the calculated values, but adiabatic binding energies are obviously required in the future for similar comparisons between theory and experiment.

Section V-6; Disilane and Trisilane.

The observed vibrational structure in photoelectron spectroscopy usually results from the excitation of totally symmetric modes resulting from the linear coupling between electronic and nuclear motion. In systems with degenerate or nearly degenerate core orbitals, ionizations of core electrons may result in allowed excitations of non-totally symmetric vibrational modes[9] due to vibronic coupling between electronic and vibrational quantum states. This theory has recently been tested by Ma *et al.* on the K shell photoabsorption spectra of benzene[20], ethylene[20-22] acetylene[22] and ethane[22] as well as some simple oxides.[22] Further evidence of vibronic coupling in core level spectroscopy is presented in Chapter III of this thesis which also covers the theoretical aspects of this phenomenon.

Figure V-8 shows the vibrational manifolds in the Si 2*p* photoelectron spectra of methyl silane, disilane and trisilane and Table V-4 summarizes the results. In the spectrum of silane (see Figure V-1) and methyl silane (Figure V-8) the intense peak at lowest binding energy (107.31 eV for silane and 106.71 eV for methyl silane) corresponds to the adiabatic (ν=0 → ν'=0) Si $2p_{3/2}$ ionization potential. In SiH_4, three vibrational peaks are seen, each separated by 0.295 eV as discussed in Section V-3. The spectrum of methyl silane has an additional three-fold vibrational series superimposed upon each of the three Si-H vibrational peaks; however, the symmetric stretch of the Si-H bonds still dominate the spectrum. The additional vibrational manifold corresponds to ν'=1,2,3 for the totally symmetric stretching frequency of the Si-C bond in the ion and has an energy

Figure V-8. (Top) Spectrum of methyl silane. The three long vertical lines mark the position of the Si-H vibrational states corresponding to ν'=0, 1 and 2 (see text). The three sets of three short vertical lines mark the Si-C vibrational states and overtones. (Middle) Spectrum of Disilane. (Bottom) Trisilane; here the central silicon atom is fit only to a broad doublet.

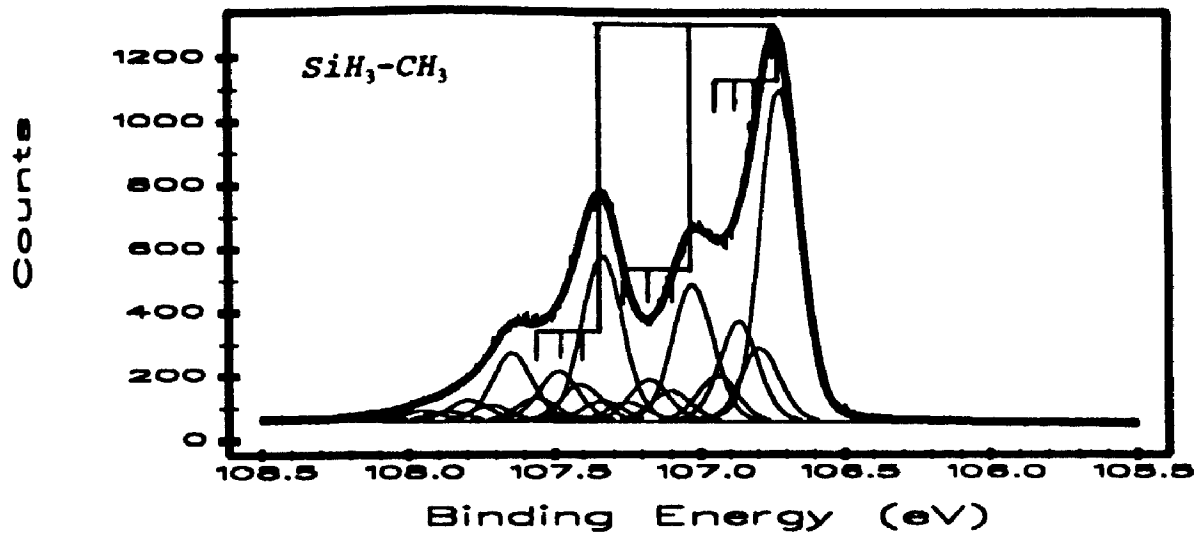
SiH_3-CH_3
Counts
1200
1000
800
600
400
200
0
108.5
108.0
107.5
107.0
106.5
106.0
105.5
Binding Energy (eV)

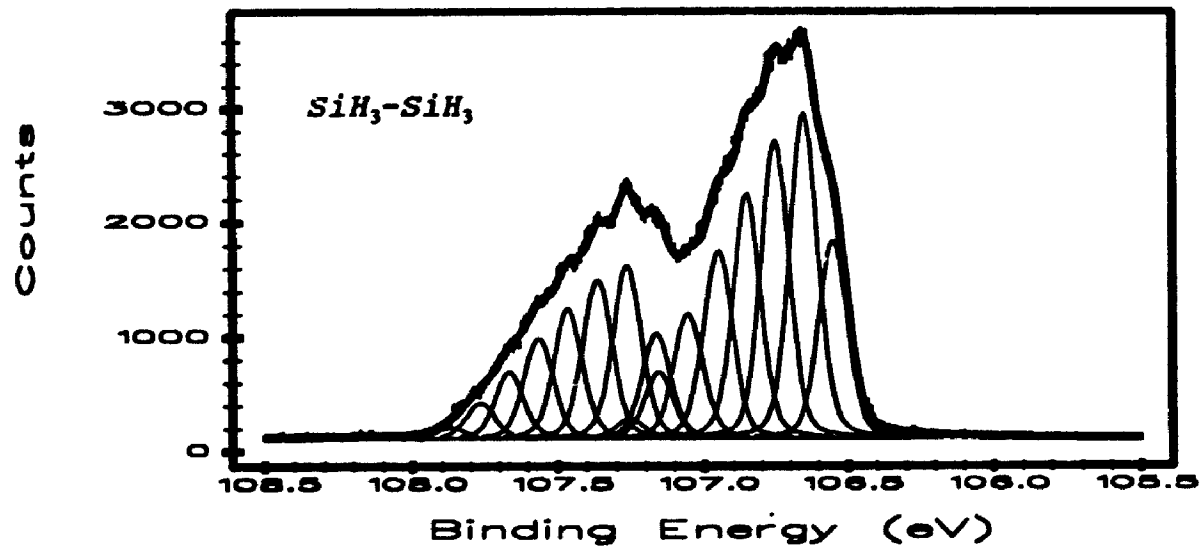
SiH_3-SiH_3
Counts
3000
2000
1000
0
108.5
108.0
107.5
107.0
106.5
106.0
105.5
Binding Energy (eV)

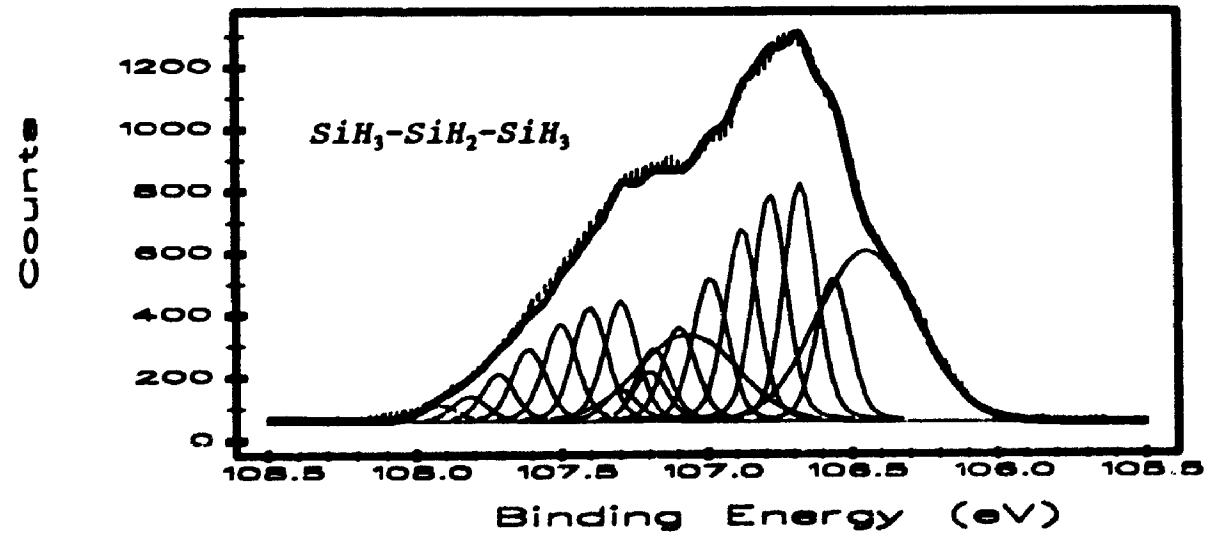
SiH_3-SiH_2-SiH_3
Counts
1200
1000
800
600
400
200
0
108.5
108.0
107.5
107.0
106.5
106.0
105.5
Binding Energy (eV)

separation of 0.075 eV which is only slightly lower than the core-equivalent stretching frequency (676.5 cm^{-1} or 0.084 eV) in the molecule CH_3-PH_2[23]. Only the first three Si-C vibrations are included in this fit because (as in the case of the hydrogen/deuterium series) the higher vibrational states likely have insignificant intensity. The three long vertical lines in Figure V-8 (Top) mark the position of the Si-H vibrational states corresponding to ν'= 0, 1 and 2. The ν'=2 state is very weak and falls directly underneath the the first spin-orbit peak. In the same figure the three sets of three small vertical lines mark the position of the Si-C vibrations and overtones.

Table V-4. Si 2*p* binding energy, ion state vibrational frequency, linewidth and Frank-Condon factors for Methyl silane, Disilane and Trisilane.

Molecule	B.E. (eV)	Type of Vib.	Linewidth (meV)	Vib.Freq. (meV)	Frank-Condon Factors
CH_3SiH_3	106.71	Si-H(ss)	160	305(10)	69.0:26.2:4.8
		Si-C(ss)	160	75(10)	55.2:26.0:13.8:5.0
Si_2H_6	106.56	Si-H(ab)	128	102(5)	15.2:23.5:20.2:16.7: 12.3:7.7:3.9:0.5
Si_3H_8	106.56[a]	Si-H(ab)	135	104(5)	12.8:21.3:20.3:17.2: 12.8:8.4:4.4:2.8
	106.25[b]	-	401	-	

ss=symmetric stretch; ab=asymmetric bending mode
(a) Position of the first Si-H vibration in the two terminal silicons.
(b) Approximate position of the ν'=0 vibrational mode for the central silicon in trisilane

This spectrum differs from previously published spectrum of ethyl silane[6] insofar that the Si-C vibrations are fit to a symmetric envelope (as discussed in Section V-4 for the case of TMS) as opposed to an asymmetric envelope proposed by Bozek[6] *et al.*

If the Si 2*p* ionization of disilane were to excite the totally symmetric stretching frequencies in this molecule one would expect a spectrum very similar to that of methyl silane with the Si-Si stretching frequency approximately equal to that of the core-equivalent species, silyl phosphine ($H_3Si\text{-}PH_2$), namely 0.056 eV (452 cm^{-1})[23]. Qualitatively it is immediately apparent that this is not the case. It is apparent (especially on the $p_{1/2}$ peak at ~107.3 eV) that there exists distinct fine structure with an energy spacing of approximately 0.1 eV. Attempts to deconvolute the spectrum of disilane with even small contributions (less than 10 %) from the symmetric stretching frequencies of Si-H and Si-Si resulted in a substantially higher chi-squared value for the fit.

By far the best fit (shown in Figure V-8) results from using a single vibrational progression corresponding to ν'=0-7 with an energy spacing of 0.102 eV (823 cm^{-1}). This is exactly the same vibrational frequency observed in the photoabsorption spectrum of disilane[24] which is presented in Chapter III. From the infrared spectra of disilane[25,26] this frequency would correspond most closely to that of the asymmetric Si-H bending mode at 844 cm^{-1}. The reason the fine structure is more evident on the $p_{1/2}$ peak is because the last two vibrations in the $p_{3/2}$ series overlap exactly with the first two vibrations in the $p_{1/2}$ vibrational manifold thereby boosting their apparent intensity.

Although this is the first example of a core-level photoelectron spectrum exhibiting a vibrational frequency in the ion that is less than

that of the neutral molecule it is in accord with the C 1s photoabsorption spectrum of ethane reported by Ma et al[22]. Although it is not fully discussed in the original paper it is obvious from their data (Figure # 9, page 1857 in reference 22) that there are two vibrational progressions in the photoabsorption spectrum of ethane. Peaks 1 and 3 correspond to the totally symmetric stretching mode (not observed in disilane) while peaks 2 and 4 exhibit a frequency of 0.16 eV (1290 cm^{-1}); slightly less than the C-H bending mode in ethane[25] (1379 cm^{-1}). The results for ethane-d_6 show a similar trend[22,26] (Table V-5). Thus, ethane, ethane-d_6 and disilane all exhibit excitation of the same non-totally symmetric vibrational mode upon ionization of core electrons; however, in disilane the totally symmetric vibration is not observed in either the photoelectron or the photoabsorption spectrum.

Table V-5. Infrared vibrational frequencies for the neutral molecules ethane, ethane-d_6 and disilane.

Molecule	M-H bending Freq.[a]	Vib. Freq. of Ion[b]
CH_3-CH_3	1379 cm^{-1}	1290 cm^{-1}
CD_3-CD_3	1077 cm^{-1}	1048 cm^{-1}
SiH_3-SiH_3	844 cm^{-1}	827 cm^{-1}

(a) Observed infrared bending mode of a_{2u} symmetry where M= C or Si Data taken from ref.#27

(b) Observed vibrational frequency in the core hole ion state; frequencies for ethane and ethane-d_6 were calculated from data presented in ref. # 23.

The spectrum of trisilane (SiH_3-SiH_2-SiH_3) is less well resolved than that of disilane because of the presence of two different types of silicon atoms in this compound. The central silicon (Si_C) has a vertical binding energy that is ~0.30 eV lower than that of the two terminal silicons (Si_T). As a result the Si $2p_{1/2}$ band from the Si_C atom fills in the valley between the $2p_{3/2}$ and the $2p_{1/2}$ peaks of the two Si_T atoms which have a vibrational manifold almost identical to that of disilane. The peaks resulting from the Si_C atom have been fit only to a simple spin-orbit doublet to avoid confusion with the rest of the spectrum. The ratio of the areas of the two sets of peaks (Area(Si_T)/Area(Si_C) = 1.89) is close to the stoichiometric ratio of 2. The linewidth, lineshape and peak area of the doublet corresponding to the Si_C silicon has been determined from the spectrum of bis trimethylsilyl silane (BTMS, $[Si(CH_3)_3]$-SiH_2-$[Si(CH_3)_3]$) shown in Section V-7.

The spectra of other compounds that have equivalent cores have been recorded but no direct evidence of the asymmetric bending mode in these molecules is observed, although it is likely that this mode dominates the spectrum. Figure V-9 shows the Si 2*p* photoelectron spectra of hexamethyl disilane (HMDS, $Si(CH_3)_3$-$Si(CH_3)_3$), dodecamethyl cyclohexasilane (DMCS, $[-Si(CH_3)_2-]_6$) and tetrakis trimethylsilyl germane (TKTG, $Ge[Si(CH_3)_3]_4$); data for these three compounds are shown in Table V-6. The Si-C bending vibration (<653 cm^{-1}) is too small to resolve and, although broader, the lineshape has not changed substantially from that of TMS. Given that there is no direct evidence to support the presence of bending vibrational modes in these molecules, their spectra have been fit to a simple spin-orbit doublet. Although bending vibrational modes cannot be resolved in these compounds their presence should be strongly considered, especially in the

Figure V-9. Si 2*p* photoelectron spectra of $Si(CH_3)_3$-$Si(CH_3)_3$ (top), $Si_6(CH_3)_{12}$ (Middle` and $Ge[Si(CH_3)_3]_4$ (Bottom). No evidence of vibronic coupling can be observed (see text).

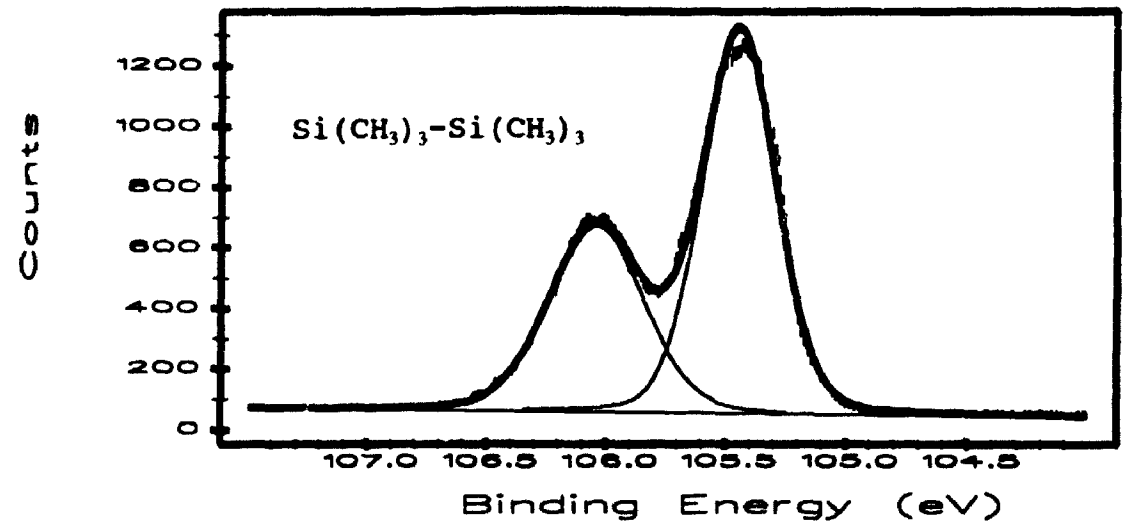
Counts
1200
1000
800
600
400
200
0
$Si(CH_3)_3$-$Si(CH_3)_3$
107.0 106.5 106.0 105.5 105.0 104.5
Binding Energy (eV)

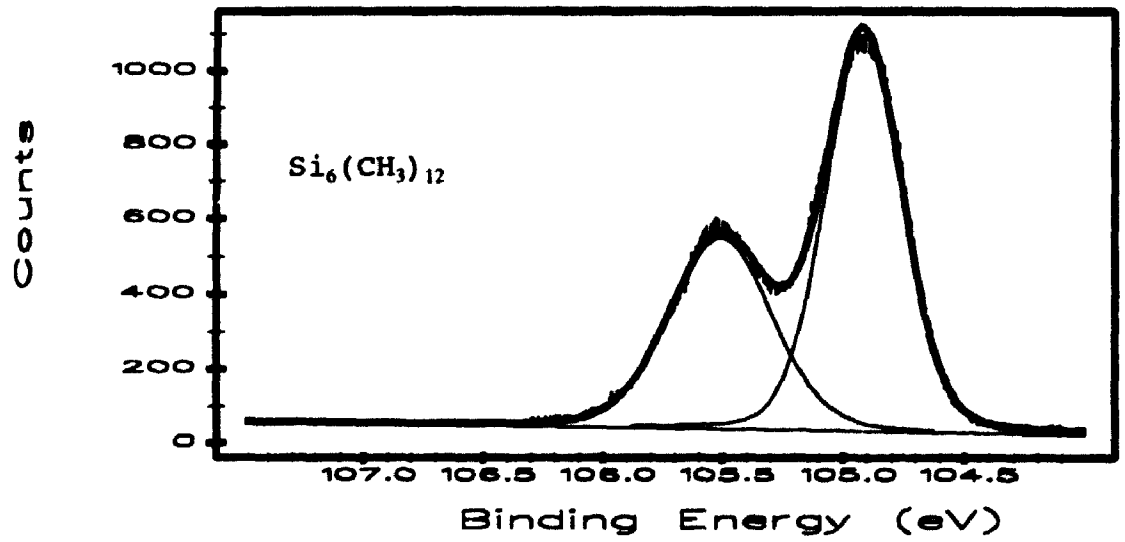
Counts
1000
800
600
400
200
0
$Si_6(CH_3)_{12}$
107.0 106.5 106.0 105.5 105.0 104.5
Binding Energy (eV)

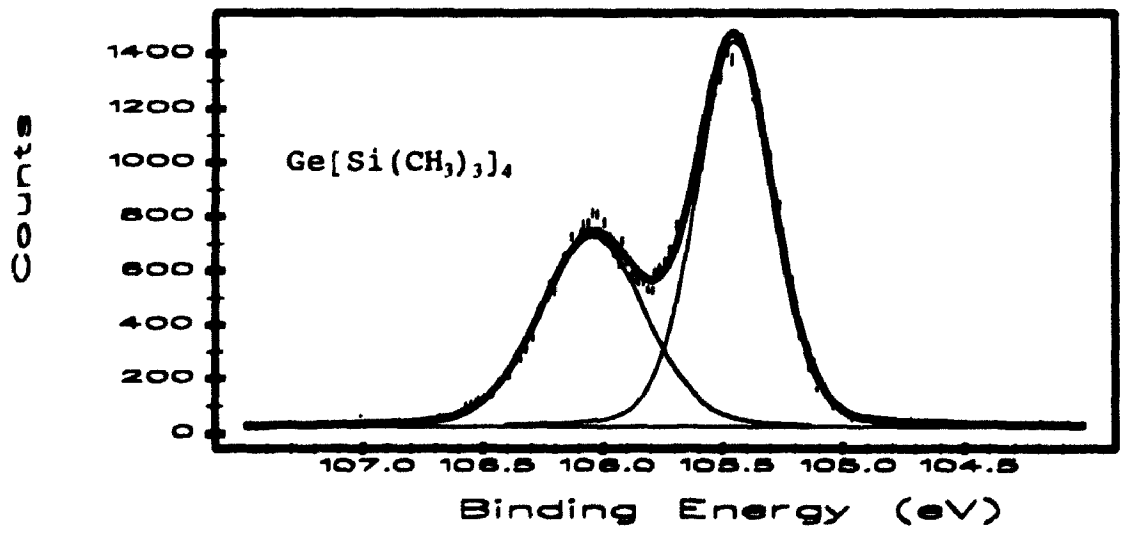
Counts
1400
1200
1000
800
600
400
200
0
$Ge[Si(CH_3)_3]_4$
107.0 106.5 106.0 105.5 105.0 104.5
Binding Energy (eV)

case of HMDS whose structure is very similar to that of disilane. The implications of this will effect the interpretation of photoelectron spectra of all equivalent core systems such as polymers and surfaces.

Table V-6. Linewidths, vertical binding energy and adiabatic B.E. for the three compounds $Si_2(CH_3)_6$, $Ge[Si(CH_3)_3]_4$ and $Si_6(CH_3)_{12}$ (Figure V-9). Linewidths are accurate to within ±10 meV.

Molecule	Line Width (meV)	Vertical B.E. (eV)	Adiabatic B.E. (eV)
$Si(CH_3)_3$-$Si(CH_3)_3$	412	105.44(1)	105.15(5)
$Ge[Si(CH_3)_3]_4$	445	105.45(1)	105.16(5)
$Si_6(CH_3)_{12}$	448	104.91(1)	104.62(5)

Section V-7; Model Compounds For Hydrogen Adsorbed on a Silicon Surface.

In the case of hydrogen adsorbed on a silicon surface the vibrational frequencies of both Si-H and Si-D have been measured by high resolution electron energy loss spectroscopy[27] (HREELS) but, the effects of ion state vibrational splitting in the Si 2*p* surface photoelectron measurements have been completely ignored[28,29] as has vibrational splitting on metal core-levels in general. For example, Ley[30] et al reported the Si 2*p* photoelectron spectra of H adsorbed on an amorphous silicon surface and fit the experimental data to four spin-orbit doublets corresponding to those silicon atoms which have 0, 1, 2 or 3 hydrogens bonded to them. Each doublet was chemically shifted by 0.335 eV per hydrogen relative to the unhydrogenated bulk silicon. However, from Section V-3 above, the high resolution spectra of SiH_4 shows intense Si-H vibrational structure with a vibrational splitting of 0.295 eV. The similarity of this *vibrational splitting* with Ley's *chemical shift*, combined with the relatively broad unresolved solid state spectra[30] prompted the investigation of the nature of the chemical shift that results from replacing Si-Si bonds with Si-H bonds. This section presents the Si 2*p* photoelectron spectra of four model compounds, $H_xSi[Si(CH_3)_3]_{4-x}$ (x=0,1,2,3) which mimic the chemical shifts resulting from 0, 1, 2 and 3 hydrogens bonded to a silicon surface.

The central silicon atom in $Si[Si(CH_3)_3]_4$ (TKTS) is in a four coordinate chemical environment which models that of bulk silicon. By successively removing one of the trimethyl silyl groups $[-Si(CH_3)_3]$ and replacing it with a hydrogen atom one can create model compounds that

correspond to one, two, or three hydrogens bonded to a silicon surface. Figure V-10 shows the Si 2*p* spectra of all four model compounds, the binding energies and linewidths of which are listed in Table V-7.

Table V-7. Chemical shifts of the Si_C and the Si_{TMS} silicons in the model compounds (Figure V-10). The chemical shift is 0.3 eV per hydrogen.

Compound	(Atom)	Linewidth (meV)	Vertical B.E.(eV)	Adiabatic B.E. (eV)	Chemical Shift(eV)
$Si[Si(CH_3)_3]_4$	(C)	414(10)	104.30(1)	104.00(5)	0.00
	(TMS)	415(10)	105.45(1)	105.15(5)	0.00
$HSi[Si(CH_3)_3]_3$	(C)	376(10)	104.61(2)	104.31(5)	0.31
	(TMS)	394(10)	105.46(1)	105.46(5)	0.01
$H_2Si[Si(CH_3)_3]_2$	(C)	397(10)	104.91(2)	104.61(5)	0.61
	(TMS)	425(10)	105.44(1)	105.44(5)	-0.01
$H_3Si[Si(CH_3)_3]$	(C)	398(10)	105.21(2)	104.91(5)	0.91
	(TMS)	448(10)	105.45(2)	105.15(5)	0.00

There are several general observations. First two rather broad doublets are observed in each spectrum corresponding to the trimethylsilyl silicons (Si_{TMS}, the large doublet at high binding energy - ~105.45 eV) and the central silicons (Si_C, the smaller doublet at low binding energy). The large line widths are similar to those observed for $Si(CH_3)_4$ or $Si_2(CH_3)_6$ and are due to unresolved vibrational splitting. As is the case with the spectra of the large methylated silanes shown in Figure V-9, there is no direct evidence of vibrational modes. Neither the totally symmetric nor

Figure V-10: Si 2*p* Photoelectron spectra of (a) TKTS, (b) TTMS, (c) BTMS and (d) TMDS.

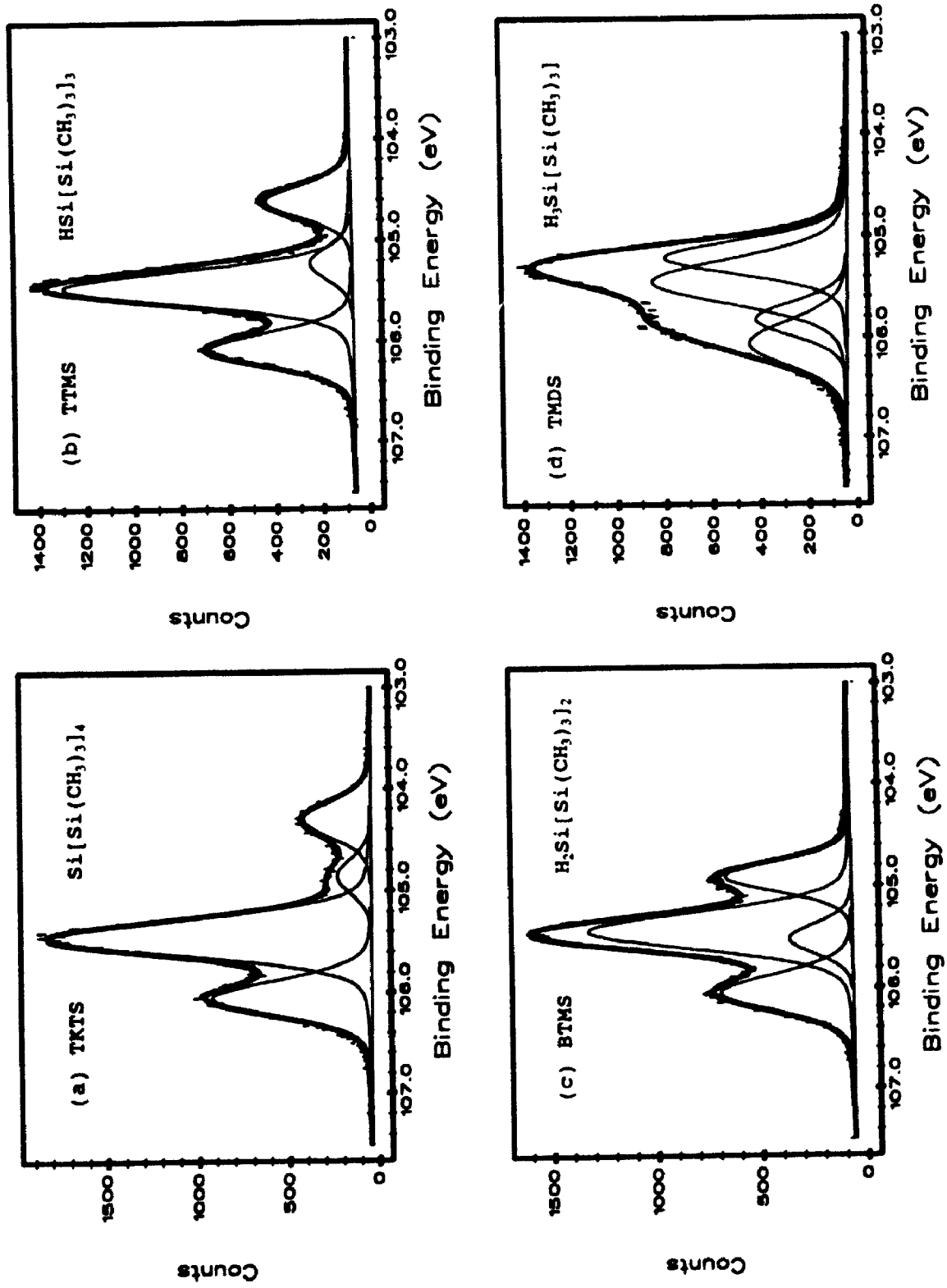
(a) TKTS
Si[Si(CH3)3]4
(b) TTMS
HSi[Si(CH3)3]3
(c) BTMS
H2Si[Si(CH3)3]2
(d) TMDS
H3Si[Si(CH3)3]
Counts
Binding Energy (eV)

asymmetric vibrations are resolved though it is probable that both are present. In the face of this ambiguity each spectrum in Figure V-10 has been fit to a pair of spin-orbit doublets. Secondly, the area ratio of the two doublets [$A(Si_{TMS})/A(Si_C)$] is close to the stoichiometric ratio in all four compounds. Thirdly, the ionization potential of the Si_{TMS} silicons in each compound is within 0.01 eV while the binding energy of the central silicon atom, Si_C, shows a chemical shift of approximately 0.30 eV per hydrogen (see Table V-7) toward higher binding energy. These values are in reasonable agreement with those reported by Ley[30] *et al* for the photoelectron spectrum of hydrogen adsorbed on a silicon surface.

When the preliminary results were first reported[4] it was suggested that the broadness of Ley's[30] photoelectron spectrum may be due to excitation of the symmetric Si-H vibrational mode rather than a simple chemical shift effect. Recently Dumas *et al.*[31] have observed the excitation of the Si-H symmetric stretching frequency as well as the asymmetric bending mode in the photoelectron spectra of ideally H-terminated Si (111) surfaces. Although their values are not identical to ours this observation further emphasizes the importance and usefulness of gas-phase measurements.

Section V-8;

Applications To The C 1s Spectra of Small Molecules and Polymers.

As mentioned in Section V-1, core-level vibrational structure was resolved[1] on the C 1s level of CH_4 at a resolution of ~0.4 eV and then, latter, at a resolution of better than 0.3 eV. There is much evidence from gas-phase[1,32,33] and polymer[10,33] studies at resolutions between 0.25 and 0.4 eV that the broad C 1*s* widths of between ~0.6 and 0.9 eV are due to vibrational broadening. Specifically, at 0.40 eV resolution, the linewidths of the C 1s spectra of CH_4 and the four carbons in CF_3-COO-CH_2-CH_3[32] are 0.7 eV and ~0.8 eV respectively, and the linewidths in formic acid and substituted formic acids are all between 0.6 and 0.9 eV[33]. Furthermore, Beamson[10] *et al* recently reported the C 1s spectrum of polymers such as polyethylene, polypropylene and polystyrene at an instrumental resolution of 0.25 eV with total linewidths of between 0.77 and 0.85 eV. These spectra were fit to a totally symmetric C-H vibrational progression similar to that seen in CH_4 - three peaks with an energy spacing of 0.39 eV and a linewidth of 0.64 eV. Because the C 1s inherent linewidth is between 0.06 and 0.13 eV[1,34], all of the reported linewidths must be due to unresolved vibrational excitations.

Because of the narrow C 1s width it should soon be possible to record C 1s photoelectron spectra with total linewidths of ~0.1 eV using monochromatized synchrotron radiation. Until that time, it may be helpful to use the Si 2*p* vibrational splittings to rationalize and predict C 1*s* linewidths and vibrational manifolds in the analogous carbon compounds.

Two assumptions have to be made: The first assumption is that the vibrational manifolds for C and Si analogs are very similar. Secondly, if the vibrational manifolds are the same, then the total linewidth of the C 1s envelope at high resolution (~0.1 eV) will be directly related to the total linewidth of the Si 2*p* analog by the ratio of the vibrational frequencies as shown in Equation V-3.

$$\Gamma_C = [\nu(C)/\nu(Si)]\ \Gamma_{Si} \qquad \text{[Eq. V-3]}$$

where Γ_C and Γ_{Si} are the total linewidths for the C 1*s* and Si 2*p* envelopes respectively, and $\nu(C)$ and $\nu(Si)$ are the vibrational frequencies for the carbon molecule and its analogous silicon compound.

Certainly the first assumption is justified by the almost identical vibrational patterns in CH_4 and SiH_4[1,3,6] and by the similar changes in the bond length of the parent compound (CH_4 or SiH_4) and its corresponding core-equivalent, NH_3 or PH_3 respectively (Table 2). However, the *difference* in bond length between Si/P and C/N analogs are not generally similar (Table 2). These differences are probably due to the fact that the P and N analogs, because of their different geometry, are not good core-equivalents.

To illustrate the procedure consider SiF_4 and CF_4. Using the Si 2*p* linewidth of ~0.5 eV and the ratio of core-equivalent frequencies for the molecules SiF_4 and CF_4 (or the ion state frequencies where available, see Table V-2) the expected C 1*s* linewidth for CF_4 should be ~0.61 eV. CF_3 groups in molecules such as CF_3-COO-CH_2-CH_3 should have similar widths because substitution of a single F by another group with a similar vibrational frequency does not substantially change the overall linewidth.

Similarly for the polyethylene spectra[10]; given the photoelectron

results of disilane and trisilane presented in this chapter, and the C 1s photoabsorption results of Ma *et al*[20-22] it seems very possible that the polymer spectrum reported by Beamson[10] *et al* results from the excitation of many asymmetric C-H bending modes each with a much narrower linewidth then the 0.64 eV width required for the symmetric stretching modes reported. If the C-H vibrational envelope in polyethylene is similar to that of disilane or trisilane then given the frequency ratio of 1290/827 for the C-H and Si-H bending vibrations, and the SiH_3-SiH_3 linewidth of ~0.5 eV, the linewidth expected for polyethylene should be approximately 0.78 eV. This is very close to the value of 0.77 eV reported by Beamson *et al*[10].

Finally, on moving across the periodic table through the ligands C, N, O and F the C 1*s* linewidths should increase from ~0.5 to ~0.8 eV. This same trend is observed for the Si 2*p* linewidths but the increased vibrational frequency in the carbon analogs will cause the spectra to be even broader.

Section V-9; Conclusions.

At a resolution of ~0.1 eV the vibrational manifold of SiH_4 has been resolved and, for the first time, the vibrational isotope effect in the core-level photoelectron spectroscopy has been demonstrated. Also, the effect of vibrational overtones in the spectra of SiH_3D, SiH_2D_2 and $SiHD_3$ were investigated. In the spectra of the mixed hydrogen/deuterium compounds, vibrational states corresponding to $v'>1$ are sharply attenuated when compared with the same states in either SiH_4 or SiD_4. This phenomenon is likely a general feature of all photoelectron spectra; if this were not the case the spectrum of compounds such as dimethyl dimethoxy silane would have linewidths much larger than those observed.

From the spectra of the methyl/methoxy and the methyl/dimethyl amino series it was shown that the linewidth increases linearly with respect to the number of methoxy or dimethyl amino groups. The greater linewidth in the methoxy compounds is indicative of a larger vibrational manifold for the Si-O bonds than for those of Si-C or Si-N. This establishes a trend for the light elements in the number of vibrational states that are populated upon Si 2*p* ionization (the number of vibrations is shown in parenthesis): H(3); D(+); C(7); N(>7,<10); O(10); F(11). The large vibrational manifolds can cause the vertical and adiabatic binding energies to differ by as much as 0.5 eV. Because this difference will not be the same for each molecule, even relative binding energies cannot be measured accurately without vibrational resolution.

The presence of equivalent cores in small molecules results in core

hole localization in the ion state. This in turn leads to coupling between electronic and non-totally symmetric vibrational modes that would otherwise be symmetry-forbidden. The large number of vibrations that are excited in the spectrum of disilane may have important implications for the study of other equivalent core systems such as polymers and surfaces.

The chemical shift (as measured by the change in vertical binding energy) that results from replacing a Si-Si bond with a Si-H bond is 0.3 eV per hydrogen. Although this is essentially identical to the symmetric Si-H stretching vibrational frequency (0.295 eV) the latter is not likely going to be observed in surface photoelectron work as a result of the equivalent cores as mentioned above.

In the C 1*s* spectra of organic molecules and polymers much higher resolution is needed to resolve the vibrational structure in a wider variety of compounds for comparison with the Si 2*p* photoelectron spectra already reported. The Si 2*p* linewidths should be very useful in predicting C1*s* linewidths in general, and particularly in the case of surfaces and polymers where it will probably not be possible to resolve vibrational structure.

Because of the very narrow Si 2*p* inherent linewidths, even better resolution should be achievable in the near future with monochromatized synchrotron radiation. At total linewidths of ~50 meV it should be possible to resolve much more of the vibrational structure that is suggested by the broad linewidths of compounds such as $Si(OCH_3)_4$, as well as other molecules with even smaller vibrational frequencies.

No evidence has been observed for ligand field splitting, which should split the $2p_{3/2}$ level but not the $2p_{1/2}$ level in the non-tetrahedral molecules such as CH_3-SiH_3, Si_2H_6 and CH_3SiCl_3[6,35]. Indeed, the equivalent fits to the $2p_{3/2}$ and $2p_{1/2}$ lines give excellent fits in all cases

indicating that any ligand field splitting that may be present is less than 50 meV in these compounds. Ligand field splitting[36] has been observed on Si surfaces, but this report[37] is currently the subject of controversy and thus the issue of ligand field splitting on Si surfaces has not yet been resolved in the literature. A good gas-phase model to study this might be SiH_3F; however, this compound is not commercially available and hence its spectra has never been recorded.

Finally, shortly after the original publication of this work,[38] Dumas *et al.* reported the observation of both the symmetric and asymmetric Si-H vibrational modes in the Si 2*p* photoelectron spectrum of an ideally H-terminated Si surface.[39]

Section V-10; References.

1) (a) U. Gelius, S. Svensson, H. Siegbahn, E. Basilier, A. Faxläv and K. Siegbahn; Chem. Phys. Lett., **28**, 1, (1974).

(b) U. Gelius, L. Asplund, E. Basilier, K. Helenelund and K. Siegbahn; Nuc. Instr. Methods, **B229**, 85 (1984)

2) J.H.D. Eland, *Photoelectron Spectroscopy*, John Wiley and Sons, New York, 1974

3) J.D. Bozek, G.M. Bancroft, J.N. Cutler and K.H. Tan; Phys. Rev. Lett., **65**, 2757, (1990).

4) D.G.J. Sutherland, G.M. Bancroft and K.H. Tan; Surf. Sci. Lett., **262**, L96, (1992)

5) Z.F. Lui, G.M. Bancroft, J.N. Cutler, D.G.J. Sutherland, and K.H. Tan; Phys. Rev. A, In press

6) J.D. Bozek, G.M. Bancroft and K.H. Tan, Phys. Rev. A, **43**, 3597, (1991)

7) For the purpose of this chapter we shall define the term "core-equivalent" as a molecule in which the core-ionized atom, with nuclear charge Z, is replaced by an atom with nuclear charge Z+1. For instance, PH_3 would be the core-equivalent of SiH_4^+ because the screening of the nuclear charge due to core electrons would be approximately the same in each case. Although confusing, the precedent is already established in the literature[21-23] to use the term "equivalent cores" to describe molecules such as disilane (SiH_3-SiH_3) which, from symmetry considerations, have silicon cores in equivalent geometric positions; these types of molecules yield photoelectron spectra with unique characteristics. We will use these

two terms precisely as written above (*core-equivalent* or *equivalent core*) to express their assigned definitions.

8) J.N. Cutler, G.M Bancroft and K.H. Tan, J. Phys B, **24**, 4897, (1991)

9) (a) W. Domcke and L.S. Cederbaum; Chem. Phys. **25**, 189, (1977).

(b) L.S. Cederbaum and W. Domcke; J. Chem. Phys. **66**, 5084, (1977).

10) G. Beamson, D.T. Clark, J. Kendrick and D. Briggs; J. Elec. Spec., **57**, 79, (1991)

11) H.Gilman and C.L.Smith, J. Organomet. Chem., **14**, 91, (1968)

12) A.G. Brook, F. Abdesaken and H. Söllradl; J. Organomet. Chem., **299**, 9, (1986)

13) J.D.Bozek, J.N.Cutler, G.M.Bancroft, L.L.Coatsworth, K.H.Tan, D.S.Yang and R.G.Cavell, Chem. Phys. Lett., **165**, 1, (1990).

14) Z.F. Lui, J.S. Tse and G.M. Bancroft; To be published

15) J.H. Meal and M.K. Wilson, J. Chem. Phys., **24**, 385, (1956)

16) L.C. Thomas; *Interpretation of The Infrared Spectra of Organophosphorous Compounds*; Heyden and Son; London; 1974; Pgs. 52, 125

17) (a) E.Z. Chelkowska and F.P. Larkins, J. Phys. B, **24**, 5083, (1991)

(b) J. McColl and F.P. Larkins, Chem. Phys. Lett.; In Press.

18) J.N. Cutler, G.M. Bancroft, D.G.J. Sutherland and K.H. Tan, Phys. Rev. Lett., **67**, 1531, (1991).

19) P. Kelve, B.Blomster, H. Siegbahn, and K. Siegbahn; Phys. Scrip., **21**, 75, (1980) and references therein

20) Y. Ma, F. Sette, G. Meigs, S. Modesti and C.T. Chen; Phys. Rev. Lett., **63**, 2044, (1989).

21) F.X. Gadea, H. Köppel, J. Schirmer, L.S. Cederbaum, K.J. Randall, A.M. Bradshaw, Y. Ma, F. Sette, and C.T. Chen; Phys. Rev. Lett., **66**, 883, (1991).

22) Y. Ma, C.T. Chen, G. Meigs, K.J. Randall, and F. Sette; Phys. Rev. A, 44(3), 1848, (1991).

23) H.R. Linton and E.R. Nixon; Spectro. Chim. Acta, 146, (1959)

24) D.G.J. Sutherland, G.M. Bancroft, J.D. Bozek and K.H. Tan; Chem. Phys. Lett.; In Press.

25) H.S. Gutowsky and E.O. Stejskal; J. Chem. Phys., 22, 939, (1954)

26) G.W. Behtke and M.K. Wilson; J. Chem. Phys., 26, 1107, (1957)

27) H. Wagner, R. Butz, U. Backes and D. Bruchmann, Solid State Comm. 38, 1155, (1981)

28) H. Fröitzheim, H. Ibach and S. Lehwald, Phys. Lett., 55A, 247, (1975).

29) P. Guyot-Sionnest, P. Dumas, Y.J. Chabal and G.S. Higashi, phys. Rev. Lett., 64, 2156, (1990).

30) L. Ley, J. Reichardt and R.L. Johnson, Phys. Rev. Lett., 49, 1664, (1982).

31) P. Dumas *et al.;* Unpublished work.

32) U. Gelius, E. Basilier, S. Svensson, T. Bergmark and K. Siegbahn; J. Elec. Spect., 2, 405, (1974).

33) A. Naves de Brito M.P. Keane, N. Correia, S. Svensson, U. Gelius and B.J. Lindberg; Surf Int. Anal., 17, 94, (1991).

34) M.O. Krause; J. Phys. Chem. Ref. Data, 8, 307, (1979)

35) G.M. Bancroft and J.S. Tse; Comm. Inorg. Chem., 5, 89, (1986) and references therein.

36) J.N. Cutler, G.M. Bancroft and K.H. Tan; J. Chem. Phys., 97(11), 7932, (1992).

37) G.K. Werteim, D.M. Riffe, J.E. Rowe and P.H. Citron; Phys. Rev. Lett., 67, (1991), 120

38) D.G.J. Sutherland, G.M Bancroft and K.H. Tan; J. Chem. Phy., 97, 7918,

(1992)

39) P. Dumas *et al.*; *Proceedings of The Tenth International Conference on Vacuum Ultraviolet Radiation Physics*, Paris France, July 27-31, 1992 (In Press)

CHAPTER VI

The Valence Band Photoelectron Spectra of Si Clusters

Section VI-1; Introduction.

From an industrial point of view it is arguable that the most important group in the periodic table is group IV containing the elements C, Si, Ge, Sn and Pb. Although the latter two elements are, perhaps, of lesser importance, the significance of carbon chemistry is self-evident and the world-wide proliferation of the electronics industry over the last twenty years has shifted considerable attention to the chemistry of Si and Ge[1-5]. In this chapter the valence band photoelectron spectra of five cluster-type compounds of group IV elements are presented: tetramethyl silane (TMS, $Si(CH_3)_4$); hexamethyl disilane (HMDS, $Si_2(CH_3)_6$); tetrakis trimethylsilyl silane (TKTS, $Si[Si(CH_3)_3]_4$); tetrakis trimethylsilyl germane (TKTG, $Ge[Si(CH_3)_3]_4$); and the cyclic compound, dodecamethyl cyclohexasilane (DCHS, $[Si(CH_3)_2]_6$). The spectra of each compound was recorded at four different photon energies, namely 21.2 eV, 100 eV, 120 eV and 135 eV. These systems are of importance both because of their intrinsic molecular interest and because molecules such as these mimic local sites in tetrahedral group IV semi-conductors.

The valence band photoelectron spectra of TMS has been reported before[2,4,5] and the Si 2*p* core-level photoelectron spectra of all five compounds have recently been reported by Sutherland[6] *et al.* (see Chapter V, Section V-7), however, to date no documentation of the valence band photoelectron spectra of the other four compounds exists.

Section VI-2; Experimental.

Tetramethyl silane (TMS, $Si(CH_3)_4$); Hexamethyl disilane (HMDS, $Si_2(CH_3)_6$); and Tetrakis trimethylsilyl silane (TKTS, $Si[Si(CH_3)_3]_4$) were purchased commercially in high purity from The Aldrich Chemical Company and used without further purification. Tetrakis trimethylsilyl germane (TKTG, $Ge[Si(CH_3)_3]_4$ was synthesized according to Brook[7] *et al.* and the cyclic compound dodecamethyl cyclohexasilane (DCHS, $[Si(CH_3)_2]_6$) was synthesized according to West[8] *et al.*

In all cases the samples were introduced directly into the gas cell of the spectrometer at pressures of ~ $5X10^{-3}$ torr. Liquid samples (TMS and HMDS) were de-aerated by repeated freeze-pump-thaw cycles to remove any dissolved oxygen or nitrogen. The solid samples (TKTS, TKTG and DCHS) were heated to approximately 65°C to increase their vapor pressure. Constant sample pressure was maintained for the time required to accumulate the data for each spectrum.

For each compound, spectra were recorded at four different photon energies: 21.2, 100, 120 and 135 eV. The photoelectron spectrometer used to record the three higher energy spectra has been described in detail elsewhere[9] (see Chapter II, Section II-4). Briefly, the spectrometer consists of a McPherson 36 cm mean radius electron energy analyzer with 1mm entrance and exit slits resulting in a theoretical electron resolution, $\Delta E/E$, of 1/720. For electron kinetic energies of ~100 eV the theoretical value of ΔE is ~0.14 eV. Assorted differential pumping was used on the spectrometer and beamline to isolate the high pressure of the gas cell from

the optical components of the beamline.

All of the higher energy spectra were recorded using the CSRF Mark IV Grasshopper monochromator at the Aladdin synchrotron of the University of Wisconsin at Madison. An 1800 groove/mm grating was employed in the monochromator resulting in a minimum *practical* photon resolution of 0.08 eV at 100 eV photon energy (see Chapter II, Section II-1).

The five spectra taken with a photon energy of 21.2 eV were recorded using a commercial McPherson 36 cm mean radius electron energy analyzer fitted with a He discharge lamp and entrance and exit slits of 0.5 mm. This instrument is described in detail elsewhere[10] (see Chapter II, Section II-4).

The binding energy of each compound was measured through the use of an internal calibrant, namely the $3p_{3/2}$ line of argon which has binding energies of 15.759 eV. Although these lines interfere with the spectra itself they are sufficiently sharp by comparison that an accurate calibration can be made.

Section VI-3; Results and Discussion.

Figures VI-1 to VI-5 show the spectra of the five compounds $Si(CH_3)_4$, $Si_2(CH_3)_6$, $Si[Si(CH_3)_3]_4$, $Ge[Si(CH_3)_3]_4$ and $[Si(CH_3)_2]_6$ each at four different photon energies and Tables VI-1 to VI-5 document the pertinent data. Because of the large number of molecular orbitals (MO's) in these compounds the spectra have been fit with the minimum number of peaks needed to reproduce the experimental data; no attempt has been made to fit transitions from each individual orbital. All spectra have been fit in a similar fashion and can be briefly summarized as follows: Peak A at approximately 8 eV (not present in TMS) corresponds to the metal-metal bonding MO and has been fit to a single peak as has peak B at ~10 eV which results from MO's associated with the metal-carbon bonds. The broad feature at ~14 eV is fit to three peaks; the first two (C & D) result from MO's associated, primarily, with the C-H bonds and the third peak, E, results from a metal-carbon/metal-metal bonding orbital. The one exception to the above description is the peak associated with the Si-C MO's in the cyclic compound, DCHS, which has been fit to two peaks (B & B') at approximately 9.2 and 10.4 eV respectively.

From the spectra of these five compounds some qualitative trends are readily apparent. Relative to the carbon-hydrogen MO's (peaks C & D), the cross section of both the metal-carbon (peaks B & E) and the metal-metal MO's (peaks A & E) increase in intensity as the photon energy is increased. Although this is generally true, the cross section of the metal-metal MO's in the Ge compound (peak A; Figure VI-4) increases much less rapidly then

the corresponding peak in any of the Si analogs.

The assignment of the molecular orbitals in the photoelectron spectrum of $Si(CH_3)_4$ (Figure VI-1; Table VI-1) is in agreement with previously reported extended Hückel[5] and ab initio[1,3,11] calculations. Peak B, at lowest binding energy, is assigned to the $3t_2$ silicon-carbon bonding molecular orbital. Peaks C & D result from the carbon-hydrogen bonding orbitals ($2t_2$+ $1e$ + $1t_1$) which are not fully resolved, and peak E, is a second silicon-carbon bonding orbital of a_1 symmetry.

Ms-Xα calculations[13] predict that the $3t_2$ orbital in TMS is composed primarily from the C $2p$ (56%) and the Si $3p$ (26.5%) with a small contribution from the Si $3d$ orbitals. This assessment is in excellent agreement with previous calculations[2] which predict a composition of 57% C $2p$, 25% Si $3p$ and 6% Si $3d$. As the photon energy increases, the intensity of peaks B & E (the Si-C bonding orbitals) increases relative to peaks C & D (the C-H bonding orbitals). From consideration of the C $2p$ and Si $3p$ cross sections,[12] it is seen that the C $2p$ cross section decreases much faster than does that of the Si $3p$. Hence, at higher photon energies, it is the inclusion of the Si $3p$ character in the $3t_2$ (peak B) and $2a_1$ (peak E) orbitals that is responsible for their increased intensity relative to that of peaks C & D.

Figure VI-2 shows the spectra of $Si_2(CH_3)_6$ (HMDS) at four different photon energies and Table VI-2 documents the pertinent data. Peaks B to E behave, qualitatively, the same as they do in the case of TMS (Figure VI-1). However, peak B in Figure VI-2 results from two different molecular orbitals ($7e$ and $8e$; see Table VI-2) and this splitting is evident in the poor fit of this peak in the He I spectrum of this compound. Furthermore, peak E shows a much greater increase at higher photon energies and the relative intensity

of peak A (not present in the spectrum of TMS) increases dramatically as the photon energy is increased from 21.2 to 135 eV. The more pronounced increase in peak E in HMDS compared to TMS is due to the greater Si character in the corresponding MO's (compare Tables VI-1 & VI-2) and the very large increase in peak A is a result of the high percentage of Si 3*p* character in the $7a_1$ orbital.

The spectra of $Si[Si(CH_3)_3]_4$ (TKTS) and $Ge[Si(CH_3)_3]_4$ (TKTG) can be explained in a fashion analogous to that of $Si_2(CH_3)_6$ with two exceptions: First, peak E in TKTG behaves much the same as peak E in the TKTS because the Ge 4*s* electrons from which the corresponding orbital is composed have a cross section that is similar to the Si 3*s* shell that is utilized in TKTS and HMDS (see Tables VI-2, VI-3 and VI-4). Conversely, peak A in TKTG is much smaller due to the lower cross section of the Ge 4*p* electrons compared to the Si 3*p* shell for TKTS and HMDS.

Figure VI-5 shows the spectrum of the cyclic compound, $[-Si(CH_3)_2-]_6$ (DCHS), and Table VI-5 lists the peak positions. No theoretical calculations are available for this compound but it is reasonable to assume that the peaks in Figure VI-5 that are common to the other spectra result from similar molecular orbitals in this compound. The main exception is the peak resulting from the Si-C bonding orbitals which is split into two separate peaks (B & B') in this compound.

The local symmetry of each Si in this compound is C_{2v} whereas, in the other compounds, the central Si is in a tetrahedral environment and the other four silicons are C_{3v}. One would not expect such a large splitting in the energy of the MO's in changing from C_{3v} to C_{2v} symmetry. Furthermore, it is obvious from the peak positions and their relative intensities that B' does indeed result from a splitting of peak B and not peak A. Although

Figure VI-1. Valence band photoelectron spectra of $Si(CH_3)_4$ at photon energies, 21.2, 100, 120 and 135 eV

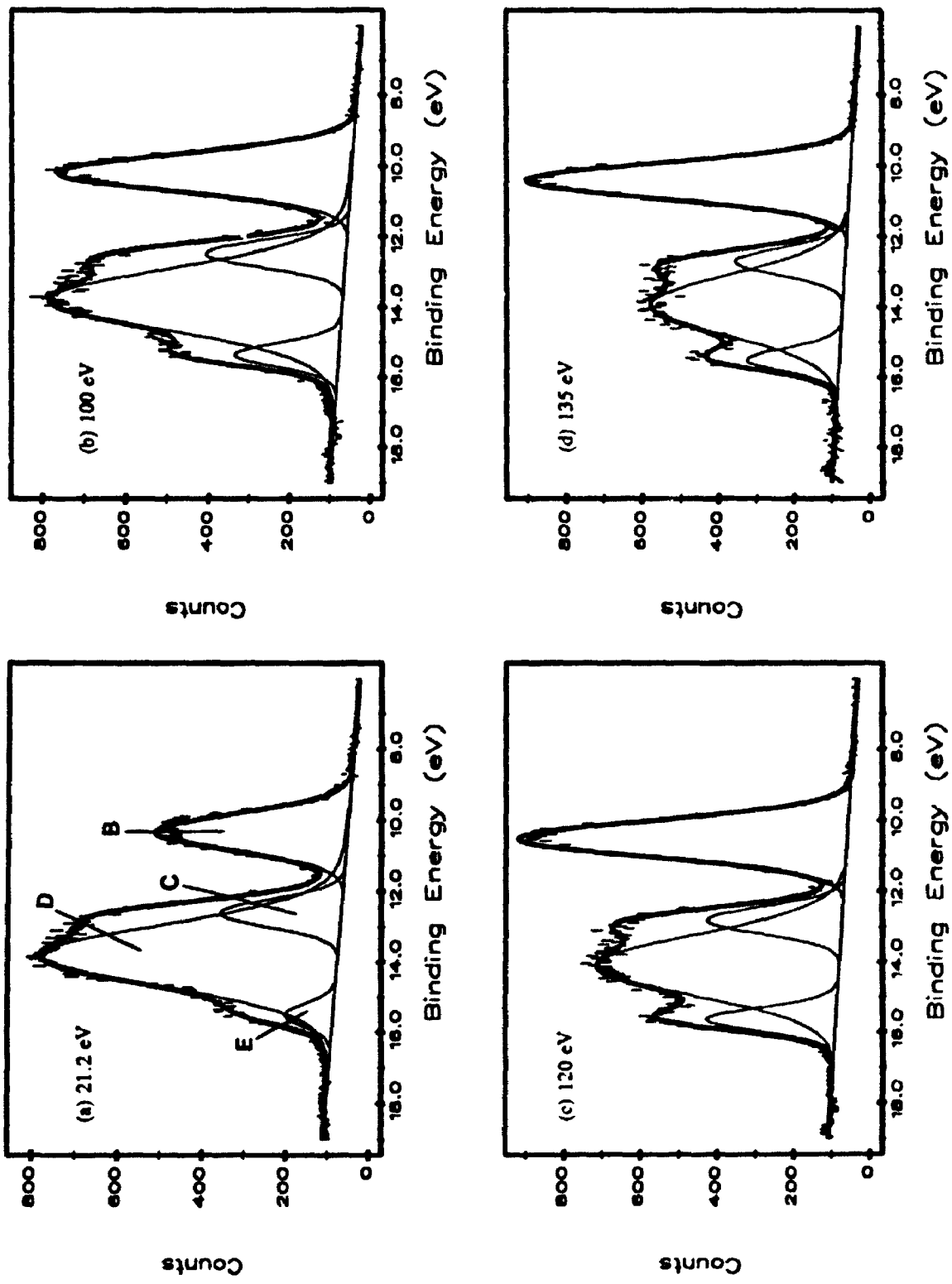
(a) 21.2 eV
(b) 100 eV
(c) 120 eV
(d) 135 eV
B
C
D
E
Counts
Binding Energy (eV)
800
600
400
200
0
18.0
16.0
14.0
12.0
10.0
8.0

Table VI-1. The composition and energy of calculated molecular orbitals (from reference 13) and the corresponding experimental peak and its binding energy in the photoelectron spectrum of $Si(CH_3)_4$ from Figure VI-1.

	Composition (%)		Calculated	Exp. Peak
Calc. MO	Si	C	Energy (eV)	& B.E (eV)
$1a_1$	13.7 *s*	57.1 *s*	-19.4	-
$1t_2$	4.6 *p,d*	64.0 *s*	-15.9	-
$2a_1$	38.9 *s*	38.8 *p*	-9.72	E (15.08)
$2t_2$	3.8 *p*	47.5 *p*	-9.17	C (12.64) D (13.74)
$1e$	1.5 *d*	47.5 *p*	-9.15	C, D
$1t_1$	0.0	52.7 *p*	-8.17	C, D
$3t_2$	26.5 *p,d*	56.0 *p*	-5.75	B (10.35)

Figure VI-2. Valence band photoelectron spectra of $Si_2(CH_3)_6$ at photon energies, 21.2, 100, 120 and 135 eV

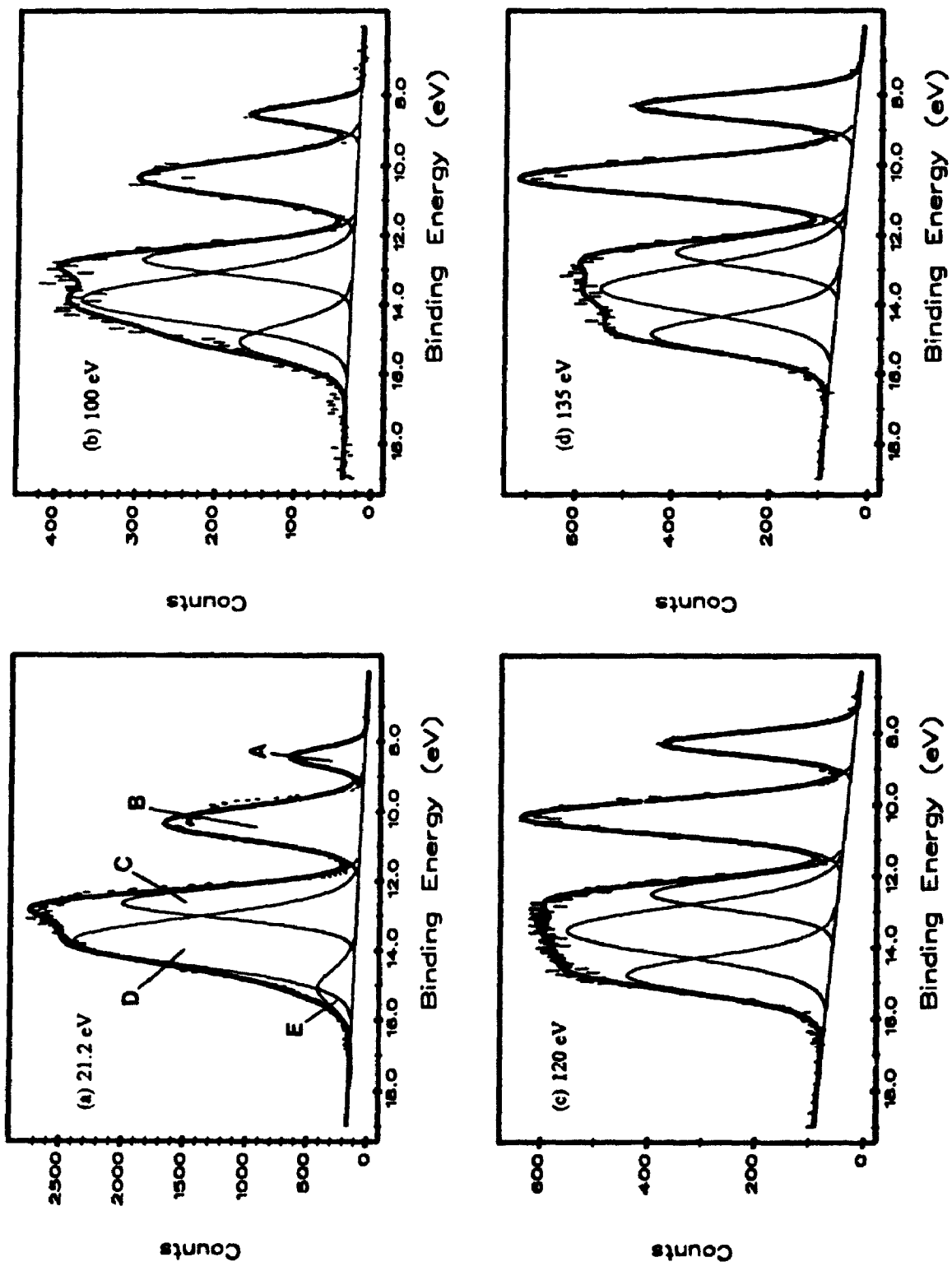
(a) 21.2 eV
A
B
C
D
E
(b) 100 eV
(c) 120 eV
(d) 135 eV
Counts
Binding Energy (eV)
18.0
16.0
14.0
12.0
10.0
8.0
0
500
1000
1500
2000
2500
100
200
300
400
600

Table VI-2. The composition and energy of calculated molecular orbitals (from reference 13) and the corresponding experimental peak and its binding energy in the photoelectron spectrum of $Si_2(CH_3)_6$ from Figure VI-2.

	Composition (%)		Calculated	Exp. Peak
Calc. MO	Si	C	Energy (eV)	& B.E (eV)
$1a_1$	15.8 *s*	50.6 *s*	-17.7	-
$2a_1$	12.4 *s*	54.0 *s*	-17.4	-
$1e$	4.6	58.6 *s*	-16.7	-
$2e$	4.2	58.8 *s*	-16.59	-
$3a_1$	46.0 *s*	24.2 *p*	-11.70	E (15.08)
$4a_1$	36.8 *s*	34.0 *p*	-10.40	E
$5a_1$	6.6 *s*	40.0 *p*	-10.20	C (12.64) D (13.74)
$3e$	2.2	42.0 *p*	-10.05	C, D
$4e$	2.8	42.6 *p*	-9.94	C, D
$5e$	1.6	43.2 *p*	-9.62	C, D
$6a_1$	7.2 *s*	42.0 *p*	-9.56	C, D
$6e$	0.8	46.3 *p*	-9.22	C, D
$1a_2$	0.0	46.4 *p*	-9.11	C, D
$2a_2$	0.0	46.8 *p*	-9.04	C, D
$7e$	28.8 *p*	46.6 *p*	-6.84	B (10.35)
$8e$	28.4 *p*	50.4 *p*	-6.54	B
$7a_1$	52.0 *p*	20.2 *p*	-5.02	A (8.45)

Figure VI-3. Valence band photoelectron spectra of $Si[Si(CH_3)_3]_4$ at photon energies, 21.2, 100, 120 and 135 eV

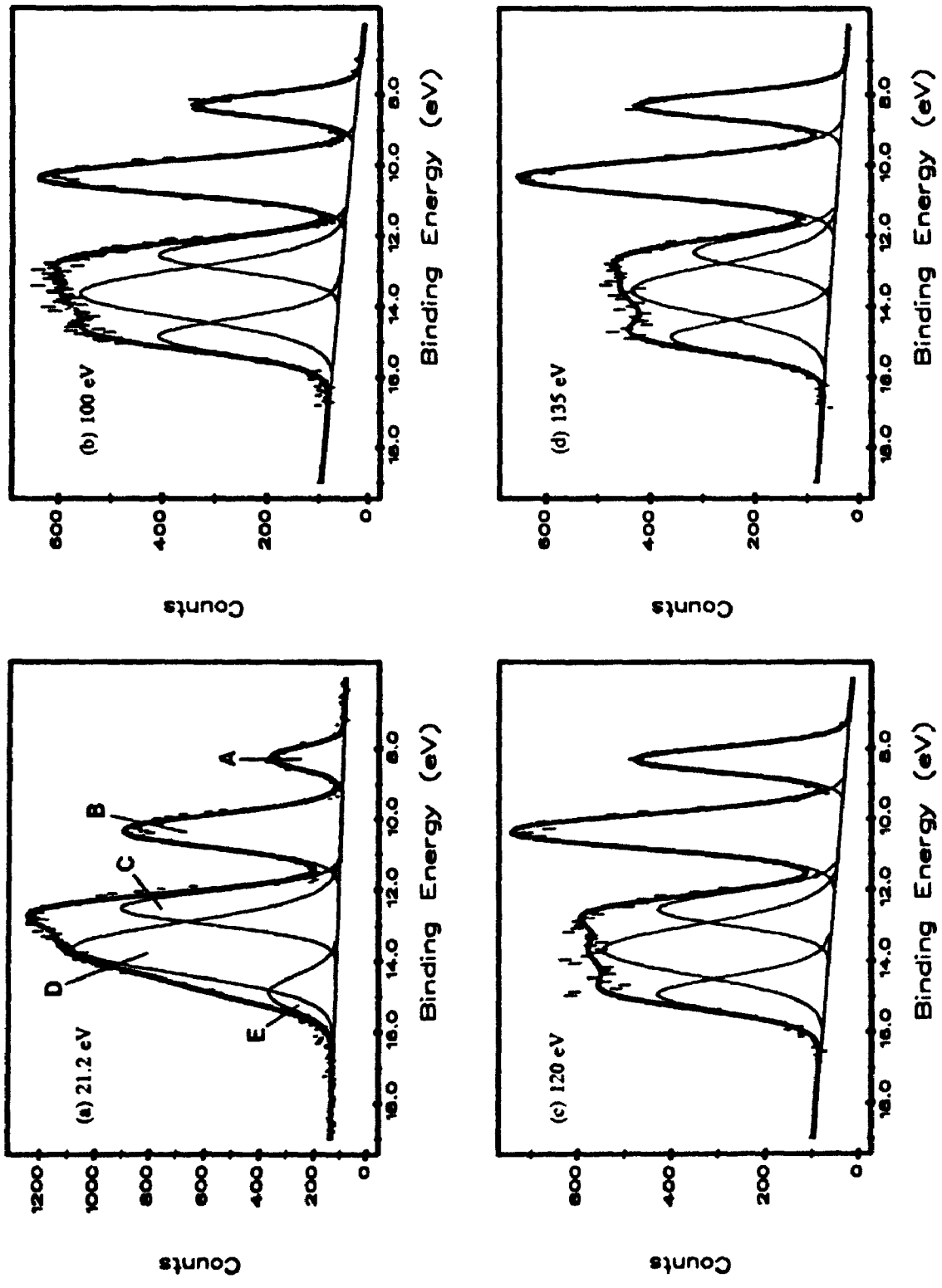
(a) 21.2 eV
(b) 100 eV
(c) 120 eV
(d) 135 eV
A
B
C
D
E
Counts
Binding Energy (eV)

Table VI-3. The composition and energy of calculated molecular orbitals (from reference 13) and the corresponding experimental peak and its binding energy in the photoelectron spectrum of $Si[Si(CH_3)_3]_4$ from Figure VI-3.

	Composition (%)			Calculated	Exp. Peak
Calc. MO	Si(Center)	Si	C	Energy (eV)	& B.E (eV)
$1a_1$	1.2	13.0 *s*	49.8 *s*	-18.47	-
$1t_2$	0.2	11.4 *s*	52.4 *s*	-18.14	-
$1e$	0.0	3.7	56.4 *s*	-17.69	-
$2t_2$	0.0	6.7 *s,p*	57.9 *s*	-17.23	-
$1t_1$	0.0	4.3	59.9 *s*	-16.81	-
$2a_1$	47.0 *s*	22.8 *s,p*	7.6 *s,p*	-14.22	E (14.88)
$3t_2$	5.9 *p*	43.1 *s*	25.0 *p*	-11.77	E
$3a_1$	2.9	16.6 *s,p*	35.5 *p*	-11.41	E
$4t_2$	0.0	2.7	38.9 *p*	-11.19	C (12.51) D (13.63)
$2t_1$	0.0	1.2	40.4 *p*	-10.86	C, D
$5t_2$	1.2	3.3	41.2 *p*	-10.71	C, D
$2e$	0.0	7.4 *d*	44.0 *p*	-10.41	C, D
$3e$	0.0	4.0	46.1 *p*	-9.89	C, D
$4a_1$	15.7 *s*	19.6 *s,p*	32.8 *p*	-9.85	C, D
$3t_1$	0.0	18.6 *p*	47.5 *p*	-9.58	C, D
$6t_2$	0.0	2.4	46.6 *p*	-9.45	C, D
$1a_2$	0.0	0.0	98.8 *p*	-9.17	C, D
$4t_2$	0.0	1.7	48.1 *p*	-9.15	C, D
$7t_2$	8.8 *p*	28.7 *p*	36.6 *p*	-7.49	B (10.34)
$4e$	0.4	28.2 *p*	46.0 *p*	-7.40	B
$5t_1$	0.0	28.4 *p*	50.0 *p*	-6.82	A (8.26)
$8t_2$	26.1 *p*	28.2 *p*	24.3 *p*	-6.54	A

Figure VI-4. Valence band photoelectron spectra of $Ge[Si(CH_3)_3]_4$ at photon energies, 21.2, 100, 120 and 135 eV.

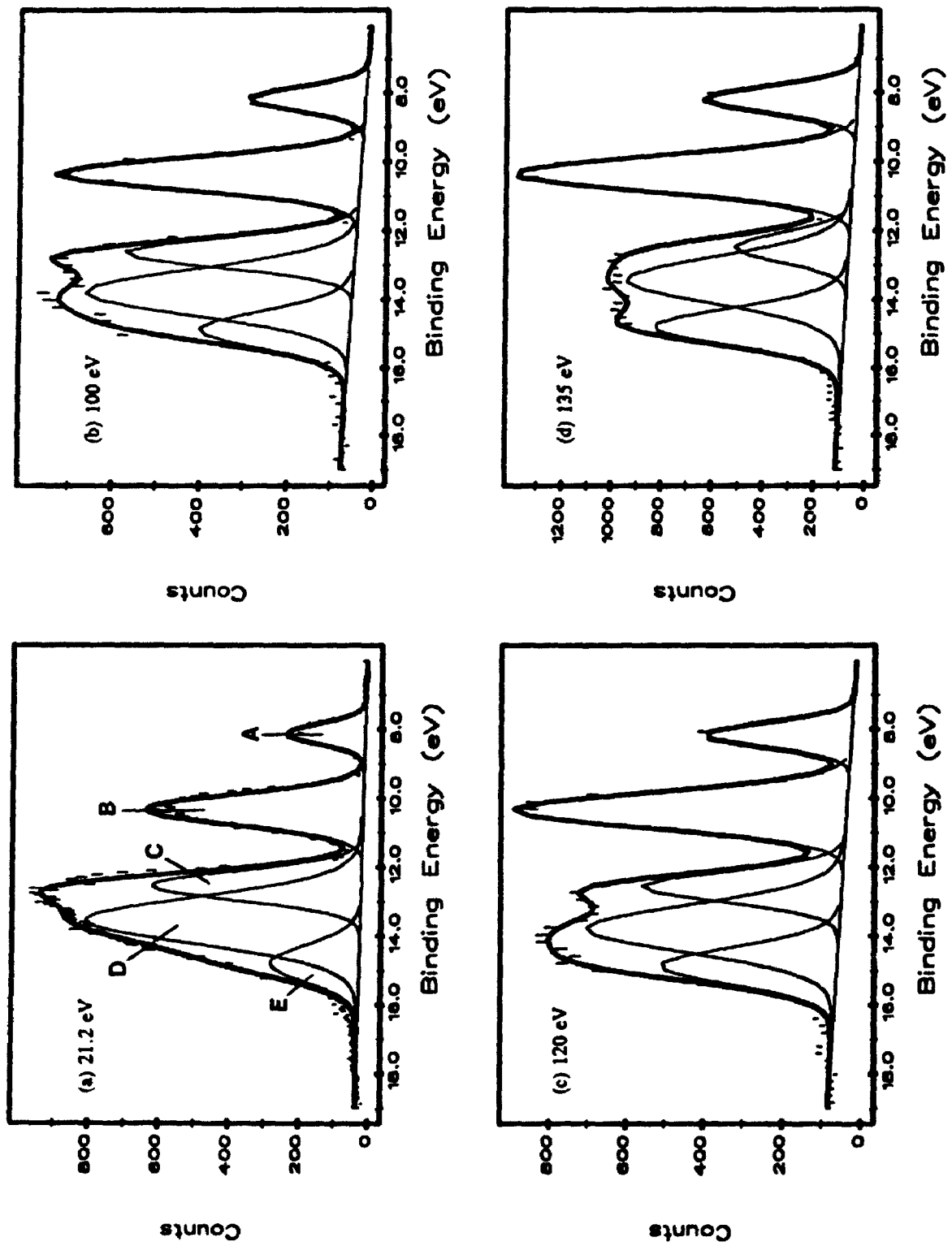
(a) 21.2 eV
(b) 100 eV
(c) 120 eV
(d) 135 eV
A
B
C
D
E
Counts
Binding Energy (eV)
0
200
400
600
800
1000
1200
18.0
16.0
14.0
12.0
10.0
8.0

Table VI-4. The composition and energy of calculated molecular orbitals (from reference 13) and the corresponding experimental peak and its binding energy in the photoelectron spectrum of $Ge[Si(CH_3)_3]_4$ from Figure VI-4.

	Composition (%)			Calculated	Exp. Peak
Calc. MO	Ge	Si	C	Energy (eV)	& B.E (eV)
$1t_2$	99.7 *d*	0.2	0.0	-30.40	-
$1e$	99.8 *d*	0.0	0.0	-30.40	-
$1a_1$	1.8	13.3 *s*	50.0 *s*	-18.50	-
$2t_2$	0.2	11.3 *s*	52.3 *s*	-18.20	-
$2e$	0.0	3.7	56.3 *s*	-17.7	-
$3t_2$	0.0	6.8 *s,p*	57.9 *s*	-17.20	-
$1t_1$	0.0	4.3	59.8 *s*	-16.81	-
$2a_1$	52.4 *s*	20.2 *s,p*	7.0 *s,p*	-14.80	E (14.80)
$4t_2$	5.9 *p*	43.0 *s*	25.0 *p*	-11.80	E
$3a_1$	2.7	18.7 *s,p*	35.1 *p*	-11.50	E
$5t_2$	0.0	2.8	38.8 *p*	-11.21	C (12.55) D (13.56)
$2t_1$	0.0	1.2	40.4 *p*	-10.90	C, D
$6t_2$	1.1	3.4	41.3 *p*	-10.70	C, D
$3e$	0.0	0.8	44.5 *p*	-10.40	C, D
$4a_1$	12.4 *s*	19.2 *s,p*	34.2 *s*	-10.00	C, D
$4e$	0.0	1.2	46.1 *p*	-9.93	C, D
$3t_1$	0.0	1.8	47.7 *p*	-9.62	C, D
$7t_2$	0.0	2.4 *p*	46.7 *p*	-9.45	C, D
$1a_2$	0.0	0.0	98.8 *p*	-9.21	C, D
$4t_1$	0.0	1.7	48.1 *p*	-9.17	C, D
$8t_2$	8.1 *p*	28.9 *p*	37.0 *p*	-7.53	B (10.34)
$5e$	0.3	28.2 *p*	46.1 *p*	-7.43	B
$5t_1$	0.0	28.4 *p*	50.0 *p*	-6.85	A (8.13)
$9t_2$	25.7 *p*	28.5 *p*	24.1 *p*	-6.53	A

Figure VI-5. Valence band photoelectron spectra of $[-Si(CH_3)_2-]_6$ at photon energies, 21.2, 100, 120 and 135 eV.

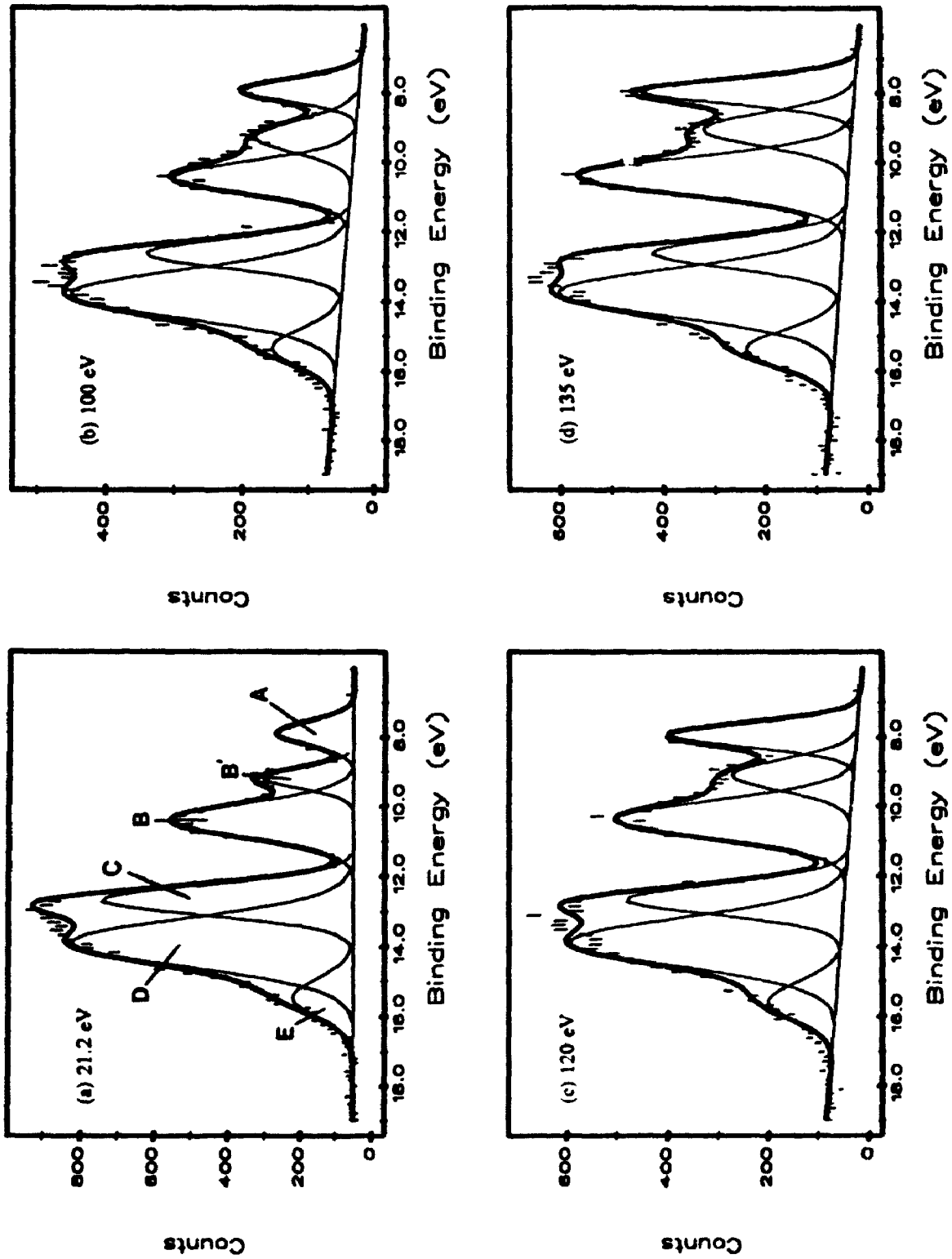
(a) 21.2 eV
(b) 100 eV
(c) 120 eV
(d) 135 eV
A
B
B'
C
D
E
I
II
III
Counts
Binding Energy (eV)
0
200
400
600
800
18.0
16.0
14.0
12.0
10.0
8.0

Table VI-5. The peaks in Figure VI-5, their binding energy and peak width for the He I spectrum of $[-Si(CH_3)_2-]_6$ (DCHS).

Peak	Binding Energy (eV)	Peak Width (eV)
A	7.89	0.796
B	9.19	0.700
B'	10.41	1.150
C	12.68	1.010
D	13.89	1.610
E	15.47	1.260

there is no precedent in the literature to support this claim, the splitting of the Si-C molecular orbitals has been assigned to the axial and equatorial arrangement of the methyl groups around the silicon ring. The steric repulsion of the axial methyl groups raises their energy (peak B) while the more isolated equatorial methyl groups (peak B') are at lower energy. To summarize the above effects, over the energy range from 21.2 to 135 eV, the C 2*p* cross section shows the greatest decrease, dropping from ~5 Mb to ~0.065 Mb.[12] Thus, orbitals that contain a large percentage of C 2*p* character will show the largest decrease in relative intensity over this energy range. The Ge 4*p* cross section exhibits the next largest decrease, ranging from ~0.7 Mb at 21.2 eV to ~0.03 Mb at 135 eV and the Si 3*p* orbitals show the smallest change in cross section, decreasing from 0.4 to 0.1 Mb

over the energy range of interest.[12] Hence, relative to the C 2*p*, orbitals composed of the Ge 4*p* electrons will show an increase in intensity over the energy range 21.2 to 135 eV, and orbitals formed from the Si 3*p* will show an even greater increase in relative intensity over the same energy range.

Table VI-6 shows the peak area as a function of photon energy for peaks A to E in Figures VI-1 to VI-5 where the area of peak B in every spectrum has been normalized to 100. The data in Table VI-6 has been used to construct Table VI-7 which compares the ratio of the area of peaks A (the metal-metal MO's) and B (the metal-carbon MO's) to that of C+D (the carbon-hydrogen MO's). This data is plotted in Figure VI-6 for the three photon energies 100, 120 and 135 eV where the solid lines represent data for the branching ratio B:(C+D) and the dashed lines are for A:(C+D)

The branching ratio B:(C+D) is quite similar for the four compounds studied with the one exception that the data for TKTG, the germanium compound, rises abruptly at 135 eV. The data for the three silicon-based molecules form three parallel lines of approximately equal slope and comparable y-intercept which is indicative of the similar composition of the molecular orbitals in these three compounds. The branching ratios for HMDS are consistently lower than those of the other three compounds. This may be due to the fact that HMDS is the only non-tetrahedral member of the group and the different composition of MO's in this molecule may result in lower branching ratios.

The branching ratio A:(C+D) is represented by the dashed lines in the lower half of Figure VI-6. The data for the two silicon-based compounds, HMDS and TKTS, are very similar with the HMDS data again exhibiting the lower branching ratio. Similar to the B:(C+D) data, the A:(C+D) branching ratio for TKTG also rises at 135 eV, but here, the overall lower value

Table VI-6. The peak areas in Figures VI-1 to VI-5 normalized so that peak B in every spectrum has an area of 100

Molecule	Peak	Photon Energy (eV) 21.2	100	120	135
$Si(CH_3)_4$	B	100	100	100	100
	C	48	36	30	27
	D	277	175	124	103
	E	17	25	27	20
$Si_2(CH_3)_6$	A	21	27	40	48
	B	100	100	100	100
	C	108	81	53	44
	D	207	166	123	101
	E	22	56	76	64
$Si[Si(CH_3)_3]_4$	A	23	38	47	46
	B	100	100	100	100
	C	97	60	50	39
	D	193	129	102	88
	E	36	63	53	48
$Ge[Si(CH_3)_3]_4$	A	25	29	31	34
	B	100	100	100	100
	C	94	71	53	28
	D	206	129	108	92
	E	54	61	58	63
$[-Si(CH_3)_2-]_6$	A	30	48	52	52
	B'	31	58	43	49
	B	100	100	100	100
	C	119	102	74	56
	D	211	220	147	131
	E	39	45	29	33

Table VI-7. The ratio of the peak areas from Table VI-6.

Molecule	Peak Area Ratio	Photon Energy (eV) 21.2	100	120	135
$Si(CH_3)_4$	B:(C+D)	0.307	0.474	0.649	0.769
$Si_2(CH_3)_6$	A:(C+D)	0.067	0.109	0.227	0.331
	B:(C+D)	0.318	0.405	0.568	0.690
$Si[Si(CH_3)_3]_4$	A:(C+D)	0.079	0.201	0.309	0.362
	B:(C+D)	0.345	0.529	0.658	0.787
$Ge[Si(CH_3)_3]_4$	A:(C+D)	0.083	0.145	0.193	0.283
	B:(C+D)	0.333	0.500	0.621	0.833

(compared to TKTS) is indicative of a substantial contribution from the Ge 4*p* atomic orbital as is expected from the metal-metal bond in this compound.

Figure VI-7 shows the cross section ratio for the Si 3*p* and Ge 4*p* compared to the C 2*p* at 100, 120 and 135 eV. The Si/C ratio forms a straight line through the three data points similar to the branching ratios in the three molecules TMS, HMDS and TKTS. The Ge/C ratio is much smaller and rises slightly at 135 eV similar to the A and B branching ratios for the germanium-containing compound TKTG.

If one assumes that peaks C and D result from MO's that are entirely C 2*p* in character then the only way that the branching ratios of TKTG can increase at 135 eV is if the corresponding orbital(s) contain considerable Ge 4*p* character. This is expected of peak A in the spectrum of TKTG because

Figure VI-6. Branching ratios for peaks A & B compared to (C+D). The ratio B:(C+D) is represented by the solid lines and A:(C+D) by the dashed lines.

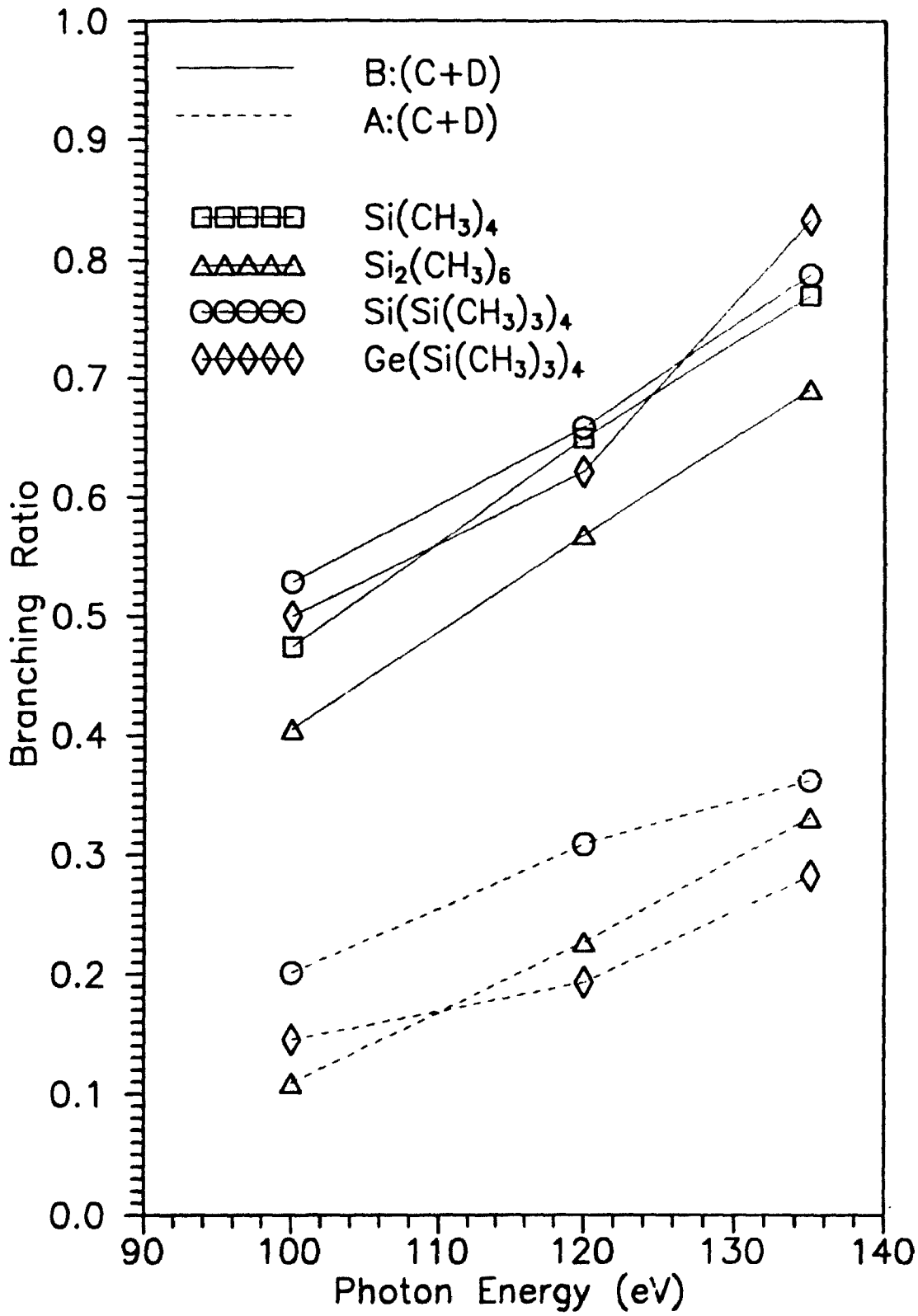
B:(C+D)
A:(C+D)
Si(CH3)4
Si2(CH3)6
Si(Si(CH3)3)4
Ge(Si(CH3)3)4
Branching Ratio
Photon Energy (eV)
1.0
0.9
0.8
0.7
0.6
0.5
0.4
0.3
0.2
0.1
0.0
90
100
110
120
130
140

Figure VI-7. The ratio of the cross sections of the Si 3*p* and the Ge 4*p* levels compared to the C 2*p*. The ratio Si/C is represented by the circles and Ge/C is represented by the diamonds.

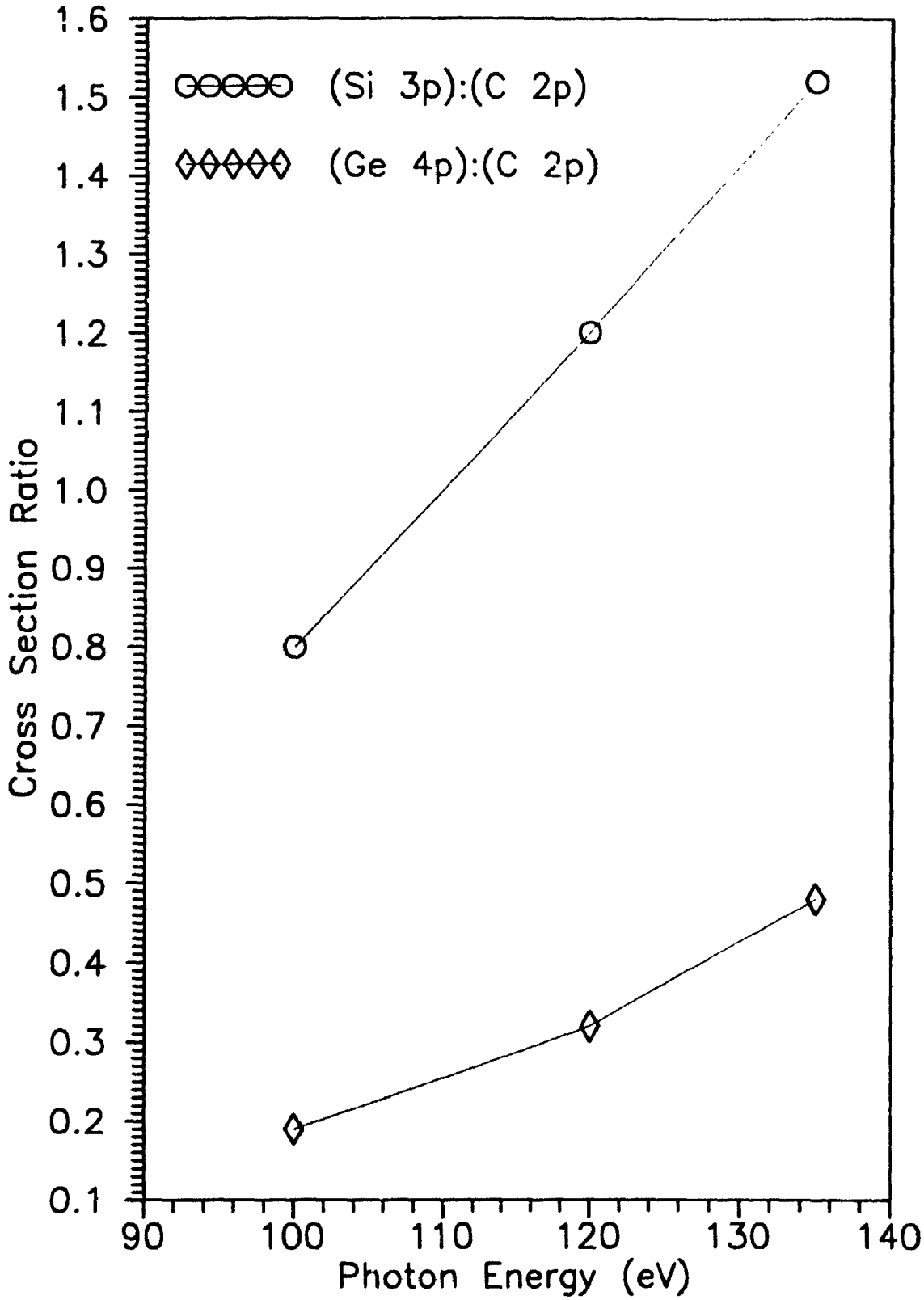
(Si 3p):(C 2p)
(Ge 4p):(C 2p)
Cross Section Ratio
1.6
1.5
1.4
1.3
1.2
1.1
1.0
0.9
0.8
0.7
0.6
0.5
0.4
0.3
0.2
0.1
90
100
110
120
130
140
Photon Energy (eV)

it results from the metal-metal bond and this feature is predicted by the Xα calculations. However, this also implies that peak B must correspond to at least one MO that has significant Ge 4*p* character; a fact that is not supported by the calculations (see Table VI-4).

Section VI-4; Conclusions.

The valence band photoelectron spectra of organo-silicon clusters consists of three main peaks with binding energies ranging from approximately 8 to 18 eV. The peak with the lowest binding energy (~8 eV) results from the metal-metal bonding molecular orbital which is primarily of Si 3*p* (or Ge 4*p*) character. The next highest peak (~10 eV) results from orbitals associated primarily with the metal-carbon bonds and are mostly C 2*p* and Si 3*p* in character. There is, however, some evidence that, in the Ge compound, this peak may also result from MO's associated with the metal-metal bond. The third and broadest peak has been divided into three unresolved transitions: the first two (at ~12.5 and 14.2 eV) are associated almost entirely with the C-H bonding orbitals and are composed mostly of C 2*p* electrons. The third transition in the third peak (~15.2 eV) is assigned metal-metal character because of its large increase in relative intensity as a function of photon energy. The two exceptions to the above description are in the case of TMS [$Si(CH_3)_4$] which has no metal-metal bond and in the case of DCHS [$-Si(CH_3)_2-]_6$ in which the metal-carbon peak is split into two separate peaks. Although there are no calculations to support this data, the splitting of the Si-C bonding MO's in the second peak may be due to the axial and equatorial positions of the methyl groups around the Si ring.

Section VI-5; References.

1) J.J. Toman, A.A. Frost and S. Topiol; Theoret. Chim. Acta, 58, 285, (1981).

2) J.E. Bice, K.H. Tan, G.M. Bancroft and J.S. Tse; Inorg. Chem., 26, 4106, (1987).

3) Z. Berkovitch-Yellin, D.E. Ellis and M.A. Ratner; Chem. Phys., 62, 21, (1981)

4) A.E. Jonas, G.K. Schweitzer and F.A. Grimm; J. Elec. Spec. and Rel. Phen., 1, 29, (1973).

5) W.B. Perry and W.L. Jolly; J. Elec. Spec. and Rel. Phen., 4, 219, (1974)

6) D.G.J. Sutherland, G.M. Bancroft and K.H. Tan; J. Chem. Phys., In Press

7) A.G. Brook, F. Abdesaken and H. Söllradl; J. Organomet. Chem., 299, 9, (1986).

8) R. West, L.F. Brough and W. Wojnowski; Inorg. Synth., 19, 265, (1979).

9) J.D. Bozek, J.N. Cutler, G.M. Bancroft, L.L. Coatsworth, K.H. Tan, D.S. Yang and R.G. Cavell, Chem. Phys. Lett., 165, 1, (1990).

10) G.M. Bancroft, I. Adams, D.K. Creber, D.E. Eastman and W. Gudat; Chem. Phys. Lett., 38, 83, (1976).

11) R. Bertoncello, J.P. Daudey, G. Granozzi and U. Russo; Organometalics, 5, 1866, (1986).

12) J.J. Yeh and I. Lindau; Atomic Data and Nuclear Data Tables, 32, 1, (1985).

13) J. Xiong, D.G.J. Sutherland, T.K. Sham, G.M. Bancroft and K.H. Tan; to be published.